

Title: Microfluidic Human Physiomimetic Liver Model as a Screening Platform Recapitulates Intrinsic and Idiosyncratic Drug Toxicity

Souradeep Dey¹, Amritha Bhat², Janani G², Vartik Shandilya³, Raghvendra Gupta^{1,3,4}, Biman B. Mandal^{1,2,4}*

¹Centre for Nanotechnology, Indian Institute of Technology Guwahati, Guwahati-781039, Assam, India.

²Biomaterials and Tissue Engineering Laboratory, Department of Biosciences and Bioengineering, Indian Institute of Technology Guwahati, Guwahati-781039, Assam, India.

³Department of Chemical Engineering, Indian Institute of Technology Guwahati, Guwahati-781039, Assam, India.

⁴Jyoti and Bhupat Mehta School of Health Sciences and Technology, Indian Institute of Technology Guwahati, Guwahati-781039, Assam, India.

***Corresponding author:**

Prof. Biman B. Mandal

Professor and SwarnaJayanti Fellow

Department of Biosciences and Bioengineering

Centre for Nanotechnology

Jyoti and Bhupat Mehta School of Health Sciences and Technology

Indian Institute of Technology Guwahati, Assam, India

Phone: +91-361-258 2225 (O)

Fax: +91 361 258 2249 (O)

E-mail: biman.mandal@iitg.ac.in, mandal.biman@gmail.com

1. Introduction

DILI is a patient specific, temporal, multifaceted pathophysiological process in response to drugs or other xenobiotics that arises either as a predictable event or as an unpredictable event leading to loss of both parenchymal and non-parenchymal cells. [1] Typically, DILI is classified into intrinsic and idiosyncratic hepatotoxicity based on the mechanism of action of the chemical compound. The intrinsic type is direct, dose related, predictable and occurs at a short duration in individuals exposed to certain threshold level of drugs. In contrast, idiosyncratic type is drug dose independent, has a longer latency period, is triggered by the interaction of drug with the host and environmental factors and occurs mainly after re-exposure. Even though idiosyncratic DILI is a rare event, but it remains a leading cause for new chemical entity failure in phase II drug development, post-market withdrawals and restriction uses. [2, 3]

The U.S. Food and Drug Administration (FDA) and European Medicines Agency (EMA) requires the evaluation of new drug candidates in animal models, before initiating human clinical trials of a new chemical entity. [3-5] However, an analysis of 150 drugs in animals that caused adverse reactions in humans, reported the concordance of hepatotoxicity finding between animals studies and observed human toxicities to be only 55%. [6] The major reason for this low concordance is hypothesized to be the genetic variations, mechanism of toxicity and drug metabolizing pathways that involves the differences in drug metabolizing enzyme and transporter expressions. [1, 7] Furthermore, DILI in humans is typically not identified until clinical trials or post-marketing, leading to an increased risk of hepatotoxicity in clinical trial participants as well as a financial burden in the drug development pipeline. Thus, a paradigm shift in reduction, replacement and refinement (3‘Rs’ principle) of animal models is desired from the pharmaceutical and biotechnology industries which serves the critical need for the development of more predictive and human-relevant in vitro models for improved hepatotoxicity testing.

Moreover, the FDA centre for drug evaluation and research, EMA and the Government of India’s “New Drugs and Clinical Trials (Amendment) Rules, 2023” also encourages the adoption of in silico and in vitro models to improve the regulatory efficiency and expedite drug development. [8-10] In order to drive a paradigm shift in the use of non-animal methods for drug discovery and development pipelines, conventional 2D coculture, 3D spheroid and 3D dense constructs based in vitro models are currently being employed for hepatotoxicity prediction. Even though these models are robust and affordable, but their applications are

limited due to their inability to mimic the complex in vivo microarchitecture and the physiologically relevant fluid flow condition in the liver, maintain the viability and functionality of the cells for prolonged periods as well as limited oxygen and nutrient supply to the cells in the core of dense constructs. [11] Therefore, one of the promising solutions has been the development of complex human physiomimetic models to recapitulate the liver acinus or sinusoid structure and function to improve their application for drug screening or drug toxicity evaluation [10]. Recently, reported dynamic in vitro liver models demonstrated enhanced secretome release and functionality under dynamic fluid flow condition, but it was limited to a short period of time. Further, in few studies drug induced hepatotoxicity was evaluated following 24 hours of drug exposure, which limits the applications of the models for evaluation of chronic hepatotoxicity and/ idiosyncratic DILI. [12-15] Moreover till date, only few 3D liver in vitro models have emulated the microarchitecture of the liver acinus along with dynamic fluid flow condition to predict DILI. [10]

Therefore, in line with the evolution of the human liver in vitro models, we developed a human physiomimetic 3D printed in vitro liver acinus model for detailed mechanistic studies using transdisciplinary technologies (**Figure 1**). With the concept to mimic the microniche of the liver acinus and the native hierarchical arrangement of the cords of hepatocytes separated by functional sinusoidal microvasculature networks, we 3D printed a biomimetic hepatic acinus construct using a cell instructive liver mimetic biomaterial ink composed of regenerated *B. mori* silk fibroin (SF), liver decellularized extracellular matrix (dECM) and a bulking agent gelatin (**Figure 1A-C**). Simultaneously, a micro-physiomimetic liver acinus bioreactor platform was also developed to recapitulate the physiological microcirculation and shear stress effects on the hepatocytes in the human liver sinusoid to promote hepatocyte physiology, cell-cell interaction, cell-matrix interaction and inform drug induced liver toxicities of human relevance (**Figure 1D**).

Further, to closely recreate the liver acinus cellular microniche and add a higher order of biological complexity to the model necessary to study diverse phenotypes of liver toxicity, we incorporated the 3D printed liver acinus model with matured human adipose mesenchymal stem cell-derived hepatocyte-like cells (HLCs), human umbilical vein endothelial cells (HUVECs) and human hepatic stellate cells (HHSCs) to emulate the physiologically relevant cellular combination and improve the long-term physiological functionality. The tricultured scaffolds were matured in either static or dynamic condition in the developed 3D printed physiomimetic microfluidic bioreactor connected to a recirculating peristaltic pump till 15 days to emulate the spatial and temporal microenvironment of the liver acinus. Following 15 days

of maturation, our developed tricultured HPLAM platform in the perfusion condition was able to demonstrate and maintain physiologically relevant levels of albumin and urea synthesis, CYP activity and LDH activity (**Figure 1E and F**). In line with the changes in the secretome levels observed, the gene expression studies and immunofluorescence staining also confirmed the enhanced expression of the HLC, HUVEC and HHSC specific genes and markers in the perfused tricultured liver acinus model in comparison to the static model. Thus, the perfused tricultured liver acinus model acted as an optimal analog of the vascularized liver acinus suitable for evaluating diverse phenotypes of drug toxicity. Furthermore, to determine the sensitivity and specificity of the physiomimetic liver acinus model as potential platform to evaluate diverse phenotype of DILI of human relevance, we used drugs (severity class 0 – 8) across the different classifications observed in DILIRank, i.e. “No-DILI concern”, “Less-DILI concern” and “Most-DILI concern”. [16]

Interestingly, our model predicted a diverse phenotype of hepatotoxicity with more human specific sensitivity in comparison to the previously reported 3D in vitro liver models [17-21]. Overall, in this study we validate the potential of the 3D printed HPLAM cultured under physiologically relevant microenvironment, to act as metabolic biofactories with enhanced hepatic functionality and biomarker expression profiles for prolonged durations as well as demonstrate dose- and time-dependent hepatotoxic response of human relevance compared to static culture. Thus, the developed HPLAM emulated *in vivo* like functions and confirmed the potential utility of this platform for DILI risk assessment.

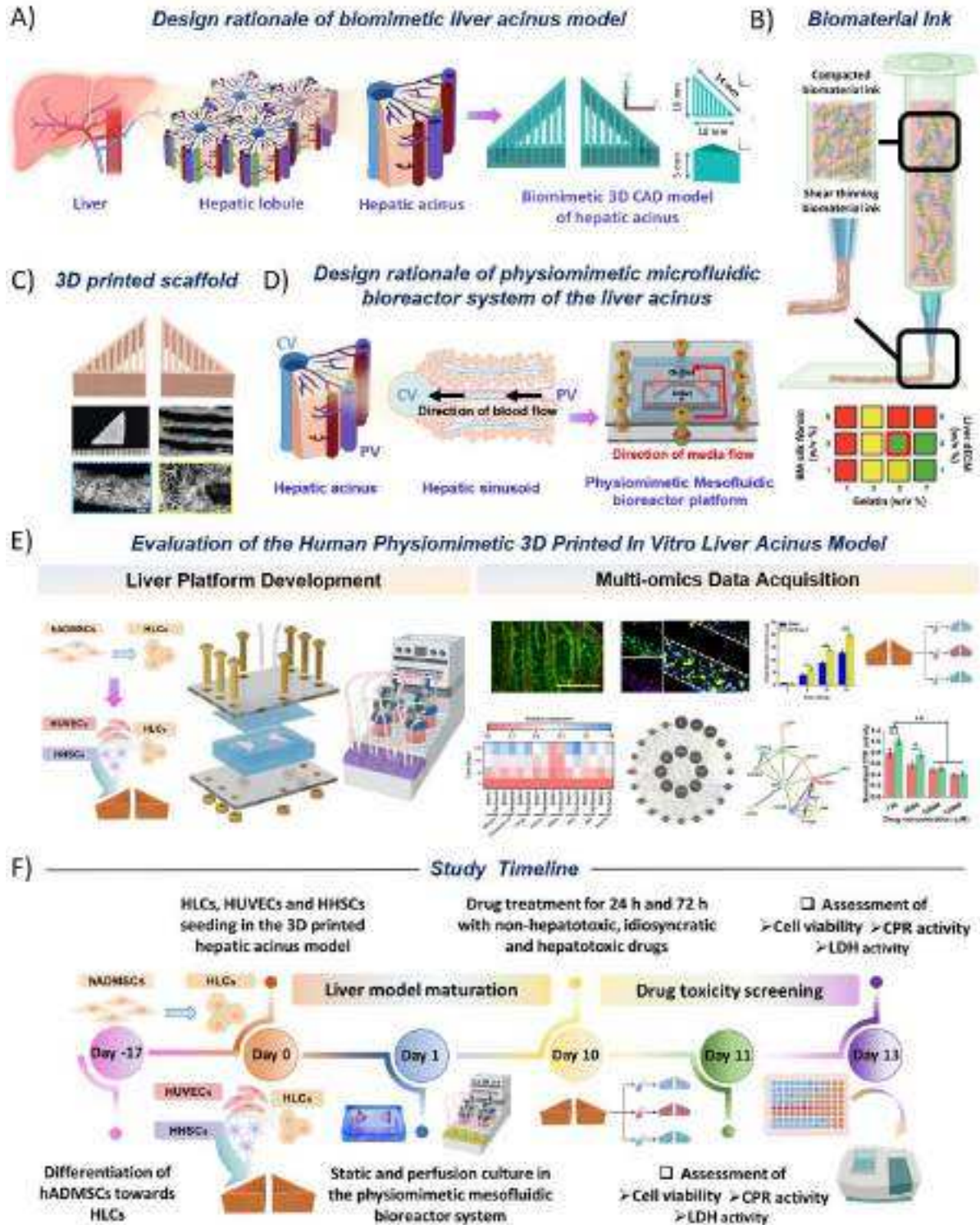


Figure 1: Schematic representation of the rationale and timeline of the study; A) Illustration of the native hepatic acinus inspired development of the biomimetic CAD model of the 3D scaffold; B) Schematic representation of the biomaterial ink formulation and its characterization; C) Illustration of the 3D printed biomimetic liver acinus scaffold and its characterization; D) Scheme representing the native human liver acinus microphysiological environment inspired conceptualization of human physiometric liver microfluidic bioreactor platform E) Illustration of the overall development and functional evaluation of the human

physiomorphic in vitro liver acinus model F) The timeline of the vital experimental steps followed in the study. Created with BioRender.com

2. Objectives

2.1 Develop a decellularized liver extracellular matrix mimetic biomaterial ink that exhibits shear thinning behaviour with thixotropic recovery and high print fidelity for 3D printing.

2.2 Fabricate a 3D printed biomimetic liver acinus construct using the developed liver extracellular matrix mimetic biomaterial ink to confer in vivo like physiological relevance

2.3 Fabricate a human physiomorphic liver acinus microfluidic platform to recapitulate the key biological phenomena of native liver acinus

2.4 Perform in vitro functional validation of the human physiomorphic liver acinus model to assess the cellular alignment, cell proliferation, maturation, albumin and urea secretion and cytochrome P450 and LDH activity.

2.5 Validate the maturation of the tricultured physiomorphic liver acinus model by assessing the liver-specific physiological genes and biomarkers expression.

2.6 Assess the sensitivity of the human physiomorphic liver acinus platform for detection of diverse phenotypes of hepatotoxicity.

3. Material and Methods

3.1 Materials

All the preparatory chemicals and few assay kits were procured from Sigma, USA. The cell culture grade chemicals, assay kits and molecular biology reagents were procured from Invitrogen, USA. The cell culture grade plasticwares and consumables were sourced from Thermo Fisher Scientific, USA.

3.2 Development of silk fibroin based liver mimetic biomaterial ink and its characterization

3.2.1. Regeneration of silk fibroin

For the isolation of *B. mori* silk fibroin (SF), *B. mori* cocoons were sourced from the local silk farms in Guwahati, Assam, India and the regenerated aqueous solution of SF was acquired according to the previously published protocols [22, 23]. Briefly, cocoons were finely chopped and degummed in 0.02 M sodium carbonate (Na_2CO_3 , Sigma-Aldrich, USA) to remove the sericin. Post-degumming the fibers were thoroughly rinsed in deionized water and dried at room temperature (25 °C). Further the fibers were dissolved in 9.3 M lithium bromide (LiBr,

Sigma-Aldrich, USA) at 60 °C for 4 h. The obtained solution was then dialyzed against deionized water for 2 days in a 12 kDa dialysis membrane, with frequent water changes to remove the residual LiBr. After dialysis, the protein concentration was estimated using gravimetric method and the regenerated SF solution was utilized for the preparation of biomaterial ink.

3.2.2. Preparation and characterization of decellularized liver ECM

For the preparation of liver ECM, porcine liver tissue (purchased from a local market, Assam, India) was decellularized according to the previously published chemical decellularization technique followed by enzymatic solubilization [7, 24]. Briefly, the porcine liver tissue was cut into thin slices, subjected to freeze-thaw cycle and agitated alternately in 0.1 M phosphate-buffered saline (PBS) and deionized water to initiate cell lysis. Further, for proper decellularization the liver slices were agitated in Triton X-100 (1% v/v) and ammonium hydroxide solution (0.1% v/v) for 4 days. Further the decellularized liver extracellular matrix was lyophilized and digested in a pepsin buffered solution (1% w/v in 0.01 N HCl) to obtain a 10 mg/mL solution of liver ECM. Finally, the liver ECM solution was brought to pH 7.4 and strained through a 70 µm cell strainer to acquire liver ECM-derived microparticles. These liver ECM-derived microparticles (dECM) were freeze-dried and stored at 4° C for biomaterial ink preparation.

The decellularization of the liver was validated through histological evaluation and by quantifying the DNA, glycosaminoglycan (GAG), collagen and protein content. For histological evaluation, 15 µm cryosections of both native and decellularized liver samples were obtained and subsequently stained with Alcian blue and picosirius red stain to assess the GAG and collagen preservation, respectively, following manufacturer's protocols. The images were captured via bright-field microscopy using Nikon Eclipse Ti2 (Nikon, Japan). Quantification of the DNA, glycosaminoglycan (GAG), collagen and protein content in the native and decellularized liver samples were done using Quant-iT PicoGreen dsDNA assay, dimethylmethylene blue assay, Sirius Red Dye method and Bradford assay, respectively, as previously described [25, 26].

3.2.3. Formulation, optimization and printability of liver specific biomaterial ink

In this study, we developed a liver ECM mimetic biomaterial ink using regenerated SF, dECM and a bulking agent gelatin (Sigma-Aldrich, USA). Gelatin was used as bulking agent to enhance the printability of the silk-liver ECM based biomaterial ink. Moreover, the printability

of the biomaterial ink was optimized by blending different concentration of regenerated SF solution (1-5%, w/v), dECM (1-5%, w/v) and gelatin (1-7%, w/v). The blended ink solution was loaded into 4 mL cartridges (Cellink, Sweden) with 27G blunt needles and incubated at 20 °C for 15 min to ensure complete gelation. Further, the printability of the biomaterial ink was evaluated based on the gelation, shear-thinning, stability and self-standing nature by extruding it using BIO X 3D bioprinter (Cellink, Sweden).

3.2.4. Physico-chemical characterization of developed liver ECM mimetic biomaterial ink

3.2.4.1. Fourier transform infrared (FTIR) spectroscopy

The structural analysis of the biomaterial ink was evaluated using attenuated total reflectance fourier transform spectrometer (PerkinElmer FTIR Spectrum Two, USA). The samples of individual components and blend biomaterial ink were prepared by freeze drying. The infrared spectra were recorded from 1000 – 1800 cm^{-1} culminating from 32 scans averaged to a single spectrum with a resolution of 4 cm^{-1} .

3.2.4.2. Rheological characterization

Rheological characterizations of the biomaterial ink were performed using a rheometer (MCR 302, Anton Paar, Austria) with a standard steel parallel plate of diameter 25 mm. Prior to the tests the sample holder of the rheometer was maintained at 20 °C, unless specified. For the rheological analysis, the biomaterial ink solution was placed in between the two parallel plates maintained at a distance of 0.5 mm and 0.1N (Newton) force was applied for all tests. The rheological test methods performed were temperature sweep for assessment of temperature-based viscosity and modulus changes, oscillatory strain sweep (amplitude sweep test) to determine the linear visco-elastic region (LVER) of biomaterial ink, frequency sweep to understand the frequency dependent changes in visco-elastic behaviour and thixotropic analysis to comprehend the deformation and regeneration capability of the biomaterial ink. The temperature sweep analysis was performed at a varying temperature range of 4 – 60 °C while maintaining the shear strain ($\gamma = 1\%$) and angular frequency ($\omega = 10 \text{ rad.s}^{-1}$) constant. The amplitude sweep was performed in the range of 0.1% to 1000% shear strain (γ) at a constant temperature (20 °C) and angular frequency ($\omega = 10 \text{ rad.s}^{-1}$) to determine the yielding point and the linear viscoelastic range of the biomaterial ink. Further, the change in the complex viscosity (η^*) against shear strain (γ) was also determined. The biomaterial ink was further evaluated for frequency sweep within the LVER region obtained from the amplitude sweep by varying the

angular frequency (ω) from 0.1 to 100 rad/s at a constant shear strain ($\gamma = 1\%$) and temperature (25 °C). For the three-interval thixotropy test (3ITT), the biomaterial ink was exposed to alternating cycles of low shear strain ($\gamma = 1\%$), low angular frequency ($\omega = 10 \text{ rad.s}^{-1}$) and high shear strain ($\gamma = 100\%$), high angular frequency ($\omega = 100 \text{ rad.s}^{-1}$).

3.3. Native human liver acinus inspired conceptualization of the biomimetic liver acinus CAD design, 3D printing and its characterization

3.3.1. CAD designing and 3D printing of biomimetic liver acinus model

The liver acinus is the smallest and basic structural and functional unit of the liver. It comprises of one-sixth of the hepatic lobule and is composed of the hepatocytes arranged in the form of liver cords within a sinusoid network, a central vein and the portal vein. With the concept to mimic the complex microarchitecture of the liver acinus, a 3D biomimetic CAD model of the liver acinus was developed using AutoCAD software (Autodesk, USA). The native liver acinus inspired CAD model closely recapitulated the hepatic cord in the form of filaments along with the hepatic sinusoidal networks in the form of spaces in between the adjacent filaments. The distance between the adjacent filaments were modelled at 200 μm to facilitate the paracrine signalling among the parenchymal and the non-parenchymal cells. Further the CAD model was processed using the Slic3r (1.3.0, Alessandro Ranellucci) to obtain the G-code file, which was imported to the Bio X 3D microextrusion bioprinter (Cellink, Sweden) for printing. The parameters for slicing and 3D printing have been listed in **Table 1**.

3D printing of the acellular biomimetic hepatic acinus construct was done using the silk-liver dECM based biomaterial ink. The biomaterial ink was loaded into 4 mL cartridges (Cellink, Sweden) with 27G blunt needles and incubated at 20 °C for 15 min to ensure complete gelation, followed by extrusion printing at 20-22 °C. For optimal printing condition, the print-bed temperature was kept at a range of 15-16 °C and the print speed and extrusion pressure were maintained at 5 mm.s^{-1} and 50-60 kPa. Post printing, the 3D printed constructs were freeze-dried and crosslinked using 1-ethyl-3-(3-dimethylaminopropyl) carbodiimide hydrochloride (EDC) and N-hydroxysuccinimide (NHS) chemistry for 12 h to induce β -sheets [24]. Further the scaffolds were washed with de-ionized water repeatedly to ensure the complete removal of residual crosslinking solution and by-products. The crosslinked scaffolds were used for further biological experiments.

Table 1: *Dimensions of the 3D biomimetic liver acinus CAD model*

Parameters	Measurements
Dimensions of the hepatic acinus like construct (base, perpendicular, hypotenuse and height) (mm)	10, 10, 14, 5
Total no. of layers	20
Inter layer increment (μm)	250
Inter filament distance (μm)	200
Nozzle diameter (μm)	250
Extruder temperature (°C)	20 – 22
Print bed temperature (°C)	15 - 16
Extrusion pressure (kPa)	50 - 60
Printing speed (mm.s ⁻¹)	5

3.3.2. Physicochemical characterization of the 3D printed liver acinus model

3.3.2.1. Field emission scanning electron microscopy (FESEM)

The morphology of the acellular 3D printed constructs, its pore size, and filament dimensions were determined using field emission scanning electron microscopy (Zeiss, Germany) at an operating voltage of 2-3kV. The 3D printed constructs were lyophilized, and sputter coated with gold before analysis. The micrographs obtained were analysed with ImageJ (NIH, USA) software to determine the pore size and the printed filament diameter from 10 random pores and filaments.

3.3.2.2. Swelling study

The swelling ratio of the 3D printed constructs was determined using the conventional gravimetric method reported earlier [27]. Briefly, the dry weight of the freeze-dried 3D printed scaffolds was weighed and immersed in phosphate buffered saline (PBS; pH 7.4) at 37 °C for 30 h. The weight of the swollen constructs was recorder at definite time intervals, after removing the excess PBS on surface of the scaffold using filter paper.

The swelling ratio was calculated using the following equation:

$$\text{Swelling ratio} = \left(\frac{W_s - W_d}{W_d} \right) \quad (1)$$

Where, W_s and W_d represents the swelled weight and initial dry weight of the constructs, respectively.

3.3.2.3. *In vitro degradation assessment*

The *in vitro* degradation of the 3D printed constructs was assessed by analysing the weight loss post 28 days of incubation of the constructs (n=3) in 0.1 M PBS (pH 7.4) solution at 37 °C. 0.05% (w/v) sodium azide was added in the PBS solution to prevent any microbial growth. At pre-determined time points the incubated constructs were taken out, washed with milli-Q water, freeze dried and the dry weight was recorded. The mass remaining (%) of the printed constructs were calculated using the following formula:

$$\text{Mass degraded (\%)} = \left(\frac{W_i - W_f}{W_f} \right) \times 100 \quad (2)$$

$$\text{Mass remaining (\%)} = 100 - \text{mass degraded (\%)}$$

Where, W_i and W_f represents the initial dry weight and final dry weight of the constructs, respectively.

3.3.2.4. *In vitro stability assessment*

The stability of the cross-linked constructs was evaluated by Bradford method as per our previous reports [28]. The initial weight of the constructs (W_1) post crosslinking was noted and subsequently incubated in 0.1 M PBS (pH 7.4) solution with 0.02% (w/v) sodium azide at 37 °C. At specific time points 20 µL of PBS consisting of the releasate was collected and incubated with 200 µL of Bradford reagent for 20 min. Following incubation, the absorbance was measured at 525 nm and the unknown concentration of the protein leached out from the crosslinked scaffolds (W_2) was determined from the standard curve. The amount of protein released was represented in terms of percentage as per the following formula:

$$\text{Protein release (\%)} = \left(\frac{W_2}{W_1} \right) \times 100 \quad (3)$$

3.3.2.5. *Porosity assessment*

The porosity of the 3D printed cross-linked constructs was determined following the hexane displacement method, as previously reported [24]. The 3D printed constructs were submerged

in a known volume of hexane (V_1) in a graduating measuring cylinder. The hexane volume after the immersion of the construct (V_2) and the final hexane volume after the removal of the construct (V_3) was recorded. Thereafter, the porosity was estimated by using the following formula:

$$\text{Porosity (\%)} = \left(\frac{V_1 - V_3}{V_2 - V_3} \right) \times 100 \quad (4)$$

3.3.2.6. Mechanical characterization

Evaluation of mechanical properties is one of the most essential aspects of any fabricated organ model. The mechanical properties were assessed using Instron 5944 (Norwood, MA, USA) having a 100 N load cell. For analysis, two different sets of acellular biomimetic liver acinus constructs were 3D printed, where set I consisted of constructs with the 3D printed filaments aligned in vertical direction while set II consisted of constructs with 3D printed filaments aligned in horizontal direction. Cuboid constructs of dimension 10 mm (length) \times 10 mm (width) \times 10 mm (height) with horizontally or vertically aligned filaments were 3D printed for determining both the compressive modulus and the compressive stress and strain. For unconfined compression test, the constructs were loaded in between the compression plates and studied in the displacement control mode at a crosshead speed of 5 mm.min⁻¹ at RT (25 °C). Similarly, for tensile test, dumbbell shaped constructs of dimension 50 mm (length) \times 10 mm (width) \times 3 mm (height) with horizontally or vertically aligned filaments were 3D printed to determining both the tensile modulus and the tensile stress and strain. For tensile test, the constructs were placed within the tension grips and extended at 2 mm.min⁻¹ until failure. Analysis of all the samples were done in a PBS bath maintained at 25 °C. The stress-strain curves were plotted, and the compressive and tensile moduli were calculated from the first 10% strain of the stress-strain curves.

3.4 Native human liver acinus microphysiological environment inspired conceptualization of human physiometric liver microfluidic bioreactor design, 3D printing and its characterization

3.4.1 CAD designing, 3D printing and assembly of human physiometric liver microfluidic bioreactor

Based on the concept of the study, a human physiometric microfluidic bioreactor platform was developed to recapitulate the liver acinus physical and biochemical microenvironmental

cues that complement *in vivo* models as part of a new paradigm for understanding drug induced hepatotoxicity of human relevance. The physiomimetic microfluidic bioreactor was designed in two parts, the bottom and the top layer, using AutoCAD software (Autodesk, USA). The bottom layer was designed to accommodate the scaffold compartments and the perfusion channels while the top layer was designed to act as a negative mold for the development of a complementary layer to the bottom part. Both the layers were 3D printed using a Form 3B+ SLA 3D printer (FormLabs, USA) using a BioMed Clear V1 biocompatible resin (FormLabs, USA) with USP Class VI biocompatibility rating. After printing, all the models were rinsed in $\geq 99\%$ isopropyl alcohol and post-cured with additional UV dosage using FormWash (FormLabs, USA) and FormCure (FormLabs, USA) respectively as per manufacturer's suggestions. Post curing, a thin polydimethylsiloxane (PDMS; Sylgard 184; Dow Corning, USA) layer was developed using the 3D printed top layer as a negative mold, to act as a complementary gasket to the 3D printed bottom layer for proper sealing of the microfluidic channels. Further, two holes of 3 mm diameter were punched in the PDMS layer to form the inlet and outlet port of the device through which a perfusion microfluidic circuit for liver acinus model culture was established. Finally, the complete microfluidic bioreactor was assembled by stacking the 3D printed bottom layer and the complementary PDMS top layer in between two 2 mm poly (methyl methacrylate) (PMMA) sheets and compressed tightly using eight screws to prevent potential media leakage. The overall dimensions of the microfluidic device are enlisted in supplementary information (**Figure S3**). Unlike the conventional plasma bonded PDMS-based devices, this bioreactor platform could be disassembled to allow access to the hepatic constructs and could be resealed multiple times. Before cell culture applications, both the layers of the device were sterilized by wet autoclaving and ultraviolet light treatment before assembly.

The total cellular media volume of the system was estimated to be approximately 2 mL. Flow of media in the channels and the scaffold compartments in the microfluidic platform was achieved through a recirculating peristaltic pump (3D Biotek, USA) to ensure the accumulation of secretome and signalling molecules. The connection of the microfluidic device with the peristaltic pump was established through thin tubing (Cole-Palmer, USA) with valved breakaway couplings for easy removal of device or media changes. Flow rate of the media was adjusted through the peristaltic pump and the regulation of the air, CO₂ level and temperature were maintained by placing the whole perfusion setup inside a cell culture CO₂ incubator (Eppendorf, Germany).

3.4.2 Computational fluid dynamic analysis

3.4.2.1 Calculation of flow rate of cell culture media to recapitulate the *in vivo* hepatic sinusoidal flow condition and its physiological effects

To optimize the hepatocytes physiology, it is essential to determine the flow rate that mimics the sinusoidal microenvironmental flow conditions and the physiological shear stress on the hepatocytes. The dimensions of the perfusion device and the liver sinusoids are different. In order to emulate the physiological flow conditions inside the liver sinusoids in the *in vitro* physiomimetic liver acinus model, it had to be ensured that both the systems are dynamically similar. This was achieved by ensuring the same Reynolds number (see **Table 2**) in the two systems. The velocity, and thus the flow rate of the cell culture media, was calculated from Reynolds number assuming that it has the same properties (density and viscosity) as those of water.

Table 2: Parameters to ensure dynamic similarity between hepatic sinusoids and the perfusion device

Model	Fluid	Density of fluid	Viscosity of fluid	Diameter of flow channel	Velocity of fluid	Reynolds Number
Hepatic sinusoids (<i>in vivo</i>)	Blood	994 kg/m ³ [29]	3.5-5.5 mPa.s [30]	6.8-11.6 µm [31]	170-2810 µm/s [31]	2.09 × 10 ⁻⁴ to 9.25 × 10 ⁻³
Perfusion device (<i>in vitro</i>)	Cell culture media	1000 kg/m ³ [32, 33]	0.94 mPa.s [33]	2400 µm	0.09-3.86 µm/s	

3.4.2.2 Modelling and Simulation of Flow in the Perfusion Device

The central channel in the physiomimetic liver acinus mesofluidic device is, by design, analogous to a liver sinusoid receiving the nutrient rich blood from the portal vein and draining into the central vein. The flow rate of cell culture media along the biomimetic sinusoidal channel was regulated to ensure that the recirculating flow conditions in the device are dynamically similar to the *in- vivo* physiological conditions. This was achieved by regulating

the flow in the device to have a Reynolds number close to that of the blood flow in the sinusoidal lumen, which, in turn, was achieved by maintaining an inlet velocity of 2.42 $\mu\text{m/s}$.

The triangular compartments on either side of the main biomimetic sinusoidal channel represent the radially arranged cords of hepatocytes separated by adjacent sinusoids in a liver acinus. The geometry of the biomimetic liver perfusion device was generated using Ansys Design Modeler™ (Ansys, Inc., USA), and the mesh for the same was developed using Ansys Meshing. The model consists of a main channel having a rectangular cross section adjoining which there are two triangular compartments representing the cavities to house the biomimetic 3D printed liver acinus model. In the model, the triangular cavities are represented as regions having a porosity of 0.77, in accordance with the experimentally determined porosity of the scaffolds.

In order to understand the flow behaviour and resultant shear stress in the perfusion device, the flow was simulated in the device using computational fluid dynamics (CFD) using ANSYS Fluent 19.2. The central channel was considered filled with the fluid whereas the triangular compartments on the sides of the channel housing scaffolds were modelled as a porous media. It was also ensured that the simulation results were mesh-independent. Since the magnitude of velocity inside the sinusoidal lumen is very low, the flow is bound to be laminar. Thus, the simulation study was carried out considering the flow to be steady and laminar. No-slip boundary condition was applied at the walls of the main channel as well as those of the triangular compartments. The average flow velocity was specified at the inlet whereas pressure (zero gauge pressure) was specified at the outlet boundary.

3.5 Cell seeding in 3D printed biomimetic liver acinus model

3.5.1 Generation of hepatocyte-like cells from human adipose-derived mesenchymal stem cells and their characterization

The human adipose-derived mesenchymal stem cells (ADMSCs) were cultured subsequently in HiPer high glucose Dulbecco's Modified Eagle Medium (DMEM), 10% (v/v) fetal bovine serum (FBS), 1% (v/v) L-glutamine, and 2 ng/ml basic fibroblast growth factor (bFGF). The induction of the ADMSCs (at <5 passage) towards HLCs were done in a two-step protocol, definitive endodermal differentiation for first 7 days followed by hepatocyte differentiation for the next 11 days [7]. For the initiation stage of hepatocyte induction, ADMSCs were cultured in endodermal differentiation media comprising of high glucose DMEM supplemented with

10% (v/v) fetal bovine serum (FBS), 0.1% (v/v) L-glutamine, 10 ng/mL bFGF, 20 ng/mL hepatocyte growth factor, 10^{-7} mM dexamethasone and 10 ng/mL oncostatin M for 7 days. Post 7 days, the endodermal differentiation media was replaced with hepatocyte differentiation media consisting of high glucose DMEM supplemented with 10% (v/v) fetal bovine serum (FBS), 0.1% (v/v) L-glutamine, 40 ng/mL hepatocyte growth factor, 1X ITS, and 10 ng/mL oncostatin M. The medium changes were performed twice weekly and the differentiation of the hepatocytes were assessed by gene expression analysis and immunofluorescence analysis for hepatocyte specific genes and markers respectively.

In case of gene expression analysis, the total mRNA from the ADMSCs and HLCs collected were extracted using TRIzol reagent (Invitrogen, USA) according to manufacturer's instructions. Further, cDNA was synthesized using a high efficiency cDNA reverse transcription kit (Applied Biosystems, USA) and a thermal cycler [14]. Thereafter, quantitative RT-PCR was performed with the set of human hepatic specific primers (Table S1) including albumin, cytochrome P450 2E1, α -fetoprotein (AFP), hepatocyte nuclear factor 4 α (HNF4 α) and an endogenous house-keeping gene human β -actin using power SYBR Green master mix (Applied Biosystems, USA) in a RT-PCR machine. The relative expression of the liver-specific genes was represented following the delta Ct method. Further immunostaining based analysis was performed for ADMSCs, hepatic endodermal cells and matured HLCs for stem cell Sox9 marker, and hepatocyte specific marker albumin, cytokeratin 18, CYP2E1 and HNF4 α . The cells at the 3 different stages were fixed using neutral buffered formalin (NBF), permeabilized with 0.1% (v/v) Triton X-100 in 0.1 M PBS solution and then blocked with blocking buffer consisting of 0.2% (v/v) tween 20, 2% (v/v) horse serum and 1% (w/v) bovine serum albumin (BSA). The primary antibodies used were optimally diluted in blocking buffer and incubated overnight with the cells at 4 °C. The primary antibodies used are (i) mouse anti-Sox9 (1:200 dilution; Santa Cruz Biotechnology, USA), (ii) mouse anti-albumin (1:200 dilution; Abcam, USA), (iii) rabbit anti-CYP2E1 (1:200 dilution; Abcam, USA), (iv) rabbit anti-cytokeratin 18 (1:300 dilution; Abcam, USA), and (v) rabbit anti-HNF4 α (1:1000 dilution; Abcam, USA). Post primary antibody treatment, the cells were incubated with appropriate secondary antibody followed by DAPI counterstaining to stain the nucleus. Finally, the fluorescent images were taken using a ZEISS Axio Observer (Carl Zeiss, Germany) and processed using ImageJ software (NIH, USA).

3.5.2 Culturing of HUVECs and HHSCs

The primary HUVECs and HHSCs were obtained from the ScienCell Research Laboratories, USA. As per ScienCell Research Laboratories, the HUVECs were characterized by immunolabelling for von Willebrand factor (vWF) and cluster of differentiation 31 (CD31) and HHSCs were characterized by immunolabelling for α -smooth muscle actin (α SMA) and Desmin. The HUVECs were cultured and maintained in endothelial cell basal medium (ECBM; ScienCell, USA) supplemented with 1% (v/v) endothelial cell growth supplement, 5% (v/v) FBS and 1% (v/v) penicillin/streptomycin (P/S) solution. Similarly, the HHSCs were cultured in stellate cell basal medium (SCBM; ScienCell, USA) supplemented with 1% (v/v) stellate cell growth supplement, 2% (v/v) FBS and 1% (v/v) P/S solution. Both the cells at <5 passage were used for the study.

3.5.3 Cell seeding protocol and maturation in human physiometric liver microfluidic bioreactor

For validating the concept of “fit-for-purpose” and “context of use”, we selected the optimal ratio of parenchymal and non-parenchymal cells to maximally recapitulate the human liver acinus micro-niche required to maintain the hepatocyte polarity and metabolic function and enable the investigation of drug response required for preclinical trials and precision medicine as per our previous study [7]. The 3D printed scaffolds were sterilized and conditioned overnight in complete culture media composed of high glucose DMEM, ECBM and SCBM in the ratio of 2:1:1 prior to cell seeding. For seeding, the matured HLCs, HUVECs and HHSCs were subsequently trypsinized and resuspended in culture media with a cell density of 2×10^6 cells/construct at a ratio of 10:7:2 respectively. Further, the cell seeded scaffolds were cultured overnight in the maturation medium composed of high glucose DMEM, ECBM and SCBM (2:1:1) supplemented with FBS, growth supplements and P/S solution. Post 24 h of cell seeding, the tricultured biomimetic liver acinus constructs were cultured and matured in either static or dynamic condition in the developed 3D printed physiometric microfluidic bioreactor connected to a recirculating peristaltic pump (3D Biotek, USA) till 15 days to emulate the spatial and temporal microenvironment of the liver acinus. The maturation of the biomimetic cell seeded models in the physiometric condition was achieved by maintaining a flow rate of 100 μ L/h in the peristaltic pump with 40 ml of maturation media in the media reservoirs. After every 5 days, 50% of the media in the reservoirs were replenished with fresh media.

3.6 In vitro biological characterization

3.6.1 Cellular viability and proliferation in the liver acinus model

The cellular viability of the HLCs/HUVECs/HHSCs laden constructs, cultured under static or dynamic conditions for over 15 days was evaluated using calcein AM and ethidium homodimer-1 staining (Thermo Fisher Scientific, USA) as described previously [34]. Briefly, the matured tricultured constructs were washed in 0.1 M PBS and incubated in 40 μ M calcein-AM (stains live cells; green fluorescence) and 20 μ M ethidium homodimer-1 (stains dead cells; red fluorescence) for 30-40 min at 37° C. Following incubation, the dye solution was removed, and the constructs were visualized using a fluorescence microscope ZEISS Axio Observer (Carl Zeiss, Germany) and processed using ImageJ software (NIH, USA) to analyse the distribution of the live and dead cells through the 3D surface plots.

Cellular proliferation of the tricultured constructs cultured in static or dynamic conditions for over 15 days was assessed using the PicoGreen dsDNA assay kit (Thermo Fisher Scientific, USA) as described previously [35]. Briefly, the cell seeded constructs were collected at days 1, 5, 10 and 15 and homogenized in a cell lysis buffer at 4 °C for 4 h. Following digestion, the cell lysates were incubated with PicoGreen fluorescent dye for 10 mins in dark and fluorescence intensity was detected at an excitation/emission wavelength of 490/520 nm using a multiwell plate reader (Tecan Multiplate Reader Infinite M200 PRO, Switzerland). Thereafter, the total DNA concentration was calculated from a standard curve plotted using double stranded λ DNA.

3.6.2 Quantification of albumin and urea secretion levels

The secretion of albumin and urea are the hallmark indicator of the hepatocyte homeostasis [36]. The conditioned media from the HLC/HUVEC/HHSC laden liver acinus model cultured under static or perfusion condition were collected at pre-determined time points to measure the amount of albumin or urea produced [7]. The collected media was further centrifuged at 3000g for 10 min and stored at -80 ° C. To measure the amount of albumin produced, a human albumin enzyme-linked immunosorbent assay (ELISA) kit was used, as per manufacturer's protocol. Briefly, 50 μ L of the cultured media was incubated in the antibody precoated wells for 1 h followed by stepwise treatment of biotinylated albumin antibody, streptavidin conjugate and chromogen substrate for 30, 30 and 20 min respectively. Following treatment, the absorbance was measured at 450 nm using a microplate reader and the unknown albumin concentration was measured from the albumin standard curve.

Similarly, the urea content in the cultured media was estimated using the urea assay kit (Sigma-Aldrich, USA). Briefly, 50 µL of the cultured media was incubated with 50 µL of the reaction mix comprising of substrate, enzyme mix, developer and converting enzyme for 1 h at 37° C under dark condition. Following incubation, the absorbance was measured at 570 nm using a microplate reader and the unknown urea concentration was measured from the urea standard curve. Moreover, the albumin and urea contents were also expressed after normalization with DNA content.

3.6.3 Cytochrome P450 activity measurement

The maintenance of the hepatocyte functions is fundamental for *in vitro* hepatotoxicity evaluation. Therefore, the metabolic activity of the HPLAM cultured under static and perfusion conditions was assessed using the cytochrome P450 reductase assay kit (Abcam, UK) as per the manufacturer's protocol after 1, 5, 10 and 15 d of culture [7]. Briefly, the microsomal fraction of the cell lysate was prepared as per the manufacturer's recommendation. Following isolation, the cell lysate was incubated with a reaction buffer composed of NADPH substrate, CYP assay buffer and glucose-6-phosphate at 37° C for 10 min. After incubation, the absorbance was measured in the kinetic mode at 460 nm for 20 min to determine the CYP activity. Similarly, the CYP activity of all the samples in the presence of 1 mM CYP inhibitor was also determined. Subsequently, the total intracellular protein concentration in the cell lysates were quantified using Bradford's method. The specific CYP activity of the liver acinus model was calculated at the pre-determined time points using the following equation:

$$\text{CYP activity (mU/mg)} = \left(\frac{\Delta A}{\Delta T \times P_C} \right) \text{ (nmol/min/mg)} \quad (8)$$

where ΔA = The amount of glucose-6-phosphate consumed as calculated from the standard graph (nmole); ΔT = Linear phase reaction time (min); P_C = Total intracellular protein concentration in the sample (mg); specific CYP activity = (CYP activity) – (CYP activity in the presence of the inhibitor).

3.6.4 Quantification of LDH activity

Intracellular LDH levels are typically considered as the biomarker for cellular viability. The intracellular LDH activity of the liver acinus model was evaluated at predetermined time points by LDH activity assay kit (Sigma-Aldrich, USA) [7]. For sample preparation, the cell laden

constructs were incubated in cell lysis buffer to obtain the cell lysate as per the manufacturer's protocol. Further the cell lysate was incubated with LDH substrate mix and assay buffer for 2-3 min at 37° C in a horizontal shaker under dark conditions. Post incubation, the absorbance was measured at 450 nm in a kinetic mode. The standard graph generated was used for determining the NADH generated from the unknown samples. Subsequently, the LDH activity of the liver acinus model was calculated using the following equation:

$$\text{LDH activity (milliunits/mL)} = \left(\frac{B}{\Delta T \times V} \right) \quad (9)$$

where B = The amount of NADH (nmole) as calculated from the standard graph; ΔT = reaction time (min); and V = sample volume (mL) per well.

3.6.5 Gene expression studies

The maturation level of the 3D tricultured liver acinus model was determined through liver-specific gene expression and functions analysis. The gene expression profile of parenchymal specific HLC genes (albumin, ALB; cytokeratin 19, CK-19; cytochrome P450 2E1, CYP2E1; cytochrome P450 1A2, CYP1A2; hepatocyte nuclear factor 4 α , HNF4 α); and non-parenchymal HUVEC and HHSC genes (cluster of differentiation 31, CD31; Von Willebrand Factor, vWF; desmin, DES) were determined in liver acinus model cultured under both static and dynamic culture conditions using quantitative RT-PCR (7500 Fast, Applied Biosystems, USA). The mRNA from the tricultured models collected at pre-determined time points were extracted using TRIzol reagent (Invitrogen, USA) according to manufacturer's instructions. Following RNA extraction and quantification, cDNA was synthesized using a high efficiency cDNA reverse transcription kit (Applied Biosystems, USA) and a thermal cycler [28]. Thereafter, quantitative RT-PCR was performed with the set of human specific primers (Table S1) and an endogenous house-keeping gene human β -actin using power SYBR Green master mix (Applied Biosystems, USA) in a RT-PCR machine. The relative expression of the liver-specific genes was normalized against the expression of the respective functional gene at day 1 and the obtained data was represented following the comparative Ct method ($2^{-\Delta\Delta Ct}$).

3.6.6 Gene network prediction analysis

GeneMANIA (<http://www.genemania.org>), a gene function tool that identifies the interacted genes that are related with a set of query genes through its large functional association dataset with respect to co-expression, pathways, co-localization, genetic and protein interactions and protein domain similarity [37]. In this study, the GeneMANIA server was used to determine the possible gene-gene interaction networks functionally associated with the differentially expressed genes (ALB, CK-19, CYP2E1, CYP1A2, HNF4 α , CD31, vWF and DES) analysed using quantitative RT-PCR.

3.6.7 Immunohistochemistry and evaluation of protein-protein interaction networks

3.6.7.1. Immunohistochemistry

Immunofluorescence staining of the tricultured liver acinus model matured for 2 weeks were performed by fixing the sample in neutral buffered formalin. The fixed samples were incubated in 15% (w/v) sucrose made in PBS (pH 7.4) for 6h, followed by 30% sucrose (w/v) in PBS for 12 h. Post incubation, the constructs were embedded in PolyFreeze tissue freezing medium (Sigma, USA) and 15 μ m cryosections were obtained using cryomicrotome (Leica CM1860 UV, Leica Biosystems, Germany). For immunostaining, the cryosections were permeabilized in 0.1% (v/v) Triton X-100 in 0.1 M PBS and blocked in 0.2% (v/v) tween 20, 2% (v/v) horse serum and 1% (w/v) bovine serum albumin (BSA). To determine the distribution of the HLCs and HHSCs in the liver acinus model cultured under static or dynamic conditions, the sections were incubated overnight in primary antibodies, mouse anti-albumin (1:200 dilution; Abcam, USA) and rabbit anti-desmin (1:200 dilution; Abcam, USA) at 4 °C. The sections were further incubated in appropriate secondary antibody at 1:200 dilutions. In order to determine the vascularization in the liver acinus model, the sections were immunolabelled overnight with the respective primary antibodies, mouse anti-albumin (1:200 dilution; Abcam, USA) and rabbit anti-vWF (1:200 dilution; Abcam, USA) or rabbit anti-CYP2E1 (1:100 dilution; Novus Biologicals, USA) and mouse anti-CD31 (1:200 dilution; Abcam, USA) at 4 °C and further incubated with appropriate secondary antibody at 1:200 dilutions. The distribution of the NPCs, i.e. HHSCs and HUVECs, were also analysed by immunostaining the sections with primary antibodies against rabbit anti-desmin (1:200 dilution; Abcam, USA) and mouse anti-CD31 (1:200 dilution; Abcam, USA) and, further with appropriate secondary antibodies at 1:200 dilution. All the sections were also counter stained with DAPI ((4',6-diamidino-2-phenylindole) to stain the nucleus. The immunofluorescence images were visualized and captured using ZEISS Axio Observer (Carl Zeiss, Germany) and processed using ImageJ software (NIH, USA) to analyse the co-distributions of the cells and the 3D surface plots.

3.6.7.2. Protein-protein interaction (PPI) network analysis

The STRING database (Search Tool for the Retrieval of Interacting Genes/Proteins; version 12.0) collects, scores and integrates all publicly accessible data of known and predicted PPI based on co-expression, experiments, text-mining and other previously curated knowledge [38]. In the current study, the STRING database was also used to determine the protein-protein interaction network of the target proteins (ALB, CK-19, CYP2E1, CYP1A2, HNF4 α , CD31, vWF and DES) encoded by the differentially expressed genes in the matured tricultured liver acinus model. Additionally, the gene enrichment functional analysis was also evaluated to determine the pathways and the biological processes the differentially expressed genes contribute to. The results obtained were further collated and analysed.

3.6.8 Evaluation of drug-induced liver injury on the human physiometric liver acinus model

To determine the drug responsiveness of the liver acinus model, the tricultured model was matured for 10 days and exposed to various types of drugs in static or dynamic bioreactor condition for 24 h and 72 h. Hepatotoxicity testing was performed using non-hepatotoxicants (dexamethasone and aspirin), idiosyncratic hepatotoxicant (trovafloxacin mesylate) and hepatotoxicants (acetaminophen and troglitazone). C_{max} , the highest drug concentration reached in the plasma, is employed as the therapeutically appropriate margin for drug safety evaluation. Taking into consideration the underlying risk factors for DILI, human C_{max} , $100 \times C_{max}$ or above $100 \times C_{max}$ drug dosing concentrations were chosen to negate the effect of the risk factors in our *in vitro* physiometric model as per our previous study and reports [7, 39]. The concentration of the various types of drugs used for drug response study are provided in **Table 3**. All the drugs were procured from Sigma-Aldrich, USA and dissolved in dimethyl sulfoxide to prepare stock solutions. Following drug exposure to the matured liver acinus model, the effects were evaluated by estimating cell viability, LDH activity assay and CYP activity. The cellular viability, LDH activity and CYP activity of the liver model without drug exposure was considered as internal control to the drug treated samples. Afterwards, the tricultured matured liver constructs following drug treatment were homogenized in cell lysis buffer and assessed for viability of the cells by quantifying the DNA concentration using the Quant-iT PicoGreen dsDNA assay kit. Further, the drug dosing concentration showing a decrease in 50% cell viability (EC_{50}) was determined using a non-linear curve fitting method following the dose-response model from a plot of percentage of cell viability (Y) versus concentration of drug (X) using OriginPro 2021 software. The drug treated matured tricultured

models were also assessed for LDH activity and specific CYP activity using the LDH assay kit and CYP activity assay kit as per the protocol explained in methodology section 2.5.3 and 2.5.4 respectively. Further, for comparison among the static and perfusion group, the DNA concentration, LDH activity and CYP activity data from the drug treated groups were normalized with the values obtained from the internal control.

Table 3: List of small molecule drugs and their concentrations used for drug response assessment in the physiomimetic liver acinus model. The drugs are also classified and ranked by their risk for causing DILI as per DILIRank dataset [16], where severity class 0 corresponds to drugs with no DILI and severity class 8 corresponds to drugs with severe clinical DILI.

Sl. No.	Type of Drugs	PubChem_CID	Drugs	DILI concern	Severity Class	Drug Label section	Human Cmax (μ M)	100 x Human Cmax (μ M)	Concentrations tested (μ M)
1.	Non-hepatotoxicants	2244	Aspirin	No-DILI-Concern	0	No match	5.53	552.60	5.53, 552.60, and 1000
2.		5743	Dexamethasone	Less-DILI-Concern	3	Adverse reactions	0.22	22.40	0.22, 22.40, and 500
3.	Idiosyncratic hepatotoxicant	62959	Trovafloxacin mesylate	Most-DILI-Concern	8	Withdrawn	4.08	407.80	2, 4.08, 100, and 407.80
4.	Hepatotoxicants	1983	Acetaminophen	Most-DILI-Concern	5	Warnings and precautions	139	13900	139, 5000, 10000, and 13900
5.		5591	Troglitazone	Most-DILI-Concern	8	Withdrawn	6.39	638.70	6.39, 50, 100, and 638.70

4. Statistical analysis

All the experiments shown in this study are carried out in experimental or biological triplicates, unless otherwise mentioned. All the data from the analysis are presented as mean \pm standard deviation (SD). For determining statistical significance, one-way analysis of variance (ANOVA) via Tukey's test was performed (OriginPro 2021, OriginLabs, USA) and the results between the groups were considered statistically significant at $p \leq 0.05$, $p \leq 0.01$, and $p \leq 0.001$.

5. Results

5.1. Decellularized liver extracellular matrix mimetic biomaterial ink exhibits shear thinning behaviour with excellent thixotropic recovery and high print fidelity for 3D printing

The field of 3D printing liver tissue models requires a suitable biomaterial ink that closely emulates the native tissue micro-niche and mechanics as well as exhibits high print fidelity. The limitations of the current commercial biomaterial inks are that they lack ECM like components which facilitate cell-cell interaction and cell-matrix interaction vital for tissue formation and maturation. [7, 40] Among the various biomaterials available, decellularized liver extracellular matrix has been one of the most ideal components for biomaterial ink fabrication due to its excellent cytocompatibility. [41] Thus, to formulate a liver mimetic biomaterial ink, porcine liver was decellularized by using a chemical decellularization method followed by enzymatic solubilization to obtain liver ECM-derived microparticles. The resulting ECM microparticles were assessed for decellularization through histological and biochemical assays (**Figure S1**). Following decellularization, the DNA content in the decellularized ECM was significantly reduced ($p \leq 0.001$) to 33.16 ± 3.49 ng/mg of dry weight compared to 966.8 ± 22.05 ng/mg of dry weight in the native liver (**Figure S1A**). In accordance with the previous reports, the content of DNA in the decellularized tissue was within the permissible limit of 50 ng/mg of tissue. [42] The total protein, sGAG and collagen content in the decellularized liver tissue was estimated to be 49.72 ± 4.50 μ g/mg, 2.97 ± 0.21 μ g/mg, 3.34 ± 0.25 μ g/mg in comparison to 56.18 ± 5.18 μ g/mg, 2.75 ± 0.3 μ g/mg, 2.3 ± 0.31 μ g/mg in the native liver (**Figure S1B – D**). The collagen content of the dECM was higher than the native liver due to the increased exposure of only ECM without any cellular components. Similar results have been reported previously as well. [24] Also, the total protein content and sGAG content of the decellularized liver was found to be similar with the native liver, confirming the efficacy of the decellularization method in preserving ECM components. Furthermore, the Alcian blue and picrosirius red staining also

confirmed the preservation of sGAG and collagen post decellularization (**Figure S1E**). Thus, the decellularized liver ECM had a biochemical composition similar to that of native liver. However, only decellularized ECM biomaterial inks have disadvantages in terms of poor printability, weak mechanical stability and slow crosslinking speed resulting in limited shape fidelity and scalability. [43] Therefore, a multicomponent hybrid liver mimetic biomaterial ink was developed for achieving ideal physiological relevance and optimal printability.

The multifunctional liver mimetic biomaterial ink was developed using regenerated *B. mori* SF, dECM and a bulking agent gelatin (**Figure 2A**). *B. mori* silk fibroin being a fibrous protein is not only biocompatible and biodegradable but it also provides mechanical resiliency, stability and viscoelasticity to the biomaterial ink. [44]. As already discussed, the incorporation of ECM in the ink provides a physiomimetic microenvironment which enhances cell-cell interaction, cell matrix interaction and overall tissue maturation. [24] Furthermore, gelatin was used as bulking agent as well as viscosity enhancer to significantly improve the printability of the silk-liver ECM based biomaterial ink. [45] The formulated biomaterial ink was systematically characterized for its compositional, printability and rheological properties (**Figure 2Bi**). The compositional features of the crosslinked and non-crosslinked bioinks were confirmed using fourier-transform infrared (FTIR) spectroscopy (**Figure 2Bii**). The secondary structures of the crosslinked biomaterial ink with the signature β -sheet peaks were observed at 1617 cm^{-1} (amide I; C=H stretching), 1517 cm^{-1} (amide II; C=N stretching) and 1231 cm^{-1} (amide III; C-N stretching) which were found to be shifted from 1641 cm^{-1} (amide I), 1537 cm^{-1} (amide II) and 1241 cm^{-1} (amide III), respectively. Similarly, the discrete *B. mori* SF and gelatin also showed peaks at amide I, II and III, which are the characteristic peaks of proteins. The characteristic peak for liver dECM was observed at $1340 - 1420\text{ cm}^{-1}$ indicating the presence of methyl group. [24] Overall, the typical amide and methyl group peaks of the constituent polymers (*B. mori* SF, dECM and gelatin) were observed in the biomaterial ink. The conformational changes (shift in the amide peaks) in the biomaterial ink after EDC/NHS cross-linking confirmed β -sheet induction leading to the integral stability of the biomaterial ink. [24, 45]

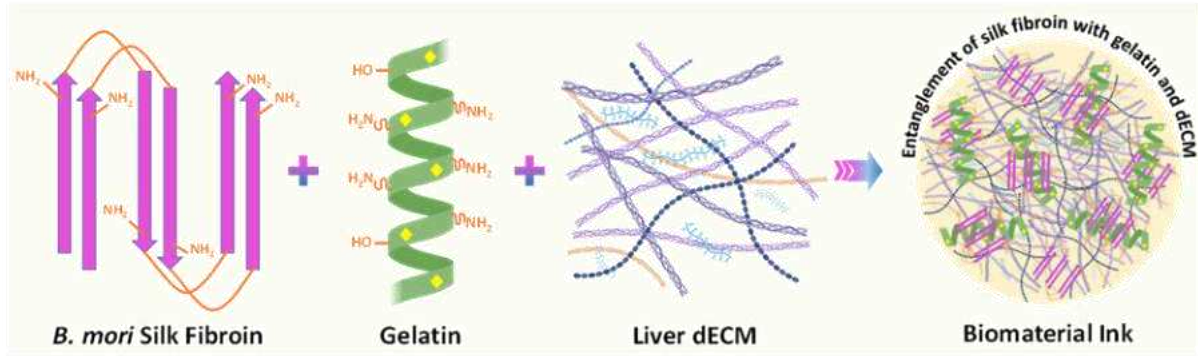
Further, the printability of the biomaterial ink was investigated from a range of concentrations of *B. mori* SF, dECM and gelatin to identify the ink concentrations with suitable viscosity for 3D micro-extrusion based printing. The printability of the biomaterial ink was assessed based on gelation, shear-thinning behaviour, self-standing nature, print fidelity and resolution. For evaluation, the printing conditions were categorized into (i) non-printable, (ii) printable, but

shape not in agreement with the CAD model and (iii) printable (**Figure 2Biii**). The concentration of gelatin at 5% and 7% along with SF and dECM concentration at 1% and 3% yielded a viscous biomaterial ink optimal for 3D printing self-standing structures with high print fidelity and resolution. While the concentration of gelatin below 5% and SF below 3% yielded a viscous biomaterial ink, but the printed structures were not in agreement with the CAD model. Further, the concentration of gelatin below 3% resulted in low viscosity non-printable inks as well as the concentration of SF and dECM above 3% resulted in very high viscosity non-printable inks. Overall, the printability of the ink composition was found to be ideal at 3% (w/v) B. mori SF, 5% (w/v) dECM and 3% (w/v) liver dECM. The printed constructs with the optimal concentrations had shear thinning behaviour with high print fidelity and resolution.

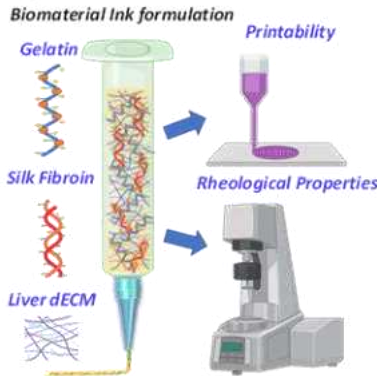
Further the flow properties or deformation of the developed biomaterial ink was assessed through rheological characterization where the storage modulus (G') and the loss modulus (G'') associated with elastic and viscous behaviour respectively were recorded for different testing conditions (**Figure 2C**). First, the temperature sweep was performed to determine the temperature dependent complex viscosity of the biomaterial ink. Both the G' and complex viscosity were found to decrease with the increase in the temperature (**Figure 2Ci and ii**). It was noted that the biomaterial ink maintained its integrity (indicated by the high G') below $\sim 25^\circ\text{C}$ and gradually became fluidic (indicated by the higher G'') when the temperature was raised over that. Moreover, the complex viscosity was also found to be optimal in the temperature range of $18\text{--}22^\circ\text{C}$. This temperature dependent gelation behaviour is mainly attributed to the gelatin component in the biomaterial ink. The viscosity of the biomaterial ink decreased as the gelatin undergoes sol-gel transition with the increase in the temperature. Thus, the ink exhibited shear thinning effect at a temperature range of $18\text{--}22^\circ\text{C}$. The linear viscoelastic region (LVER) of the biomaterial ink was determined through amplitude sweep wherein G' and G'' as well as complex viscosity were plotted against strain value (γ). At low shear stress the G' of the ink was dominant indicating a more elastic nature of the ink. With the increase in the γ value, the biomaterial ink gradually deformed, resulting in decreased G' value and complex viscosity. This viscoelastic transition assured the shear thinning behaviour of the biomaterial ink. Both the complex viscosity and the G' decreased after $\sim 100\%$ of γ , and the yield point or the crossover point was noted at $\sim 300\%$ of γ (**Figure 2Ciii and iv**).

The LVER of the biomaterial ink was found to be decent and in the range of 0.1 – 100% of γ . The LVER range portrays stability in terms of prevention of ink sedimentation and the ink totally deforms and become fluidic beyond the range exceeding the yield point due to applied strains. Further, the frequency sweep of the biomaterial ink was evaluated to determine the frequency dependent viscoelastic behaviour at a fixed strain. The biomaterial ink showed no angular distortions till 100 rad.s⁻¹ and the G' was dominant over G'' at all frequencies, assuring the robustness of the biomaterial hydrogel (**Figure 2Cv**). Furthermore, the thixotropic nature of the biomaterial ink was assessed (**Figure 2Cvi**) and the biomaterial inks were found to have rapid recoverability property post deformations caused by high shear strains for different time durations. Thus, the biomaterial inks post printing would not laterally diffuse. Overall the rheological assessment revealed that the developed biomaterial ink possessed shear thinning behaviour with rapid thixotropic recovery required for developing self-standing constructs with high print fidelity.

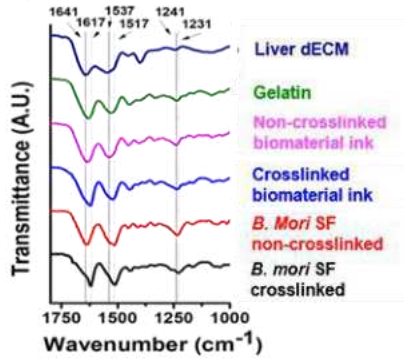
A)



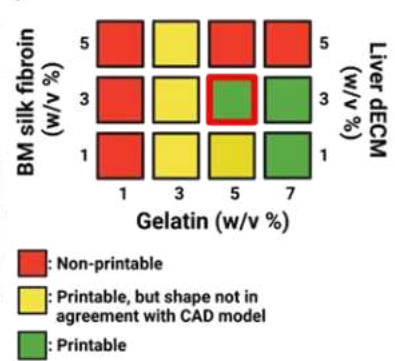
B) i)



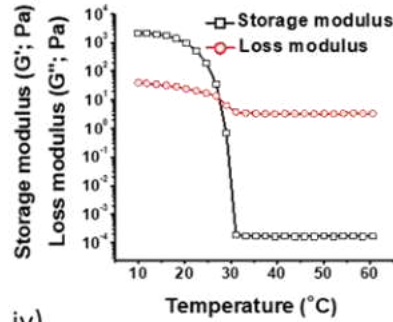
ii)



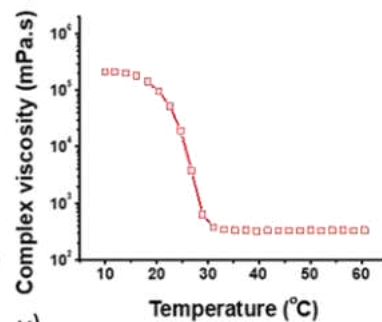
iii)



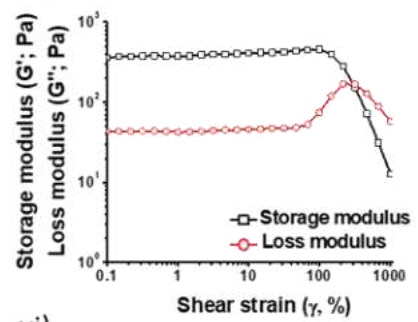
C) i)



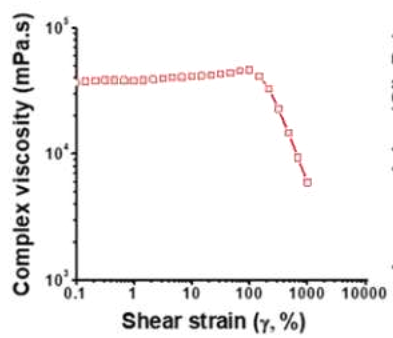
ii)



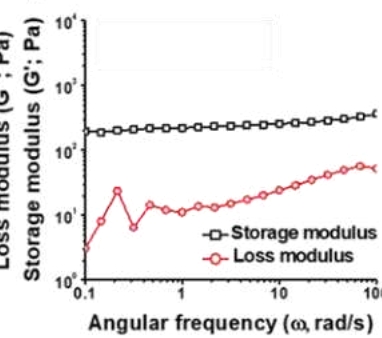
iii)



iv)



v)



vi)

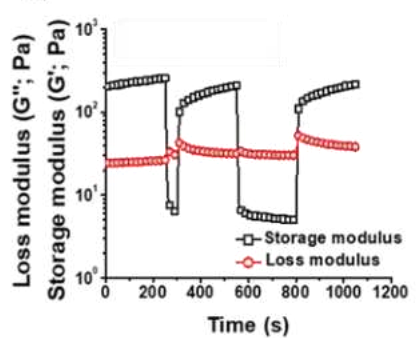


Figure 2: Formulation, optimization and characterization of the multifunctional liver mimetic biomaterial ink; A) Schematic depicting the formulation of the biomaterial ink; B) Characterization of the biomaterial ink for its compositional, printability and rheological properties, (i) illustration representing biomaterial ink formulation and its characterization; (ii) fourier infrared spectrographs of the individual components and both crosslinked and un-

crosslinked biomaterial ink; (iii) Printability chart of the different concentrations of SF, gelatin and liver dECM; C) Rheological characterization of the biomaterial ink; i) Temperature sweep profile, ii) complex viscosity vs temperature iii) amplitude sweep profile, iv) complex viscosity vs shear strain v) frequency sweep profile and vi) thixotropic property analysis at alternate cycles of low and high oscillating shear and angular frequency.

5.2 3D printing of biomimetic liver acinus construct using liver extracellular matrix mimetic biomaterial ink confers in vivo like physiological relevance

The liver acinus is the smallest functional unit of the liver which is composed of the hepatic arteriole, bile duct, central vein, liver sinusoid, space of Disse and multiple cells types including hepatocytes, sinusoidal endothelial cells, hepatic stellate cells, Kupffer cells and cholangiocytes. The liver sinusoid is formed by the combined entry of blood from the portal vein and the hepatic artery, which ultimately flows into the central vein. [10, 46] Recapitulation of the native tissue microarchitecture is one of the prime prerequisites for dictating tissue functions. [47] Therefore, development of a biomimetic liver model where the physical and mechanical properties and the cellular distribution mimics the microarchitecture and organization of the cells in the liver acinus altogether helps in maintaining its functionality in vitro (**Figure 3**). In the current study, we developed a liver acinus mimetic CAD model which recapitulates the native hierarchical arrangement of the cords of hepatocytes separated by functional sinusoidal microvasculature networks (**Figure 3A**). 3D printing of the acellular biomimetic hepatic acinus construct was done using the silk-liver dECM based biomaterial ink. The printed constructs post crosslinking were highly stable and maintained their architecture and dimensions as per the CAD model (**Figure 3B**). In the printed construct the dimensions of the base, perpendicular, hypotenuse and height were found to be approximately 10 mm, 10 mm, 14 mm and 5 mm in physiologically relevant environment. The 3D printed construct closely recapitulated the hepatic cord in the form of filaments along with the hepatic sinusoidal networks and space of Disse in the form of inter filament spacing. Further FESEM characterization revealed that the multi-layered assembly of the acellular construct was comprised of parallelly arranged filaments with an inter filament distance of $\sim 200\ \mu\text{M}$ to facilitate the paracrine signalling among the seeded parenchymal and the non-parenchymal cells. The constructs also depicted uniformly distributed interconnected micro pores of $\sim 100\ \mu\text{M}$, which is suitable for parenchymal and non-parenchymal cells infiltration, attachment and migration. [24, 48] (**Figure 3B**) Further, the scaffolds also demonstrated high porosity in the

range of 70-80%, which is suitable for uniform cell distribution and migration in the constructs along with the exchange of oxygen and nutrients (**Figure S2A**).

The 3D printed constructs were also physiochemically and mechanically characterized. The swelling, degradation and mechanical properties of the constructs are essential requirements for the development of a suitable matrix for tissue engineering applications. The porosity of the constructs also plays a vital role in determining the swelling, degradation and mechanical properties of the constructs. The 3D printed constructs showed a rapid swelling (swelling ratio of ~ 4) in the initial 3 h and then attained a maximum swelling (swelling ratio of ~ 6) in about 12 h (**Figure S2B**). Optimal swelling capacity was observed due to the high porosity which allows for better exchange of oxygen and nutrients between the seeded cells and the cellular medium. [49] The long-term stability of the 3D printed constructs was assessed by evaluating both degradation and protein leached out from the 3D printed constructs. The crosslinked constructs did not show any significant degradation for over 28 days. The constructs degraded $\sim 10\%$ of the initial weight (w/w), suggesting the optimal stability of the scaffolds for performing prolonged in vitro studies (**Figure S2C**). Further the protein leached out from the 3D printed constructs was less than 0.3% (w/w) of the initial weight of the constructs, suggesting an insignificant loss of protein and confirming the integral stability of the constructs post crosslinking (**Figure S2D**).

The stiffness of the substrate also plays a crucial role in preserving the in-vivo like phenotype and bioactivity of hepatocytes. [50, 51] It has also been reported that stiff substrates attenuate the phenotype and function of hepatocytes and cause increased apoptosis. [52, 53] In this regard, the compressive and tensile strength was evaluated in both 3D printed constructs with vertically aligned filaments or horizontally aligned filaments. The compressive and tensile modulus were calculated from the stress-strain curve of the different types of specimen. To evaluate the compressive stress-strain response of the constructs, a compressive strain of up to 30% was applied in both the 3D printed constructs with vertically aligned filaments or horizontally aligned filaments (**Figure 3Ci**). Under hydrated condition the 3D printed constructs with vertically aligned filaments demonstrated a compressive modulus of 101.14 ± 9.56 kPa, significantly higher ($p \leq 0.001$) than the 3D printed construct with horizontally aligned filaments having compressive modulus of 31.3 ± 3.11 kPa (**Figure 3Cii**). The compressive modulus of the 3D printed constructs with vertically aligned filaments was found to be similar to the reported compressive modulus of the native human liver. [54]

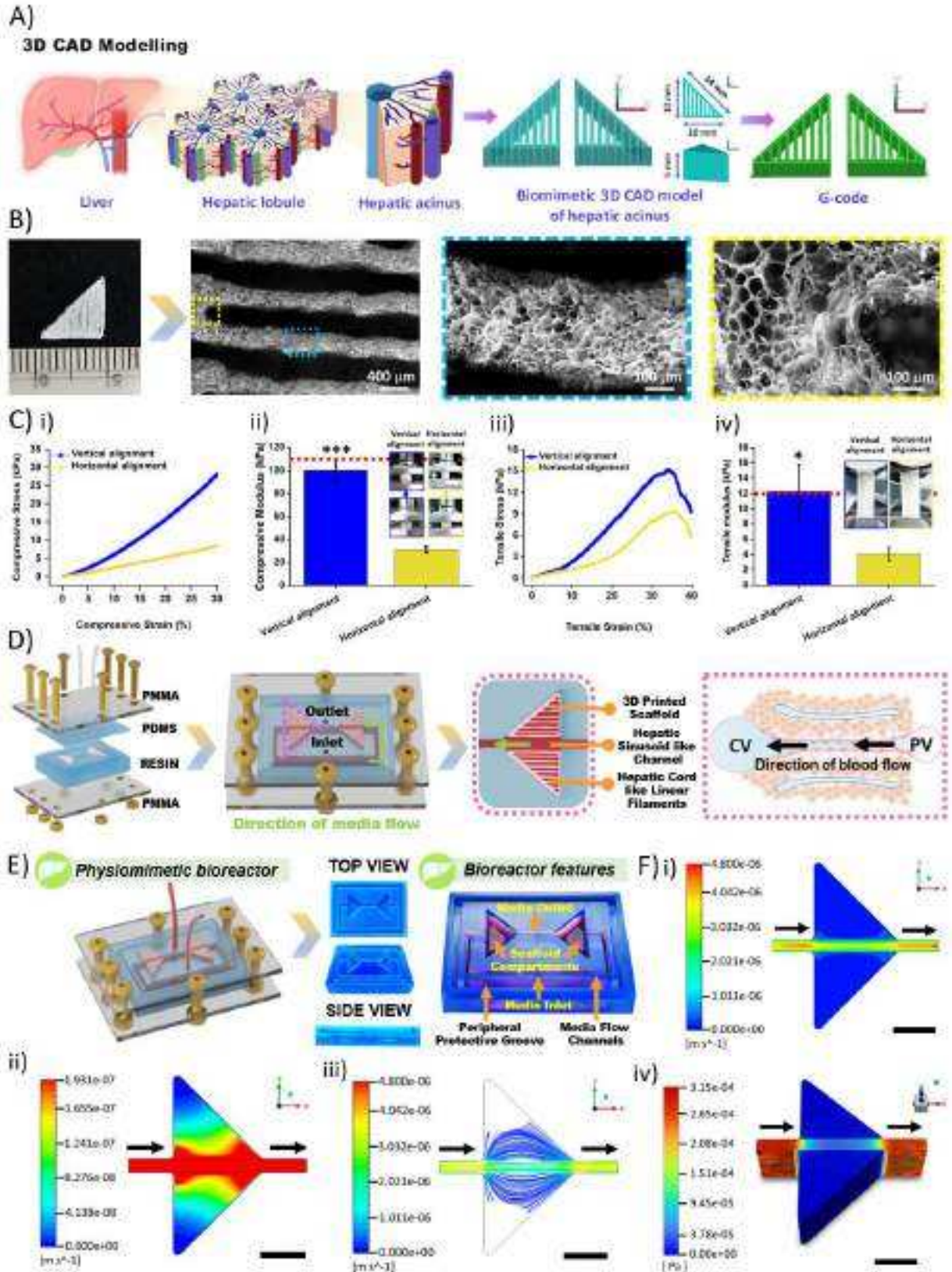


Figure 3: Native human liver acinus microphysiological environment inspired conceptualization of the biomimetic liver acinus scaffold and physiomimetic liver acinus microfluidic bioreactor CAD design, 3D printing and its characterizations; A) Schematic

*illustration of the CAD design of the 3D biomimetic liver acinus construct closely recapitulating the hepatic cord in the form of filaments along with the hepatic sinusoidal networks in the form of spaces in between the adjacent filaments; B) Representative digital image and FESEM images of the freeze-dried 3D printed construct representing the gross surface morphology and the interconnected pores in the filaments. Scale bar: 400 μ m and 100 μ m respectively; C) Mechanical properties of the silk, gelatin and liver dECM based 3D printed constructs, i) representative compressive stress-strain curves, ii) compressive moduli, iii) representative tensile stress-strain curves and iv) tensile moduli; D) Schematic illustration of the conceptualization, development and assembly of the liver acinus microfluidic bioreactor CAD model based on the key biological and physiological phenomena and flow conditions in the native liver acinus microenvironment;; E) Representative image portraying the assembled liver acinus microfluidic bioreactor and digital photographs of the bottom part of the microfluidic bioreactor with annotations of the device features. F) Analysis of flow in the microfluidic bioreactor as per CFD simulations, i) and ii) flow velocity exhibiting a decreasing trend with increasing distance from the channel, iii) streamline plot of the flow and iv) distribution of wall shear stress suggesting near-static flow conditions in the scaffolds. Scale bar: 5 mm. The arrows represent the direction of the flow of the media. Data is expressed as Mean \pm S.D (n = 4); where statistically significant difference is represented by * $p \leq 0.05$, ** $p \leq 0.01$ and *** $p \leq 0.001$.*

The tensile stress-strain responses of the crosslinked 3D printed dumbbell shaped constructs were evaluated in hydrated condition until breakage of the constructs (**Figure 3Ciii**). Further, under hydrated condition the 3D printed constructs with vertically aligned filaments demonstrated a tensile modulus of 12.24 ± 3.56 kPa, significantly higher ($p \leq 0.05$) than the 3D printed construct with horizontally aligned filaments having tensile modulus of 4.09 ± 0.89 kPa (**Figure 3Civ**). Intriguingly, the tensile modulus of the 3D printed construct with vertically aligned filaments was also found to be in alignment with the reported tensile modulus of the native human liver. [54] Thus, the compressive modulus and the tensile modulus of the 3D printed constructs with vertically aligned filaments were similar with the native human liver, suggesting it to be a physiologically relevant substrate for long term hepatocyte culture with maintenance of phenotype and bioactivity. [53-55]

5.3 Human physiometric liver acinus microfluidic platform recapitulated key biological phenomena of native liver acinus

It has been well reported that the data obtained from simple 2D and 3D *in vitro* experimental models are not concordant with the results from human phase clinical trials. The main reason is attributed to the loss of viability and functionality of the cells over extended periods, lacks recapitulation of the microarchitecture of the liver and loss of secretome components after media replenishment. Most importantly, static dense 3D models are even deprived from optimal nutrient and oxygen transport and lack physiologically relevant shear stress required for optimal

hepatocyte physiology. Therefore, recently microphysiological liver models have been developed to overcome the challenges faced in oversimplified static in vitro models. Particularly, in comparison to static 3D models, these dynamic platforms have better physiological relevance and high reproducibility. However further implications in cell-cell and cell-matrix interaction, physiologically relevant fluid flow and microarchitecture mimicry have not yet been taken into consideration to obtain a physiomimetic liver dynamic model. [10, 56]

At a coarse-grain view, the conceptualization and development of the physiomimetic model of the liver acinus microfluidic bioreactor in our study was based on the consideration of the following biological phenomena and key characteristics: (i) flow conditions are directionally and dynamically biomimetic to the human liver sinusoid microenvironmental conditions; (ii) recapitulation of the physiological shear stress effects of circulation in sinusoids, including physical microenvironmental cues i.e. influence hepatocytes and non-parenchymal cells physiology for the production and transport of secretome and signalling molecules; (iii) ability to evaluate potential drug candidates in a controlled environment; (iv) ability of the microphysiological 3D liver acinus model to promote cell-cell interaction, cell-matrix interaction and respond to drug reactions of human relevance; (v) recirculating media flow to enable the concentration of secreted factors and metabolites; and (vi) ability to disassemble the microfluidic platform for extracting cell laden constructs and media for biological and molecular characterization and estimation of key elements of the secretome (**Figure 3D**). Taking into consideration the aforementioned biological phenomena and key characteristics, a micro-physiomimetic liver acinus bioreactor platform was designed, and 3D printed using a SLA based 3D printer. The dimensions of the 3D printed micro-physiomimetic liver acinus bioreactor platform are mentioned in **Figure S3**. The complete microfluidic bioreactor device, consisting of the top and bottom layer, was assembled by stacking the 3D printed bottom layer and the complementary PDMS top layer in between two 2 mm poly (methyl methacrylate) (PMMA) sheets and compressed tightly using eight screws to prevent potential media leakage (**Figure 3D and E**) (**Video S1**). The two-layered design allowed for the easy disassembly of the device to retrieve the cell laden constructs and media for biological and molecular characterization. In addition, it also allowed the 3D printed device to be reused following proper cleaning and sterilization.

The microfluidic bioreactor platform consisted of an inlet port, four scaffold chambers, fluid flow channels and an outlet port which mimicked the portal vein, hepatic acinus like geometry, hepatic sinusoids like networks and the central vein respectively. Further a peripheral protective groove was fabricated in the bottom 3D printed layer onto which a complementary peripheral ridge of the PDMS top layer fits in to protect the culture from contamination. Overall, the flow pattern of the culture media from the inlet port to the outlet port through the scaffold chambers in the microfluidic bioreactor platform mimicked the native physiological flow pattern. [10] The recirculating flow of media in the channels and the scaffold compartments was achieved through a recirculating peristaltic pump for enhanced accumulation of secretome and metabolites. During the perfusion of the media through the channels it was ensured that there is no detectable media leakage.

The in vivo blood flow conditions were dynamically and directionally emulated by maintaining the flow rate of perfusion cell culture media at 100 $\mu\text{L}/\text{h}$ as previously described in materials and methods. This physiologically relevant fluid flow mimics the physiological shear stress which in turn helps in preserving the parenchymal and non-parenchymal cells phenotype and physiology for improved in vitro functionality. Moreover, the principal advantage by mimicking the physiologically relevant condition is that it promotes cell-cell interaction, cell-matrix interaction and allows the model to respond to drug reactions in an in vivo like cellular microenvironment. [56] To recapitulate the physiological shear stress effects of circulation in sinusoids, including physical microenvironmental cues, computational flow simulation was performed (**Figure 3F**). The flow simulation was carried out to determine the values of wall shear stress and velocity inside the microfluidic device. In the vicinity of sinusoid, there is negligible flow of fluid in the adjoining scaffold (**Figure 3Fi**). Consequently, there is negligible transport of nutrients and oxygen to the distal cells via convection. The simulation results show that the largest magnitude of velocity is found inside the main channel and, expectedly, the magnitude of velocity becomes smaller as the distance from the channel increases (**Figure 3Fii**). Moreover, the streamline plot confirms that there is practically no flow in the distal half of the scaffold compartments (**Figure 3Fiii**). Moreover, the wall shear stress is negligible in the triangular cavities, indicating there is negligible to no flow in those regions (**Figure 3Fiv**). In the device, low shear stress also ensures that the cells do not get dislodged from the scaffolds due to the flow of media.

Overall, these results suggest that the transfer of oxygen or nutrients inside the scaffolds is predominantly diffusion-driven and the flow characteristics mimicked the in vivo blood flow pattern in the hepatic sinusoids. [57, 58] It is understood that the cells adjacent to the flow channel are exposed to higher concentrations of oxygen than the distal cells, as the fluid in the channel is oxygen- and nutrient-rich. Upon consumption of nutrients by the cells, their concentration gets replenished more readily in the regions proximal to the channel than the distal ones, resulting in a concentration gradient which, in turn, drives the diffusion process. Thus, the resulting human physiomimetic platform allowed for the selective integration of key physiological and structural features of the human liver acinus. Moreover, based on the classification of microphysiological systems, our device can be categorized under “next generation structured human biomimetic liver microphysiological systems”. [10]

5.4 *In Vitro* Functional Validation of Tricultured HPLAM Showed Cellular Alignment with Intrinsic Pattern Maintenance, Enhanced Proliferation, Maturation and Sustained Higher Level of Albumin, Urea, Cytochrome P450 and LDH activity

As per our previous reports, [7, 24] silk fibroin and liver dECM based culture platforms have demonstrated the efficiency of the 3D formats in enhanced maintenance of the parenchymal and non-parenchymal cells phenotype and functionality. Hepatocytes, endothelial cells and hepatic stellate cells account for more than 80% of the liver mass and it has been reported from our previous study that HLCs in a triculture with HUVECs and HHSCs, remain viable and maintain hepatic specific functions for prolonged durations. [7] In the current study, to closely recreate the liver acinus microenvironment, we developed a 3D tricultured liver acinus model that possesses the physiologically relevant cell combination and microarchitecture for enhanced cellular alignment with the biomimetic structure and improved long term physiological functionality. As reported earlier, a true cell culture platform of liver model uses high cell densities and dynamic platform to allow the active transport of nutrients, metabolites and oxygen as well as overcome the limitations of diffusion [20]. Based on this consideration, the 3D printed scaffolds were seeded with matured HLCs, HUVECs and HHSCs at a cell density of 2×10^6 cells/construct at a ratio of 10:7:2 respectively (**Figure 4B**). Further, the tricultured scaffolds were matured in either static or dynamic condition in the developed 3D printed physiomimetic microfluidic bioreactor connected to a recirculating peristaltic pump till 15 days

to emulate the spatial and temporal microenvironment of the liver acinus (**Figure 4A and 4Di**).

To better evaluate the cellular activities following seeding, cell viability and cellular proliferation were assessed initially. The viability and the alignment of the cells in the tricultured liver acinus model matured was evaluated via live dead staining following 15 days of maturation (**Figure 4C**). The viable parenchymal and non-parenchymal cells were seen to uniformly align and colonize in the pore walls along the filament in an aligned structure, similar to the linear cord-like arrangement of the hepatocytes within a hepatic sinusoid network. In both the static and perfusion groups, minimal cell-death was observed. As per the fluorescent live/dead images captured, the perfused liver model (**Figure 4Ci**) group presented better aligned and more uniformly distributed cells than that of static group (**Figure 4Cii**), suggesting the need of perfusion based physiological shear stress for enhanced cellular viability, alignment and distribution. Moreover, the uniform cellular distribution and alignment of the cells along the filaments, would further enhance cell-cell interaction for emulating the 3D cellular architecture of the live acinus microenvironment. Further the quantification of the viability and proliferation of the cells in the liver model was performed by DNA quantification assay using PicoGreen-based DNA kit. In the static as well as perfused group, significantly enhanced ($p \leq 0.001$) proliferation of cells was observed on day, 5, day 10 and day 15 in comparison to day 1 (**Figure 4Dii**). Comparatively, the perfused liver acinus group showed statistically enhanced ($p \leq 0.05$) proliferation of cells on day 5 ($1.59 \pm 0.08 \mu\text{g}$), day 10 ($2.17 \pm 0.06 \mu\text{g}$) and day 15 ($2.52 \pm 0.09 \mu\text{g}$) in comparison to the static group on day 5 ($1.35 \pm 0.07 \mu\text{g}$), day 10 ($1.94 \pm 0.06 \mu\text{g}$) and day 15 ($2.27 \pm 0.07 \mu\text{g}$), respectively. The enhanced cellular viability, colonization and proliferation in the perfusion group is attributed to the enhanced paracrine interaction and other signalling molecules generated due to cell-cell interaction and cell-matrix interaction as well as the accumulation of increased secreted factors and metabolites from the multiple cells. Moreover, the enhanced cell viability, colonization and proliferation results altogether confirm the cytocompatibility of the biomaterial ink due to the intrinsic cues provided by the liver dECM microparticles.

The production of albumin and urea are the hallmark indicator of the hepatocyte homeostasis. [36] With the aim of assessing the liver specific physiological functions, including synthetic functions, nitrogen metabolism and detoxification ability of the tricultured liver acinus model in the static and perfusion culture over a period of 15 days, we measured the CYP activity, LDH

activity and the amount of albumin and urea produced and compared it with the estimated values in human in vivo condition (**Figure 4D**). The total albumin content produced from the tricultured liver acinus model cultured in static or perfused condition increased significantly on day 5, day 10 and day 15 respectively as compared to day 1 ($p \leq 0.001$) (**Figure 4D iii**). Intriguingly, the quantitative amount of human albumin produced in perfused condition on day 5 ($6.58 \pm 0.69 \mu\text{g}$), day 10 ($14.07 \pm 0.53 \mu\text{g}$) and day 15 ($20.25 \pm 1 \mu\text{g}$) was significantly higher (atleast $p \leq 0.05$) than the albumin produced in static condition on day 5 ($4.09 \pm 0.63 \mu\text{g}$), day 10 ($8.76 \pm 0.80 \mu\text{g}$) and day 15 ($12.94 \pm 0.87 \mu\text{g}$). Moreover, significantly increased ($p \leq 0.001$) albumin secretion was also observed in both static and perfused group on day 5, 10 and 15 in comparison to day 1, when the total albumin produced was normalized with the total DNA content in the liver acinus model respectively (**Figure 4D iv**). Similarly, significant increase (atleast $p \leq 0.05$) in DNA normalized albumin secretion levels of the perfused model in comparison to static model was observed on day 5, 10 and 15. Overall, the albumin produced in the perfused HPLAM on day 10 and day 15 was similar to the albumin production levels observed in human liver in vivo conditions ($\sim 20\text{-}105 \mu\text{g}$ per 10^6 hepatocytes per day) as per the data obtained through in vitro-to-in vivo extrapolation technique. [59]

We also evaluated the synthesis of urea as a measure to determine the function of hepatocytes. The synthesis of urea is a hepatocyte specific function that occurs in vivo due to the oxidation of amino acids or ammonia. [60] The total urea produced from the tricultured liver acinus model cultured in static or perfused condition increased significantly ($p \leq 0.001$) on day 5, 10 and 15 in comparison to day 1 (**Figure 4Dv**). Interestingly, the total urea content in the perfused tricultured model on day 5 ($480.56 \pm 37.78 \mu\text{g}$), day 10 ($900.6 \pm 57.95 \mu\text{g}$) and day 15 ($1380.40 \pm 65.74 \mu\text{g}$) was significantly higher (atleast $p \leq 0.05$) than the total urea content in static tricultured model on day 5 ($270.52 \pm 35.18 \mu\text{g}$), day 10 ($598.89 \pm 56.56 \mu\text{g}$) and day 15 ($825.16 \pm 71.97 \mu\text{g}$) respectively. The similar trend of significant increment ($p \leq 0.001$) of DNA normalized urea content in both static and perfusion model were observed on day 5, 10 and 15 in comparison to day 1 (**Figure 4Dvi**). Additionally, the DNA normalized urea content in the perfusion triculture model was also found to be significantly higher than the static triculture model on day 5 ($p \leq 0.05$), day 10 ($p \leq 0.05$) and day 15 ($p \leq 0.001$). Overall, the urea synthesis levels observed in the perfused HPLAM on day 10 and day 15 was also similar to the urea synthesis levels observed in human liver in vivo condition ($\sim 56\text{-}159 \mu\text{g}$ per 10^6 hepatocytes per day) [61]. The synthesis of both urea and albumin by the tricultured model in both the static

and perfusion condition increased in a time-dependent manner, supporting the fact that the hepatocyte functionality in our model was maintained for atleast 15 days.

To further evaluate the physiological relevance of our tricultured HPLAM platform, the drug metabolizing capacity of the liver model, i.e CYP activity and the LDH activity was characterized over 15 days of culture period (**Figure 4Dvii and viii**). We measured the CYP activity of the model cultured for 15 days under static or perfused conditions. The studies revealed that the CYP activity in the static and perfused model portrayed an significant increase ($p \leq 0.05$) on day 5, day 10 and day 15 in comparison to day 1. Further, the perfused liver model portrayed significantly enhanced (atleast $p \leq 0.05$) levels of CYP activity (expressed as mU/mg of total intracellular protein) on day 5 (0.24 ± 0.03 mU/mg), day 10 (0.36 ± 0.04 mU/mg) and day 15 (0.43 ± 0.06 mU/mg) in comparison to day 5 (0.13 ± 0.02 mU/mg), day 10 (0.23 ± 0.03 mU/mg) and day 15 (0.29 ± 0.05 mU/mg) of the static liver model, respectively. Overall the studies revealed that the CYP activity measured on day 10 and day 15 in perfused liver model were comparable to the activity exhibited by freshly isolated hepatocytes, which is currently considered as the gold standard model by pharmaceutical researchers. [59]

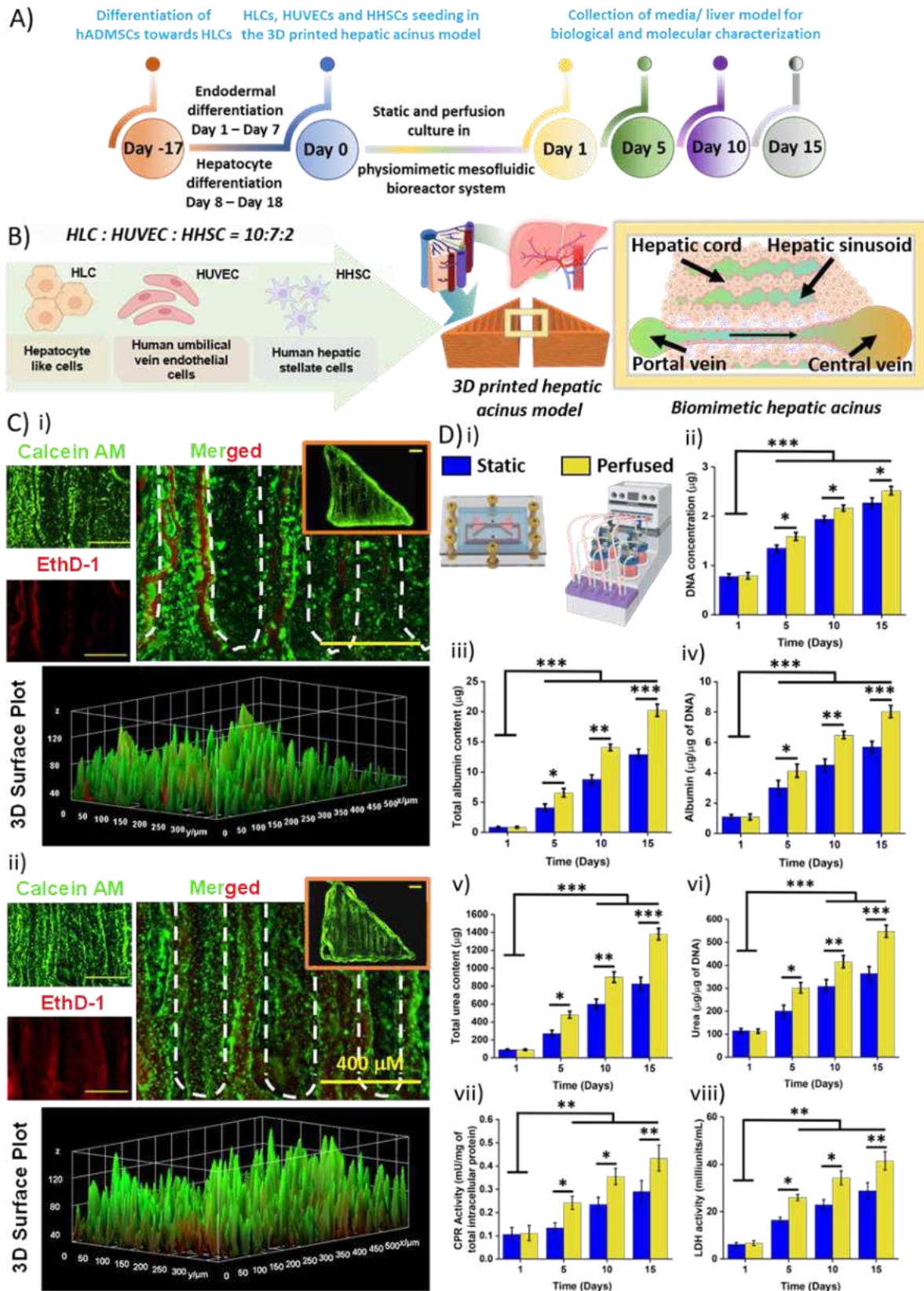


Figure 4: Viability assessment and functional validation of the matured human physiommimetic liver acinus model cultured in static or perfused condition. A) Schematic illustration of the timeline for the assessment of cellular viability, distribution, proliferation

*and functionality of the liver acinus model; **B**) Schematic illustration of the cell seeding ratio of the parenchymal and non-parenchymal cells to emulate the physiologically relevant cellular combination of the native liver acinus **C**) Live/Dead images and 3D surface plots of the HLC/HUVEC/HHSC laden matured liver acinus model cultured in (i) static or (ii) perfused condition for over two weeks. Scale bar: 200 μ m **D**) (i) Illustration representing the static and perfusion condition; Functional assessment of the HLC/HUVEC/HHSC laden liver acinus model cultured in static or perfused condition for over two weeks for (ii) assessment of cellular proliferation and biochemical estimation of (iii) total albumin content, (iv) albumin per μ g of DNA, (v) total urea content, (vi) urea per μ g of DNA, (vii) CYP activity, and (viii) LDH activity; Data is expressed as Mean \pm S.D. ($n = 4$); where statistically significant difference is represented by $*p \leq 0.05$, $**p \leq 0.01$ and $***p \leq 0.001$;*

The intracellular LDH activity of the HPLAM followed a similar trend. The perfused and the static liver acinus model portrayed a significant increase ($p \leq 0.05$) on day 5, day 10 and day 15 in comparison to day 1. However, the perfused liver model portrayed significantly enhanced (at least $p \leq 0.05$) levels of intracellular LDH activity on day 5 (26.04 ± 1.33 milliunits/mL), day 10 (34.31 ± 2.93 milliunits/mL) and day 15 (41.5 ± 3.88 milliunits/mL) in comparison to day 5 (16.36 ± 1.26 milliunits/mL), day 10 (22.86 ± 2.27 milliunits/mL) and day 15 (28.78 ± 03.43 milliunits/mL) of the static liver model, respectively.

The enhanced LDH and CYP activity in the perfused tricultured model may be attributed to the fact that the parenchymal cells are exposed to the paracrine signalling from the non-parenchymal cells as well as other signals generated due to cell-cell and cell-matrix interactions, which altogether help to mimic the cellular events required for tissue maturation and long-term in vitro functionality. Moreover, the complex microarchitecture and cellular interactions in a liver model also assist in maintaining the long term viability and functionality of the hepatocytes as well as the relevant supporting cells. [62] Overall the perfusion-based culture system generated a more physiologically relevant matured liver acinus model with enhanced in vivo like functionality by recapitulating the physiological effects of circulation and shear-stress based enhancement of hepatocytes and non-parenchymal cells physiology, overcoming the diffusion limit by facilitating adequate nutrition and oxygen to all the cells, enabling the accumulation of secreted factors and metabolites and promoting cell viability, proliferation, cell-cell interaction, and cell-matrix interaction. Therefore, our developed tricultured HPLAM platform in the perfusion condition was able to demonstrate and maintain physiologically relevant levels of albumin and urea synthesis, CYP activity and LDH activity following 10 days of maturation. Overall, the data corroborate the robustness of our HPLAM platform for the prediction of diverse phenotypes of drug induced liver toxicity.

5.5 Tricultured HPLAM Platform Promotes Liver-Specific Physiological Genes and Biomarkers Expression Validating Enhanced Model Maturation

Although the cellular viability, proliferation and hepatocyte specific functionality of the triculture liver acinus model was encouraging to a greater extent, it was also important to explore the maturation level based on the liver specific gene and biomarker expression. The gene expression profile of parenchymal (HLC) specific synthetic gene (ALB), phase I and II drug metabolizing genes (CYP2E1 and CYP1A2), other hepatocyte specific genes (CK-19 and HNF4 α); and non-parenchymal HUVEC and HHSC genes (cluster of differentiation 31, CD31; Von Willebrand Factor, vWF; desmin, DES) were determined in liver acinus model cultured under both static and dynamic culture conditions. The two major cytochrome P450 (CYP) isoforms (CYP1A2 and CYP2E1) were assessed as they are categorized under phase I and II metabolizing genes which play an important role in metabolism of many clinically used drugs [63]. Expression of these CYP isoforms have also been reported to majorly affect drug pharmacokinetics and has clinical relevance for drugs having narrow therapeutic window [64]. Following 15 days of maturation, the expression level of the HLCs specific synthetic gene, ALB, increased significantly ($p \leq 0.001$) by about 9.4-fold in the static cultured liver acinus model and by about 11.7-fold in the perfusion cultured liver acinus model (**Figure 5Ai**). Similarly, the expression level of the HLC specific drug metabolizing and hepatocyte specific genes, CYP2E1, CYP1A2 and CK-19 were also significantly upregulated (atleast $p \leq 0.01$) following 15 days of maturation by about 9.2-fold, 8-fold and 10.2-fold respectively in the static cultured liver acinus model and by about 12-fold, 9.9-fold and 13.9-fold respectively in the perfusion cultured liver acinus model (**Figure 5Aii, iii and iv**). Additionally, the expression level of hepatic progenitor HNF4 α was also maintained at significantly high levels over the period of 15 days (**Figure 5Av**). The expression level of the HUVEC and HHSC specific genes, vWF, CD31, and DES were also significantly upregulated (atleast $p \leq 0.01$) over 15 days of maturation by about 11-fold, 9-fold, and 8-fold respectively in the static cultured liver acinus model and by about 14.5-fold, 11.2-fold, and 10.3-fold respectively in the perfusion cultured liver acinus model (**Figure 5Avi, vii and viii**). Moreover, the expression of the specific HLC genes: ALB, CK-19, CYP2E1 and CYP1A2 in the perfused liver model was significant enhanced (atleast $p \leq 0.05$) on day 5, day 10 and day 15 in comparison to the static liver model respectively (**Figure 5A**). Similarly, the expression of the non-parenchymal cells specific

genes: vWF, CD31 and DES were also significantly enhanced (atleast $p \leq 0.05$) on day 5 (except CD31), day 10 and day 15 in the perfused liver model in comparison to the static liver model respectively (**Figure 5A**). A heat map profile also revealed the significant upregulation of the expressed genes associated with hepatic homeostasis, xenobiotic metabolic process, response to lipopolysaccharide and phase I and II drug metabolic process in the perfused liver acinus model over a period of 15 days, supporting that the triculture of the HLCs with HUVECs and HHSCs under dynamic platform provides a more favourable platform for model maturation (**Figure 5B**). Together, these findings revealed a relatively more matured gene expression profile of the perfused triculture liver model in comparison to the static model.

Encouraged by the expression of the HLC, HUVEC and HHSC specific genes, we also investigated the protein expression and co-localization of the key HLC, HUVEC and HHSC markers involved in maintaining hepatic homeostasis and liver drug metabolism in the both the static and perfused liver acinus model following two weeks of culture. From the analysis of the surface plot and immunofluorescence images, the perfused liver acinus model demonstrated higher expression of the HLC specific marker ALB (green fluorescence) and HHSC specific marker DES (red fluorescence) in comparison to the static liver acinus model (**Figure 6Ai and 5Di**). Analysis of the immunofluorescence images showed the linear alignment of the clustered HLCs and the distinctly aligned HHSCs along the filament. Similarly, the perfused liver acinus model demonstrated higher expression of the HLC specific marker ALB (green fluorescence) and HUVEC specific marker vWF (red fluorescence) in comparison to the static liver acinus model (**Figure 6Aii and 5Dii**). The immunofluorescence image analysis showed more prominent vascular networks in the perfused model in comparison to the static model. Moreover, the perfused model also demonstrated enhanced expression of HLC specific phase I metabolism protein CYP2E1, HUVEC specific cell adhesion protein CD31 and HHSC specific intermediate filament protein DES in comparison to the static model (**Figure 6Aiii-iv and 5Diii-iv**). Overall the analysis of the surface plot and immunofluorescence images suggested the alignment and colonization of the cells along the filaments of the 3D printed scaffolds with distinct clustering of the HLCs and formation of vascular network by the HUVECs.

In line with the changes in the secretome levels observed, the gene expression studies and immunofluorescence staining also confirmed the enhanced expression of the hepatocyte, HUVEC and HHSC specific genes and markers in the perfused tricultured liver acinus model in comparison to the static model. Previous studies have also demonstrated the significance of

co-culturing parenchymal cells with non-parenchymal cells in a dynamic flow condition for enhanced multicellular interaction, viability and prolonged maintenance of liver specific synthetic and metabolic functions compared to static 3D culture or 2D monoculture [20, 65]. Moreover, the non-parenchymal cells play a vital role in the maturation of the liver model through complex regulatory pathways induced through the synthesis, secretion of cytokines and growth factors. In addition, the paracrine interaction between the parenchymal and the non-parenchymal cells also play a crucial role in the process of liver model maturation in vitro [66]. Thus, the perfused tricultured liver acinus model acted as an optimal analog of the vascularized liver acinus-like microenvironment suitable for evaluating diverse phenotypes of drug toxicity.

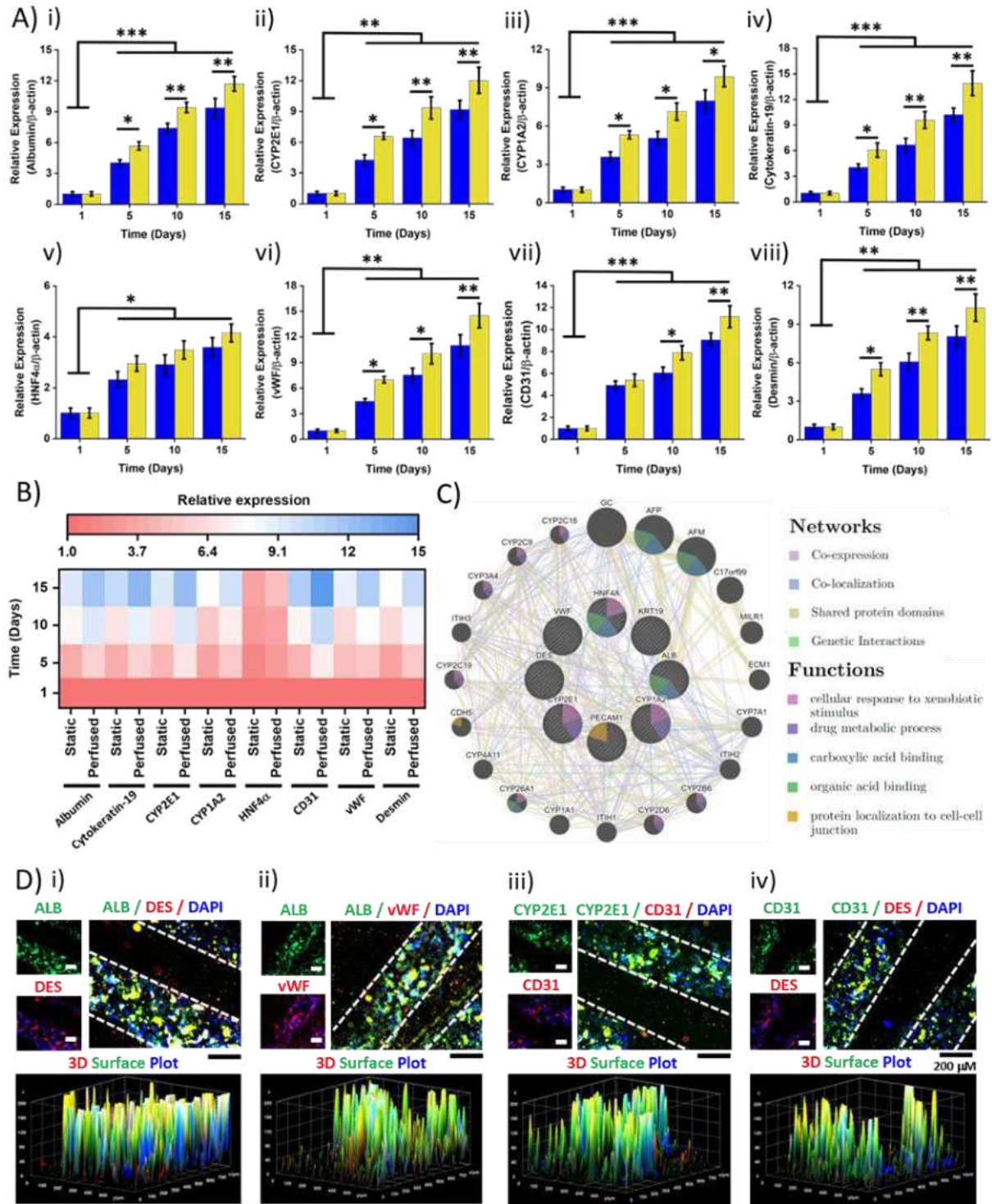


Figure 5: Functional assessment of the matured human physiometric liver acinus model cultured in static or perfused condition; (A) Gene expression profile of parenchymal (HLC) specific synthetic gene (ALB), phase I and II drug metabolizing genes (CYP2E1 and CYP1A2), other hepatocyte specific genes (CK-19 and HNF4 α) and non-parenchymal HUVEC and HHSC specific genes (CD31, vWF, and DES). Data is expressed as Mean \pm S.D. ($n = 4$); where statistically significant difference is represented by $*p \leq 0.05$, $**p \leq 0.01$ and $***p \leq 0.001$; (B) Real time gene expression heat-map profile of the expressed genes pertaining to the maturation of the tricutured liver acinus model; (C) Analysis of the gene-gene interactions

occurring between the expressed genes and other interactive genes, based on the data obtained from the GeneMANIA database; **(D)** Immunohistological analysis and 3D surface plot of the HLC/HUVEC/HHSC laden liver acinus model cultured under static condition for over two weeks for (i) albumin (green), DES (red), and nucleus (blue), (ii) albumin (green), vWF (red), and nucleus (blue), (iii) CYP2E1 (green), CD31 (red), and nucleus (blue) and (iv) CD31 (green), DES (red), and nucleus (blue) to visualize the distribution and alignment of the parenchymal cells (HLC) and non-parenchymal cells (HUVEC/HHSC) along the filaments of the 3D printed scaffolds and determine the maturation of the model. Scale bar: 200 μ m;

5.6 Gene and Protein Interaction Networks Indicated Both Functional and Physical Associations Among the Expressed and Interactive Genes and Proteins

Potential associations between the expressed genes and proteins in our study with other interactive genes and proteins that are involved in the maturation and functionality of the model were evaluated using gene and protein interaction network analysis. In this study, the GeneMANIA server was used to acquire and determine data related to the possible gene-gene physical interaction, co-expression, co-localization, gene enrichment analysis and pathways functionally associated with the differentially expressed genes (ALB, CK-19, CYP2E1, CYP1A2, HNF4 α , CD31, vWF and DES) analysed using quantitative RT-PCR. The protein interaction network of 20 genes interactive with the expressed genes were identified using the database (**Table S2**). The analysis of the 28 genes showed that the genes were mainly involved in cellular responses to xenobiotic stimulus, drug metabolic process, carboxylic and organic acid binding, long chain fatty acid metabolic processes, oxidoreductase activities, protein localization to cell-cell junctions and in alcohol as well as vitamin metabolic processes (**Figure 5C**). Most of the genes in the network are from the CYP family namely CYP2E1, CYP1A2, CYP4A11, CYP7A1, CYP2B6, CYP2D6, CYP1A1, CYP26A1, CYP4A11, CYP2C19, CYP3A4, CYP2C9 and CYP2C18 which are mainly categorized under the functions: drug metabolic process, steroid metabolic process, cellular response to xenobiotic stimulus and carboxylic acid biosynthesis. The other parenchymal and non-parenchymal specific genes such as ALB, AFP, GC, HNF4A, PECAM were categorized under the functions: cellular response to xenobiotic stimulus, carboxylic acid binding, organic acid binding, vitamin metabolic process, protein localization to cell-cell junction and steroid metabolic process. Moreover, the other interactive genes namely, CYP1A2, CYP2E1, CYP2B6, CYP2D6, CYP7A1, GC, AFM, C17orf99, ITIH1, PECAM1, MILR1, CDH5, CYP3A4, CYP2C18 and CYP2C9 were categorized under fatty acid biosynthesis and metabolic process, carboxylic acid binding and biosynthetic process, oxidoreductase activity, cell-cell adhesion and transmembrane signalling

receptor activity. The network analysis also showed that majority of the genes showed co-expression, while the other types of interactions included co-localization, shared protein domain and genetic interactions.

The STRING database was used to illuminate on the protein-protein interactions occurring between the proteins by the expressed genes and other associated proteins, assessed based on combined scores representing confidence (0-1). The protein-protein interactions showed 13 nodes (proteins from genes) and 28 edges (protein-protein associations) that are predicted to play a significant role in the maturation of the liver model by promoting cell-cell interaction, cell-matrix adhesion, ECM production, metabolism of proteins and lipids as well as in evaluating drug induced hepatotoxicity through expression of proteins associated with the pathways involving drug absorption, distribution, metabolism and excretion (**Table S3 and S4**). From the data analysis, the closely predicted functional partners were Integrin alpha-IIb light chain (ITGA2B), form 1, P-selectin (SELP), Vascular endothelial growth factor receptor 2 (KDR), Lymphoid enhancer-binding factor 1 (LEF1) and Alpha-2-HS-glycoprotein chain A (AHSG). The functional enrichment of the network involving the expressed and predicted functional partners showed close interactions based on co-expression, curated database, phylogenetic co-occurrence, experimental data, textmining, co-expression and protein homology (**Figure 6B**). Based on the functional enrichment network, tissue specific protein expressions involved HNF4 α , KRT19, CYP1A2, CYP2E1, ALB, AHSG, PECAM, vWF, DES and KDR, reactome pathways corresponding to the expressed and functional partner proteins involved CYP1A2, CYP2E1 and ALB, and KEGG pathways corresponding to the expressed and functional partner proteins involved ITGA2B, vWF, KDR, CYP1A2 and CYP2E1.

Overall the gene and protein interaction networks indicated both functional and physical associations among the expressed and interactive genes, which would play a vital role in the maturation of the liver model through complex regulatory pathways and provide a suitable microenvironment for evaluating diverse phenotypes of drug toxicity.

5.7. Improved sensitivity of the HPLAM Platform for detection of diverse phenotypes of hepatotoxicity

DILI is the major reason for phase IIb/III clinical trial drug failure, ‘black box warnings’ and the withdrawal of marketed drugs (phase IV). In particular, the termination of the drug development projects and withdrawal of the marketed drugs are mainly ascribed to the genetic

and physiological differences between animals and humans as well as the existence of over simplified *in vitro* experimental models. These late-stage failure lead to a loss of substantial time, money and effort invested in the drug developmental pipeline, making the drug development process inefficient. [3, 10] Moreover, the pre-clinical animal models and the simple static human *in vitro* models fail to detect idiosyncratic DILI. Therefore, one of the promising solutions has been the development of complex human physiomic models to recapitulate the liver acinus or sinusoid structure and function to improve their application for drug screening or drug toxicity evaluation. [10, 56] In line with this evolution, our human physiomic liver model was developed by incorporating transdisciplinary technologies including microfluidic devices, 3D printing, engineered matrix material and patient derived mesenchymal stem cell derived hepatocytes, endothelial cells and hepatic stellate cells. Non-parenchymal cells along with parenchymal cells also play a potential role in drug induced hepatotoxicity as reported previously. [59] Therefore, the inclusion of non-parenchymal cells along with parenchymal cells in our liver model would allow paracrine signalling among the multiple cells for the identification of diverse phenotype of drug toxicities targeting both types of cells. As previously mentioned, our matured liver model exhibited characteristics and functions of clinical relevance to provide mechanistic knowledge required for determining drug induced liver injury. To determine the sensitivity and specificity of the physiomic liver acinus model as platform to evaluate diverse phenotype of DILI of human relevance, we used a set of 05 drugs across the different classifications observed in DILIrank, i.e. “No-DILI concern”, “Less-DILI concern” and “Most-DILI concern”. [16] Mostly, these drugs were chosen due to kinetic stability, portrayed specific toxicity in hepatocytes, has pre-reported effective *in vitro* concentrations and *in vivo* model data, and has high human relevance. Accordingly the drugs were further classified (**Table 2**) as non-hepatotoxicants (Aspirin and dexamethasone), idiosyncratic-hepatotoxicants (Trovafloracin mesylate) and hepatotoxicants (Acetaminophen and Troglitazone) as per our previous study. [7]

5.7.1 Identifying effect of non-hepatotoxicants on the HPLAM

Following maturation for 10 days, the models were exposed to the non-hepatotoxicant drugs, aspirin and dexamethasone, for 24 h and 72 h in static or perfusion condition (**Figure 6C**).

The data from the 24h and 72h aspirin drug treatment experiment indicated that both the static and dynamic model exhibited >95% cellular viability and maintained LDH activity at 5.53 μM (C_{max}) and 552.6 μM ($100 \times C_{\text{max}}$) (**Figure 6Di–iii and v–vii**).

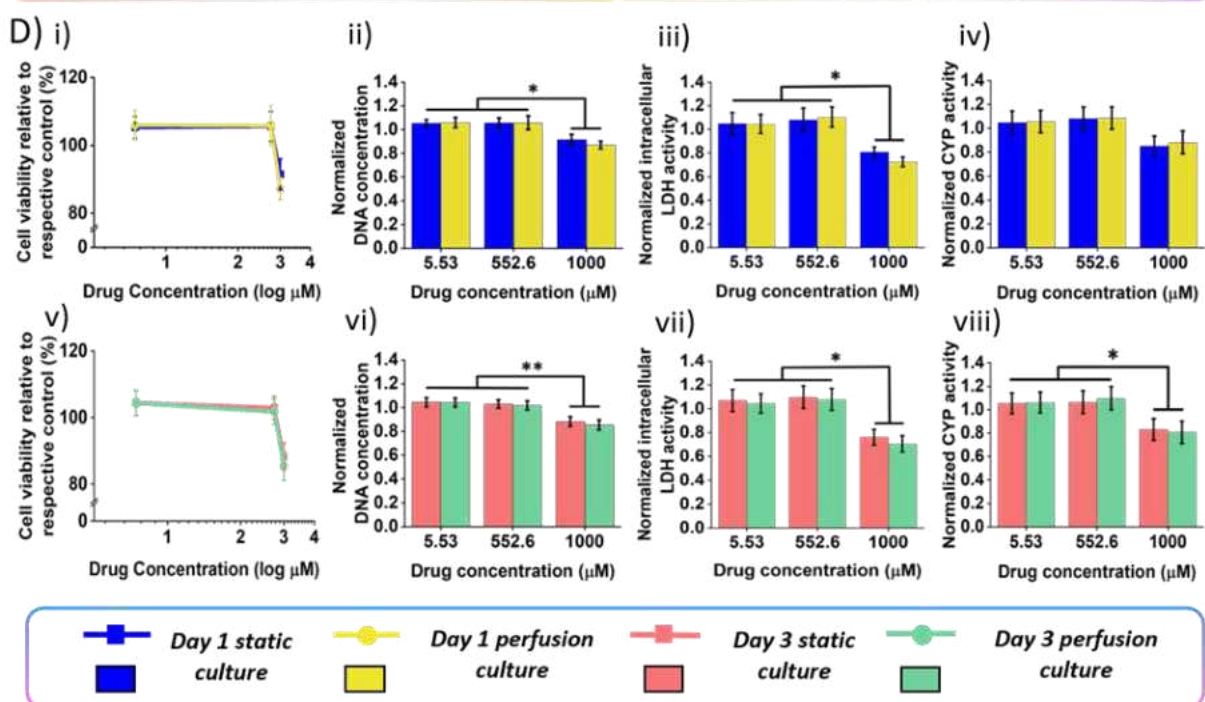
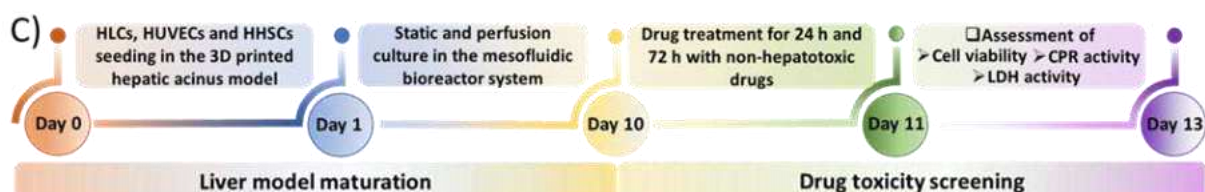
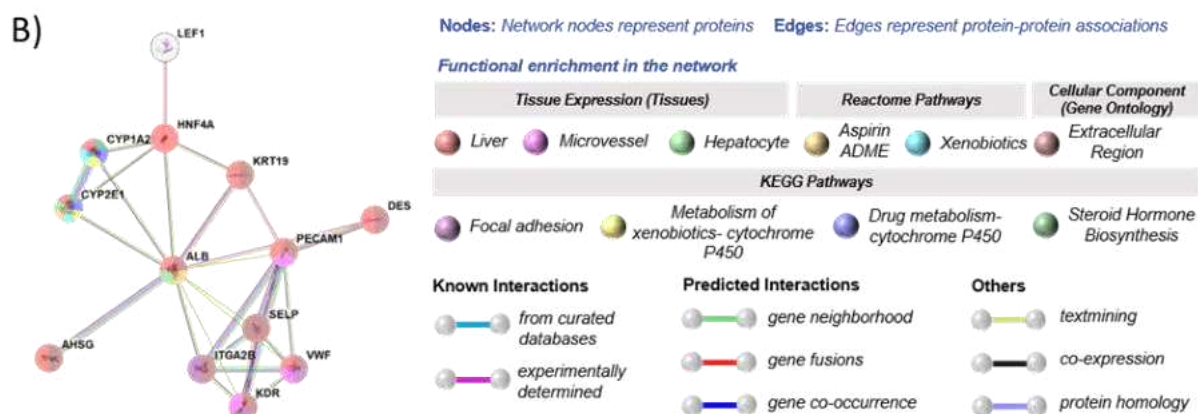
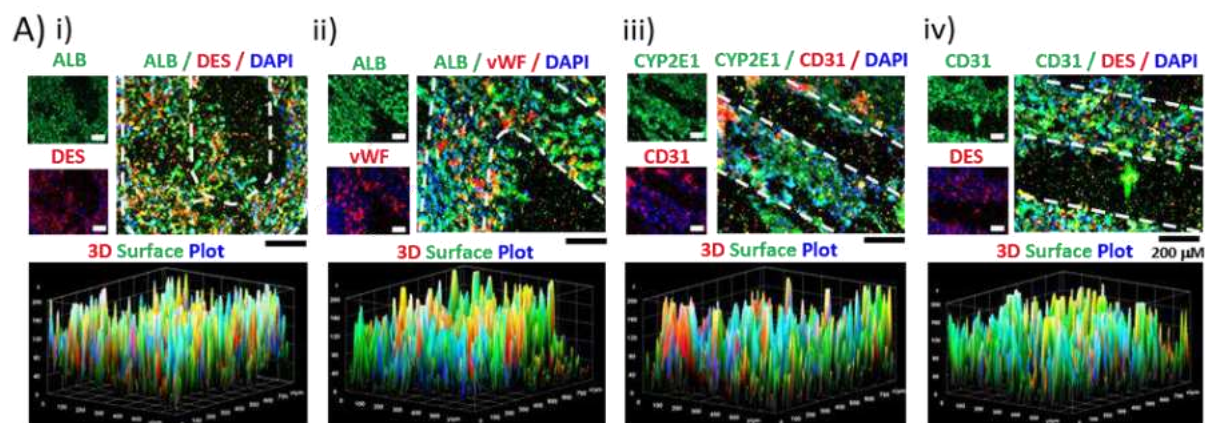


Figure 6: Functional assessment and drug toxicity prediction in the matured tricultured human physiometric liver acinus model (A) Immunohistological analysis and 3D surface plot of the HLC/HUVEC/HHSC laden liver acinus model cultured under perfusion condition for over two weeks for (i) albumin (green), DES (red), and nucleus (blue), (ii) albumin (green), vWF (red), and nucleus (blue), (iii) CYP2E1 (green), CD31 (red), and nucleus (blue) and (iv) CD31 (green), DES (red), and nucleus (blue) to visualize the distribution, alignment and colonization of the parenchymal cells (HLC) and non-parenchymal cells (HUVEC/HHSC) along the filaments of the 3D printed scaffolds with distinct clustering of the HLCs and formation of vascular network by the HUVECs and determine the maturation of the model. Scale bar: 200 μ m; (B) Analysis of the protein-protein interactions occurring between the proteins of the expressed genes and other associated proteins, based on the data obtained from the STRING database; (C) Schematic illustration of the timeline of the maturation followed by exposure of the liver acinus model to non-hepatotoxic drug; (D) Exposure of the tricultured liver acinus model to non-hepatotoxic drug aspirin in static and perfused condition for 24 h followed by estimation of (i) Percentage of cell viability, (ii) DNA content, (iii) intracellular LDH activity and (iv) CYP activity and for 72 h followed by estimation of (v) Percentage of cell viability, (vi) DNA content, (vii) intracellular LDH activity and (viii) CYP activity. Data is expressed as Mean \pm S.D. ($n = 4$); where statistically significant difference is represented by $*p \leq 0.05$, $**p \leq 0.01$ and $***p \leq 0.001$.

While in case of aspirin concentration 1000 μ M (above $100 \times C_{\max}$), significant cytotoxicity was observed with significantly ($p \leq 0.05$) reduced DNA concentration and LDH activity in both static and perfusion condition. In case of 24h aspirin treatment the drug metabolizing functions were found to be similar across the various drug concentrations as well as between the groups (**Figure 6Div**). However, in case of the 72h aspirin treatment condition, a significant reduction ($p \leq 0.05$) was observed in the CYP activity of 1000 μ M concentration group in comparison to the 5.53 μ M and 552.6 μ M concentrations (**Figure 6Dviii**). As per the observations from previous clinical DILI reports and U.S. Food and Drug Administration (FDA), a similar trend in the hepatotoxicity of higher doses of aspirin (above $100 \times C_{\max}$) was observed in our physiometric liver acinus model. [67-70]

Dexamethasone administration at the selected concentrations for 24h and 72h demonstrated no effect on the cellular viability and drug metabolizing functions in both static and perfusion conditions (**Figure 7A**). No significant differences were observed in DNA concentration, intracellular LDH activity and CYP activity in the model (**Figure 7B**). In case of dexamethasone, the absence of hepatotoxicity in the tested range of concentrations, indicate that the physiometric liver model mimics the clinical response, thus proving its potential for drug screening evaluation of in vivo relevance. [39, 71, 72]

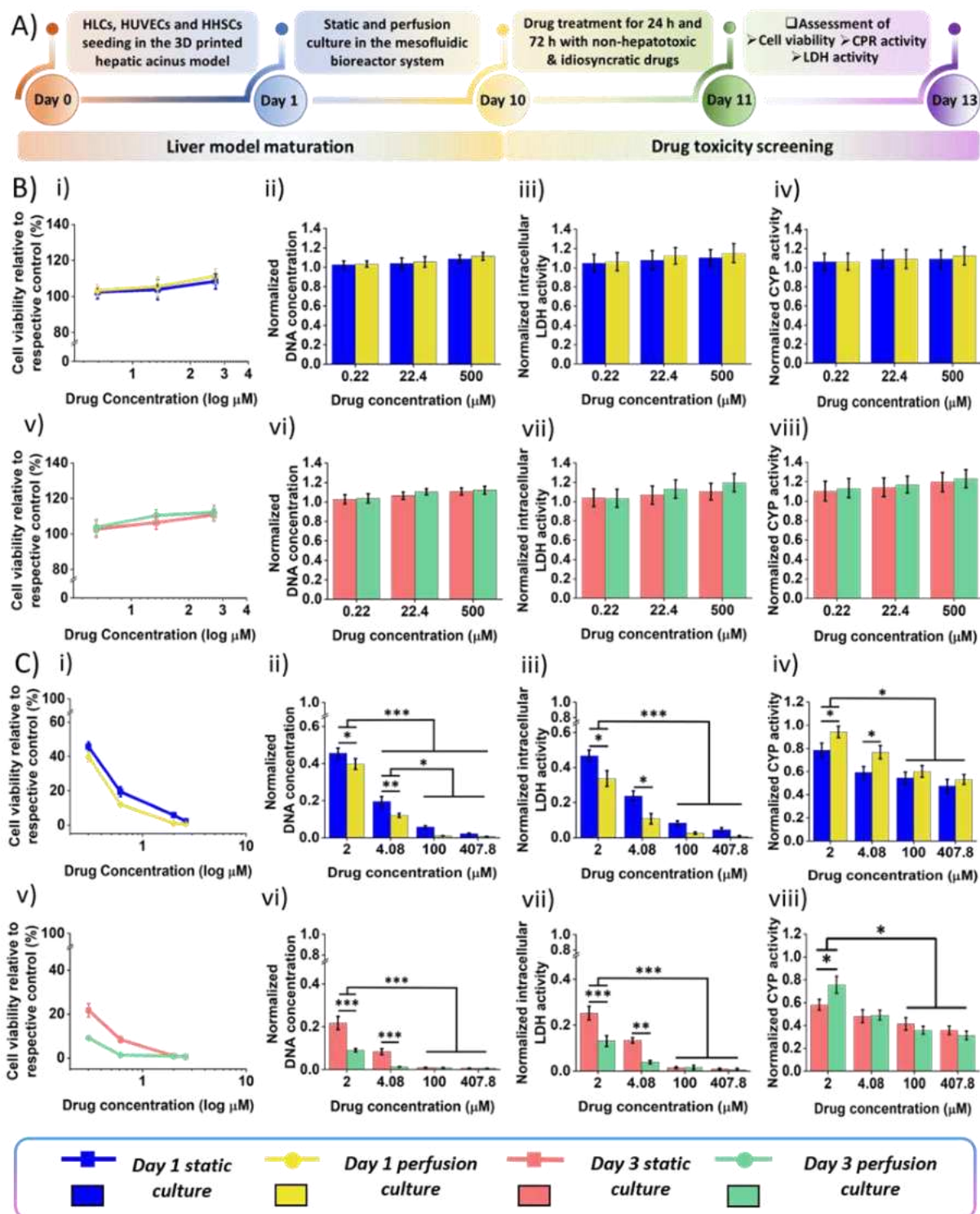


Figure 7: Drug toxicity prediction in the matured tricultured human physiometric liver acinus model exposed to non-hepatotoxic and idiosyncratic drugs in static or perfused condition for 24 h and 72 h; (A) Schematic illustration of the timeline of the maturation followed by exposure of the liver acinus model to non-hepatotoxic and idiosyncratic drugs;

*Exposure of the tricultured liver acinus model to non-hepatotoxic drug (B) dexamethasone and idiosyncratic drug (C) trovafloxacin mesylate in static and perfused condition for 24 h followed by estimation of (i) Percentage of cell viability, (ii) DNA content, (iii) intracellular LDH activity and (iv) CYP activity and for 72 h followed by estimation of (v) Percentage of cell viability, (vi) DNA content, (vii) intracellular LDH activity and (viii) CYP activity. Data is expressed as Mean \pm S.D. ($n = 4$); where statistically significant difference is represented by $*p \leq 0.05$, $**p \leq 0.01$ and $***p \leq 0.001$.*

5.7.2 Identifying risk for idiosyncratic DILI using the HPLAM platform

One of the most difficult type of hepatotoxicity to predict in the clinical setting is the idiosyncratic DILI response. To explore the sensitivity of our physiometric liver acinus model for this type of responses, we tested trovafloxacin mesylate, a broad-spectrum fluoroquinolone, that was discontinued from the market after severe adverse hepatic events and acute liver failure in human patients in the year 1999. [73] Leveraging the physiometric model, we investigated the toxicity of trovafloxacin mesylate at concentrations similar to the therapeutic doses in humans, C_{max} , $100 \times C_{max}$, and above $100 \times C_{max}$ concentrations (**Figure 7A**). The liver acinus model showed a dose- and time- dependent toxicity with a significant decrease in the cellular viability with the increase in the drug concentration. Following 24h of trovafloxacin treatment, the static and perfused liver acinus models showed hepatotoxic effect with an EC_{50} of 1.1 μM and an EC_{50} of 0.85 μM respectively, as extrapolated from the percentage of cell viability and dose response curve (**Figure 7Ci**). Similarly, following 72h of treatment with trovafloxacin, the static and perfused liver acinus models showed hepatotoxic effect with an EC_{50} of 0.95 μM and EC_{50} of 0.65 μM respectively (**Figure 7Cv**). After 24h and 72h of trovafloxacin treatment, a significant reduction in the cellular viability, LDH activity and CYP activity was observed in both the static and perfused conditions at 4.08 μM , 100 μM and 407.8 μM as compared to 2 μM trovafloxacin concentration (**Figure 7Cii-iv and vi-viii**). Pertinently, a significantly relevant reduction in cell viability was observed in the perfused group treated for 24h with 2 μM ($p \leq 0.05$) and 4.08 μM ($p \leq 0.01$) of trovafloxacin in comparison to the static group. While a more physiologically relevant reduction in cell viability was observed in the perfused group treated for 72h with 2 μM ($p \leq 0.001$) and 4.08 μM ($p \leq 0.001$) of trovafloxacin in comparison to the static group.

In case of LDH activity also, a significant reduction (atleast $p \leq 0.05$) is noted among the static and perfused group treated for 24h or 72h with 2 μM and 4.08 μM of trovafloxacin. To further evaluate the physiological relevance of the models, the drug metabolizing capacity was also characterized. The CYP activity was significantly increased in the perfused group compared to the static group at a drug concentration of 2 μM ($p \leq 0.05$) of trovafloxacin when treated for 24h and 72h and 4.08 μM ($p \leq 0.05$) of trovafloxacin when treated for 72h. Strikingly, the CYP activity among the static and perfusion group showed negligible difference at Trovafloxacin concentrations 4.08 μM , 100 μM and 407.8 μM of trovafloxacin treatment for 24h or 72 h even through the DNA concentration had significantly reduced. Thus, the perfused model demonstrated a more human specific response following exposure of the drug with respect to reduced cellular viability, intracellular LDH activity and CYP activity at C_{max} , $100 \times C_{\text{max}}$, and above $100 \times C_{\text{max}}$ concentrations. [74] This exemplifies the advantage of our perfusion-based liver acinus model for assessing the pathophysiological consequences of idiosyncratic DILI.

5.7.3 Identifying risk for intrinsic DILI using the HPLAM platform

Further to assess the ability of the liver acinus model for intrinsic DILI evaluation in human, the general analgesic acetaminophen as well as an antidiabetic and anti-inflammatory drug troglitazone were tested for hepatotoxicity (**Figure 8A**). Both the drugs are known to cause whole organ failure or even death when overdosed [75-78]. In case of acetaminophen a ‘Boxed Warning’ highlighting severe liver injury and allergic reactions have been enforced by FDA, while troglitazone was withdrawn from the market by the FDA in the year 2000 [79, 80]. Herein, the microengineered liver acinus model was administered with acetaminophen with a range of concentration in-between C_{max} , and $100 \times C_{\text{max}}$. Both the static and the perfused liver models treated with acetaminophen experienced a dose- and time- dependent toxicity with a significant decrease in the DNA concentration and LDH activity with the increase in the drug concentrations. Following 24h of treatment, the static and perfused liver acinus models showed hepatotoxic effect with an EC_{50} of 3503.26 μM and an EC_{50} of 2965.15 μM respectively, as extrapolated from the percentage of cell viability and dose response curve (**Figure 8Bi**). Similarly, following 72h of treatment with trovafloxacin, the static and perfused liver acinus models showed hepatotoxic effect with an EC_{50} of 3014.86 μM and EC_{50} of 2417.96 μM respectively (**Figure 8Bv**). In addition, following 24h and 72h of acetaminophen treatment, a significant reduction in the cellular viability, LDH activity and CYP activity was observed in

both the static and perfusion conditions at 5000 μM , 10000 μM and 13900 μM as compared to 139 μM of acetaminophen concentration (**Figure 8Bii-iv and vi-viii**). Intriguingly, a significantly relevant reduction in cell viability was observed in the dynamic group treated for 24h with 5000 μM ($p \leq 0.01$) and 10000 μM ($p \leq 0.01$) acetaminophen in comparison to the static group. While a more physiologically relevant reduction in cell viability was observed in the dynamic group treated for 72h with 5000 μM ($p \leq 0.01$) acetaminophen in comparison to the static group.

In case of LDH activity also, a significant reduction ($p \leq 0.05$) is noted among the static and perfused groups treated with 5000 μM and 10000 μM of acetaminophen for 24 h and with 5000 μM of acetaminophen for 72h. In addition, the physiological relevance of the models was evaluated by determining the drug metabolizing capacity. The CYP activity was significantly increased in the perfusion group compared to the static group at a drug concentration of 139 μM (atleast $p \leq 0.05$) and 5000 μM ($p \leq 0.05$) of acetaminophen treatment for 24h and 72h. The CYP activity in both the static and perfused group significantly reduced (atleast $p \leq 0.05$) at 10000 μM and 13900 μM in comparison to 139 μM acetaminophen treatment for 24h or 72 h, suggesting a more in vivo mimicking response to hepatotoxic drugs.

In case of troglitazone as well, a similar hepatotoxic response was noted for the range of concentrations used in-between C_{max} , and $100 \times C_{\text{max}}$. The static and the perfused liver models treated with troglitazone experienced a similar dose- and time- dependent toxicity with a significant decrease in the DNA concentration and LDH activity with the increase in the drug concentrations. Following 24h of troglitazone treatment, the static and perfused liver acinus models showed hepatotoxic effect with an EC_{50} of 51.12 μM and an EC_{50} of 35.06 μM respectively, as extrapolated from the percentage of cell viability and dose response curve (**Figure 8Ci**). Likewise, following 72h of treatment with trovafloxacin, the static and perfused liver acinus models showed hepatotoxic effect with an EC_{50} of 39.86 μM and EC_{50} of 24.96 μM respectively (**Figure 8Cv**). Subsequently, after 24h and 72h of troglitazone treatment, a significant reduction in the cellular viability, LDH activity and CYP activity was observed in both the static and perfused conditions at 50 μM , 100 μM and 638.7 μM as compared to 6.39 μM of troglitazone concentration (**Figure 9Cii-iv and vi-viii**). Moreover, a significantly relevant reduction in cell viability was observed in the dynamic group treated for 24h with 50 μM ($p \leq 0.01$) and 100 μM ($p \leq 0.01$) troglitazone in comparison to the static group. While a

more physiologically relevant reduction in cell viability was observed in the dynamic group treated for 72h with 50 μM ($p \leq 0.001$) 100 μM ($p \leq 0.01$) troglitazone in comparison to the static group.

In case of LDH activity also, a significant reduction (atleast $p \leq 0.05$) is noted among the static and perfused groups treated with 50 μM and 100 μM of troglitazone for 24 h or 72h. In addition, the physiological relevance of the models was evaluated by determining the drug metabolizing capacity. The CYP activity was significantly increased in the perfused group compared to the static group at 6.39 μM ($p \leq 0.05$) and 50 μM ($p \leq 0.05$) of troglitazone when treated for 24h and 72h. Strikingly, the CYP activity in both the static and perfused group significantly reduced at drug concentrations 100 μM and 638.7 μM troglitazone treatment for 24h or 72 h suggesting a more in vivo like response to hepatotoxic drugs.

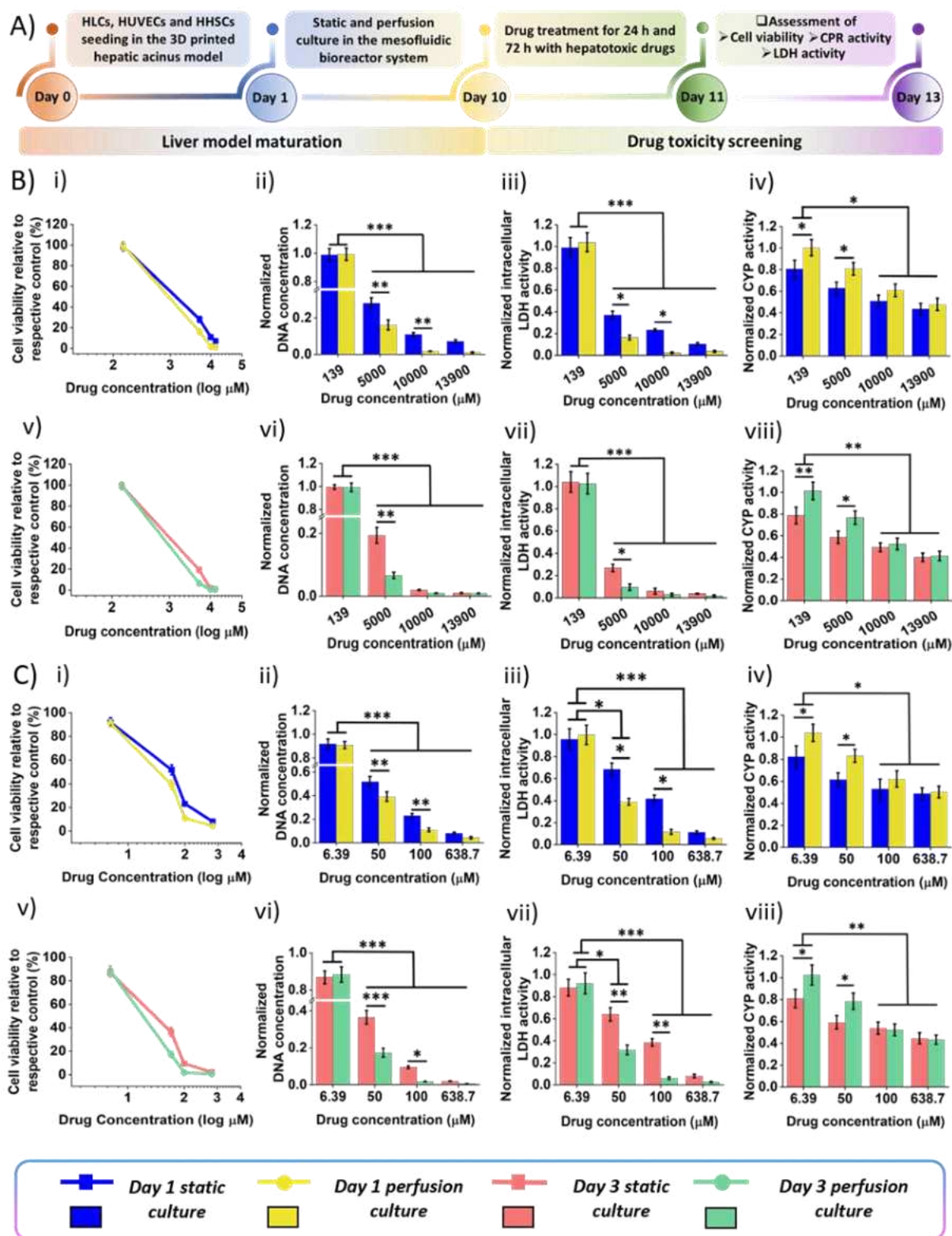


Figure 8: Drug toxicity prediction in the matured tricultured human physiometric liver acinus model exposed to hepatotoxic drugs in static or perfused condition for 24 h and 72 h; (A) Schematic illustration of the timeline of the maturation followed by exposure of the liver acinus model to hepatotoxic drugs; Exposure of the tricultured liver acinus model to hepatotoxic drugs (B) acetaminophen and (C) troglitazone in static and perfused condition for

24 h followed by estimation of (i) Percentage of cell viability, (ii) DNA content, (iii) intracellular LDH activity and (iv) CYP activity and for 72 h followed by estimation of (v) Percentage of cell viability, (vi) DNA content, (vii) intracellular LDH activity and (viii) CYP activity. Data is expressed as Mean \pm S.D. ($n = 4$); where statistically significant difference is represented by $*p \leq 0.05$, $**p \leq 0.01$ and $***p \leq 0.001$.

6. Discussion

As per the previously published reports of in vitro liver models, a gap still exists in determining drug based liver toxicity assessment of human relevance [10, 56]. Currently the “gold standard model” used by the pharmaceutical researchers for hepatotoxicity prediction is 2D monolayer of freshly isolated patient specific hepatocytes. But such 2D models fail to predict hepatotoxicity due to lack of physiologically relevant microenvironment, limited availability, rapid de-differentiation and reduced liver specific functions and morphology with time [7, 56]. To make vital decisions in the drug development process, specific “context of use” are usually defined for in vitro models. Our developed in vitro model mainly focuses in the identification of potential drugs causing human liver toxicity. In our study, the perfusion based physiomimetic liver acinus model in comparison to the static model contributed to a more heightened sensitivity for DILI and enhanced metabolic competence, as evidenced from the substantially low EC_{50} values and higher CYP activity. The reason for the improved sensitivity could be attributed to the biomimetic liver acinus like microphysiological bioreactor platform, maintenance of physiologically relevant fluid flow rates, enhanced hepatocyte functionality including drug metabolizing enzymes, improved paracrine interactions of the injured hepatocytes with the endothelial and stellate cells as well as enhanced culture longevity. In addition, the physiomimetic bioreactor platform also maintained a recirculating continuous flow of media, which ensured that both the parenchymal and non-parenchymal cells were exposed to sufficient amount of the parent drug and its metabolites. Intriguingly, the results from our studies with non-hepatotoxic, hepatotoxic and idiosyncratic drugs portray that the physiomimetic model can be used to study clinically relevant concentration of drugs for assessing human specific sensitivities and also predict diverse mechanism of drug induced liver toxicities that target parenchymal and non-parenchymal cells. Human specific sensitivities to idiosyncratic drug (trovafloxacin mesylate), hepatotoxic drugs (acetaminophen and troglitazone) and even non-hepatotoxic drugs (aspirin and dexamethasone), were confirmed in our perfused physiomimetic liver acinus model through the DNA concentration, LDH activity and CYP activity responses obtained post drug treatment with clinically relevant doses [39, 81,

82]. Particularly the perfused model, showed a strong hepatotoxic effect for both the idiosyncratic and hepatotoxic drugs with EC_{50} significantly lower than $100 \times C_{max}$ at both 24h and 72h treatment.

Interestingly, our model predicted a diverse phenotype of hepatotoxicity with more human specific sensitivity in comparison to the previously reported 3D liver in vitro models [17-21]. Further in comparison to current human liver microphysiological models, Organo-PlateTM (Mimetas) [83] and ExVive (Organovo Holdings Inc.) [19], our model portrayed amplified sensitivity to hepatotoxicants at clinically relevant concentrations. It is noteworthy, that the hepatotoxic effects were evaluated without any addition of inflammatory cytokines or inclusion of Kupffer cells. The advantage of our model was that we could relate the dose-dependent decline in the cellular viability with the drug metabolism capacity of the hepatocytes, which suggests the ability of the model in delineating pathways and mechanisms of DILI. In addition, the maintenance of metabolic competence and functionalities for prolonged durations allows the model to be evaluated for drug toxicity evaluation for longer durations. Based on the evaluation of the diverse type of drugs, cellular toxicities in the model were detected at concentrations similar to the human plasma concentrations associated with DILI, which suggest that the HPLAM can be used for drug induced human risk assessment.

Here in this study, transdisciplinary technologies have been used to develop a physiometric liver acinus model to recapitulate the cellular microenvironment by tuning spatiotemporal parameters like cell-cell and cell-matrix interaction, fluid flow recirculation and shear stresses through physiologically relevant fluid flow rates. Overall the tricultured physiometric liver acinus model acted as metabolically active biofactories and maintained the production of albumin, urea and activities of multiple key drug metabolizing enzymes at in vivo like concentrations for atleast 15 days of culture. To the best of our knowledge, this is the first report that developed a physiometric 3D printed vascularized liver acinus model that not only emulates the native hepatic cord structure with functional sinusoidal microvasculature network but also the physiological flow conditions inside the liver sinusoids for drug toxicity evaluation of human relevance. Our follow-up studies will mainly focus on measuring mechanistic end points and biomarkers for delineating pathways and mechanisms causing drug induced liver injury following repeated drug dosage. In addition, future studies will also be focussed on the inclusion of induced pluripotent stem cells-derived human liver organoids in the developed liver mimetic biomaterial ink for the fabrication of a 3D bioprinted liver acinus model towards

a more predictive patient specific platform that may improve further DILI risk assessment. The developed model would also be applied for assessing repeated-dose drug toxicity, combined drug synergistic toxicities and disease modelling.

7. Impact of the research in the advancement of knowledge or benefit to mankind

The high failure rates of drugs in phase II/III clinical trials and withdrawal of the marketed drugs are mainly ascribed to the genetic and physiological differences between animals and humans as well as the existence of over simplified *in vitro* experimental models. Here, we have microengineered a human physiomimetic 3D printed *in vitro* liver acinus model using transdisciplinary technologies for detecting diverse phenotypes of DILI. The first phase of the study discusses about the fundamental steps to unravel the formulation of a cell instructive liver mimetic biomaterial ink demonstrating multifunctional traits for recapitulating the liver-specific extracellular matrix microenvironment and mechanics. Using this multifunctional biomaterial ink, a liver acinus mimetic model was 3D printed to recapitulate the native hierarchical arrangement of the cords of hepatocytes separated by functional sinusoidal microvasculature networks. Further to maximally emulate the key physiological features of the human liver acinus i.e. physiologically relevant flow conditions and shear stress effects on cells, vascularization and flow-based stimulation of cells for enhanced release of signalling molecules as well as secretome components we conceptualized and developed a next generation structured human physiomimetic liver acinus platform ‘fit-for-the-purpose’ of investigating diverse phenotype of DILI in a high throughput manner. Computational flow simulations of the model suggested that the transfer of oxygen or nutrients inside the scaffolds is predominantly diffusion-driven and the flow characteristics mimicked the *in vivo* blood flow pattern in the hepatic sinusoids. Moreover, to recreate the liver acinus cellular microenvironment and add a higher order of biological complexity to the model, we integrated the 3D printed liver acinus model with matured HLCs, HUVECs and HHSCs to emulate the physiologically relevant cellular combination and improve the long-term physiological functionality. Following 15 days of maturation, our developed tricultured HPLAM platform in the perfusion condition was able to demonstrate more physiologically relevant function with enhanced cellular viability, colonization and proliferation in comparison to the static condition. The albumin and urea produced in the perfused HPLAM on day 10 and day 15 was similar to the albumin and urea production levels observed in human liver *in vivo* conditions as per the data obtained through

in vitro-to-in vivo extrapolation technique. Further evaluation of the drug metabolizing capacity of the liver model also revealed that the perfused tricultured model showed enhanced CYP activity similar to the levels observed in freshly isolated hepatocytes over 15 days of culture period. In line with the changes in the secretome levels observed, the gene expression studies and immunofluorescence staining also confirmed the enhanced expression of the HLC, HUVEC and HHSC specific genes and markers in the perfused tricultured liver acinus model in comparison to the static model. Thus, the perfused tricultured liver acinus matured model acted as metabolic biofactories and an optimal analog of the vascularized liver acinus-like microenvironment suitable for evaluating diverse phenotypes of drug toxicity. Furthermore, the bioinformatics-based analysis of gene and protein interaction networks indicated both functional and physical associations among the expressed and interactive genes, which are predicted to play a vital role in the maturation of the liver model.

Further evaluation of the drug responsiveness of the liver acinus model revealed that the perfused HPLAM predicted diverse phenotype of DILI with more human specific sensitivity at clinically relevant doses. Overall, the developed human physiомimetic 3D printed in vitro liver acinus model has great potential to address patient-specific absorption, distribution, metabolism, excretion and toxicity (ADMET) and serve as disease model platform for application related to therapeutic discovery and development, pathophysiological studies, precision medicine and pre-clinical trials. Moreover, it also opens up new possibilities for the development of next generation physiомimetic in vitro liver models as a multi-omics platform through inclusion of induced pluripotent stem cells-derived human liver organoids in the developed liver mimetic biomaterial ink for the fabrication of a 3D bioprinted liver acinus model towards a more predictive patient specific platform that may improve further DILI risk assessment in a reproducible manner.

Supporting Information

Supplementary results include Figure S1: Characterization of the decellularized porcine liver tissue; Figure S2: Porosity and cumulative protein release of the 3D printed scaffolds; Figure S3: Dimensions of the 3D printed microfluidic device; Figure S4: Characterization of the differentiated human adipose derived mesenchymal stem cells (ADMSCs) towards hepatocyte-like cells (HLCs); Table S1: List of genes and the forward and reverse primer sequences used for gene expression analysis; Table S2: Description of the genes identified in the gene

interaction network obtained using GeneMANIA database; Table S3: Description of the input and predicted functional partner proteins obtained from STRING database; Table S4: Protein-protein interaction network statistics and combined score annotation obtained using STRING database; Video S1: Procedure for the assembly of the human physiomimetic 3D printed in vitro liver acinus model.

Acknowledgements

B.B.M. acknowledges the funding support from the SwarnaJayanti Fellowship grant (Grant No. SB/SJF/2020-21/14), Science and Engineering Research Board (SERB), Department of Science and Technology (DST) and the Department of Biotechnology (DBT), Government of India. S.D. acknowledges the Ministry of Education (MoE), Government of India for providing Prime Minister's Research Fellowship (PMRF). A.B., G.J. and V.S. acknowledges the MoE, Government of India for providing fellowship. The Central Instrumentation Facility (CIF), Department of Biosciences and Bioengineering and the Centre for Nanotechnology, Indian Institute of Technology Guwahati are acknowledged for providing high end instrumentation support.

Conflict of interest

The authors declare no competing financial interests.

Literature References

- [1] D.E. Ingber, Human organs-on-chips for disease modelling, drug development and personalized medicine, *Nature Reviews Genetics* 23(8) (2022) 467-491.
- [2] J.H. Hoofnagle, E.S. Björnsson, Drug-induced liver injury—types and phenotypes, *New England Journal of Medicine* 381(3) (2019) 264-273.
- [3] R.J. Andrade, N. Chalasani, E.S. Björnsson, A. Suzuki, G.A. Kullak-Ublick, P.B. Watkins, H. Devarbhavi, M. Merz, M.I. Lucena, N. Kaplowitz, Drug-induced liver injury, *Nature Reviews Disease Primers* 5(1) (2019) 58.
- [4] R.J. Weaver, E.A. Blomme, A.E. Chadwick, I.M. Copple, H.H. Gerets, C.E. Goldring, A. Guillouzo, P.G. Hewitt, M. Ingelman-Sundberg, K.G. Jensen, Managing the challenge of drug-induced liver injury: a roadmap for the development and deployment of preclinical predictive models, *Nature Reviews Drug Discovery* 19(2) (2020) 131-148.
- [5] J.C. Fernandez-Checa, P. Bagnaninchi, H. Ye, P. Sancho-Bru, J.M. Falcon-Perez, F. Royo, C. Garcia-Ruiz, O. Konu, J. Miranda, O. Lunov, Advanced preclinical models for evaluation of drug-induced liver injury—consensus statement by the European Drug-Induced Liver Injury Network [PRO-EURO-DILI-NET], *Journal of Hepatology* 75(4) (2021) 935-959.

- [6] H. Olson, G. Betton, D. Robinson, K. Thomas, A. Monro, G. Kolaja, P. Lilly, J. Sanders, G. Sipes, W. Bracken, Concordance of the toxicity of pharmaceuticals in humans and in animals, *Regulatory toxicology and pharmacology* 32(1) (2000) 56-67.
- [7] G. Janani, S. Priya, S. Dey, B.B. Mandal, Mimicking native liver lobule microarchitecture in vitro with parenchymal and non-parenchymal cells using 3D bioprinting for drug toxicity and drug screening applications, *ACS Applied Materials & Interfaces* 14(8) (2022) 10167-10186.
- [8] H. Dirven, G.E. Vist, S. Bandhakavi, J. Mehta, S.E. Fitch, P. Pound, R. Ram, B. Kincaid, C.H. Leenaars, M. Chen, Performance of preclinical models in predicting drug-induced liver injury in humans: a systematic review, *Scientific reports* 11(1) (2021) 6403.
- [9] Ministry of Health and Family Welfare, Government of India. New Drugs and Clinical Trials (Amendment) Rules, 2023, *The Gazette of India*, 2023.
- [10] A. Gough, A. Soto-Gutierrez, L. Verneti, M.R. Ebrahimkhani, A.M. Stern, D.L. Taylor, Human biomimetic liver microphysiology systems in drug development and precision medicine, *Nature Reviews Gastroenterology & Hepatology* 18(4) (2021) 252-268.
- [11] D. Huh, B.D. Matthews, A. Mammoto, M. Montoya-Zavala, H.Y. Hsin, D.E. Ingber, Reconstituting organ-level lung functions on a chip, *Science* 328(5986) (2010) 1662-1668.
- [12] Y. Du, N. Li, H. Yang, C. Luo, Y. Gong, C. Tong, Y. Gao, S. Lü, M. Long, Mimicking liver sinusoidal structures and functions using a 3D-configured microfluidic chip, *Lab on a Chip* 17(5) (2017) 782-794.
- [13] L.A. Verneti, N. Senutovitch, R. Boltz, R. DeBiasio, T. Ying Shun, A. Gough, D.L. Taylor, A human liver microphysiology platform for investigating physiology, drug safety, and disease models, *Experimental biology and medicine* 241(1) (2016) 101-114.
- [14] X. Li, S.M. George, L. Verneti, A.H. Gough, D.L. Taylor, A glass-based, continuously zoned and vascularized human liver acinus microphysiological system (vLAMPS) designed for experimental modeling of diseases and ADME/TOX, *Lab on a Chip* 18(17) (2018) 2614-2631.
- [15] N. Freyer, S. Greuel, F. Knöspel, F. Gerstmann, L. Storch, G. Damm, D. Seehofer, J. Foster Harris, R. Iyer, F. Schubert, Microscale 3D liver bioreactor for in vitro hepatotoxicity testing under perfusion conditions, *Bioengineering* 5(1) (2018) 24.
- [16] M. Chen, A. Suzuki, S. Thakkar, K. Yu, C. Hu, W. Tong, DILIrank: the largest reference drug list ranked by the risk for developing drug-induced liver injury in humans, *Drug discovery today* 21(4) (2016) 648-653.
- [17] G. Lee, H. Kim, J.Y. Park, G. Kim, J. Han, S. Chung, J.H. Yang, J.S. Jeon, D.-H. Woo, C. Han, Generation of uniform liver spheroids from human pluripotent stem cells for imaging-based drug toxicity analysis, *Biomaterials* 269 (2021) 120529.
- [18] B.D. Cosgrove, B.M. King, M.A. Hasan, L.G. Alexopoulos, P.A. Farazi, B.S. Hendriks, L.G. Griffith, P.K. Sorger, B. Tidor, J.J. Xu, Synergistic drug–cytokine induction of hepatocellular death as an in vitro approach for the study of inflammation-associated idiosyncratic drug hepatotoxicity, *Toxicology and applied pharmacology* 237(3) (2009) 317-330.
- [19] D.G. Nguyen, J. Funk, J.B. Robbins, C. Crogan-Grundy, S.C. Presnell, T. Singer, A.B. Roth, Bioprinted 3D primary liver tissues allow assessment of organ-level response to clinical drug induced toxicity in vitro, *PloS one* 11(7) (2016) e0158674.
- [20] Y. Jin, J. Kim, J.S. Lee, S. Min, S. Kim, D.H. Ahn, Y.G. Kim, S.W. Cho, Vascularized liver organoids generated using induced hepatic tissue and dynamic liver - specific microenvironment as a drug testing platform, *Advanced Functional Materials* 28(37) (2018) 1801954.

- [21] N.S. Bhise, V. Manoharan, S. Massa, A. Tamayol, M. Ghaderi, M. Miscuglio, Q. Lang, Y.S. Zhang, S.R. Shin, G. Calzone, A liver-on-a-chip platform with bioprinted hepatic spheroids, *Biofabrication* 8(1) (2016) 014101.
- [22] M. Kumar, P. Gupta, S. Bhattacharjee, S.K. Nandi, B.B. Mandal, Immunomodulatory injectable silk hydrogels maintaining functional islets and promoting anti-inflammatory M2 macrophage polarization, *Biomaterials* 187 (2018) 1-17.
- [23] B. Bhar, B. Chakraborty, S.K. Nandi, B.B. Mandal, Silk-based phyto-hydrogel formulation expedites key events of wound healing in full-thickness skin defect model, *International Journal of Biological Macromolecules* 203 (2022) 623-637.
- [24] G. Janani, B.B. Mandal, Mimicking physiologically relevant hepatocyte zonation using immunomodulatory silk liver extracellular matrix scaffolds toward a bioartificial liver platform, *ACS Applied Materials & Interfaces* 13(21) (2021) 24401-24421.
- [25] J.C. Moses, S. Dey, A. Bandyopadhyay, M. Agarwala, B.B. Mandal, Silk - based bioengineered diaphyseal cortical bone unit enclosing an implantable bone marrow toward atrophic nonunion grafting, *Advanced Healthcare Materials* 11(6) (2022) 2102031.
- [26] S.-H. Park, E.S. Gil, H. Cho, B.B. Mandal, L.W. Tien, B.-H. Min, D.L. Kaplan, Intervertebral disk tissue engineering using biphasic silk composite scaffolds, *Tissue Engineering Part A* 18(5-6) (2012) 447-458.
- [27] C. Jaiswal, T. Gupta, P.K. Jadi, J.C. Moses, B.B. Mandal, Injectable anti-cancer drug loaded silk-based hydrogel for the prevention of cancer recurrence and post-lumpectomy tissue regeneration aiding triple-negative breast cancer therapy, *Biomaterials Advances* 145 (2023) 213224.
- [28] S. Mehrotra, R.D. Singh, A. Bandyopadhyay, G. Janani, S. Dey, B.B. Mandal, Engineering microsphere-loaded non-mulberry silk-based 3D bioprinted vascularized cardiac patches with oxygen-releasing and immunomodulatory potential, *ACS Applied Materials & Interfaces* 13(43) (2021) 50744-50759.
- [29] D.J. Vitello, R.M. Ripper, M.R. Fettiplace, G.L. Weinberg, J.M. Vitello, Blood density is nearly equal to water density: a validation study of the gravimetric method of measuring intraoperative blood loss, *Journal of veterinary medicine* 2015 (2015).
- [30] N. Perrira, A.S. Shuib, S.W. Phang, A.S. Muda, Experimental Investigation of Blood Mimicking Fluid Viscosity for Application in 3D-Printed Medical Simulator, *Journal of Physics: Conference Series*, IOP Publishing, 2022, p. 012016.
- [31] G. Puhl, K.D. Schaser, B. Vollmar, M.D. Menger, U. Settmacher, Noninvasive in vivo analysis of the human hepatic microcirculation using orthogonal polarization spectral imaging, *Transplantation* 75(6) (2003) 756-761.
- [32] H. Singh, S.-H. Teoh, H.T. Low, D. Huttmacher, Flow modelling within a scaffold under the influence of uni-axial and bi-axial bioreactor rotation, *Journal of biotechnology* 119(2) (2005) 181-196.
- [33] C. Poon, Measuring the density and viscosity of culture media for optimized computational fluid dynamics analysis of in vitro devices, *Journal of the Mechanical Behavior of Biomedical Materials* 126 (2022) 105024.
- [34] A. Borbora, Y. Xu, S. Dey, X. Wang, Y. Yao, B.B. Mandal, X. Wang, U. Manna, Lubricated Interfaces Enabling Simultaneous Pulsatile and Continuous Chemical Release Modes, *Advanced Materials* (2023) 2302264.
- [35] J. Lee, V. Manoharan, L. Cheung, S. Lee, B.-H. Cha, P. Newman, R. Farzad, S. Mehrotra, K. Zhang, F. Khan, Nanoparticle-based hybrid scaffolds for deciphering the role of multimodal cues in cardiac tissue engineering, *ACS nano* 13(11) (2019) 12525-12539.

- [36] G. Hong, J. Kim, H. Oh, S. Yun, C.M. Kim, Y.M. Jeong, W.S. Yun, J.H. Shim, I. Jang, C.Y. Kim, Production of multiple cell - laden microtissue spheroids with a biomimetic hepatic - lobule - like structure, *Advanced Materials* 33(36) (2021) 2102624.
- [37] D. Warde-Farley, S.L. Donaldson, O. Comes, K. Zuberi, R. Badrawi, P. Chao, M. Franz, C. Grouios, F. Kazi, C.T. Lopes, The GeneMANIA prediction server: biological network integration for gene prioritization and predicting gene function, *Nucleic acids research* 38(suppl_2) (2010) W214-W220.
- [38] D. Szklarczyk, A. Franceschini, S. Wyder, K. Forslund, D. Heller, J. Huerta-Cepas, M. Simonovic, A. Roth, A. Santos, K.P. Tsafou, STRING v10: protein–protein interaction networks, integrated over the tree of life, *Nucleic acids research* 43(D1) (2015) D447-D452.
- [39] K.M. Bircsak, R. DeBiasio, M. Miedel, A. Alsebah, R. Reddinger, A. Saleh, T. Shun, L.A. Verneti, A. Gough, A 3D microfluidic liver model for high throughput compound toxicity screening in the OrganoPlate®, *Toxicology* 450 (2021) 152667.
- [40] M.K. Kim, W. Jeong, S.M. Lee, J.B. Kim, S. Jin, H.-W. Kang, Decellularized extracellular matrix-based bio-ink with enhanced 3D printability and mechanical properties, *Biofabrication* 12(2) (2020) 025003.
- [41] H. Lee, W. Han, H. Kim, D.-H. Ha, J. Jang, B.S. Kim, D.-W. Cho, Development of liver decellularized extracellular matrix bioink for three-dimensional cell printing-based liver tissue engineering, *Biomacromolecules* 18(4) (2017) 1229-1237.
- [42] P. Gupta, G.R. Chaudhuri, G. Janani, M. Agarwala, D. Ghosh, S.K. Nandi, B.B. Mandal, Functionalized Silk Vascular Grafts with Decellularized Human Wharton's Jelly Improves Remodeling via Immunomodulation in Rabbit Jugular Vein, *Advanced Healthcare Materials* 10(19) (2021) 2100750.
- [43] H. Kim, B. Kang, X. Cui, S.H. Lee, K. Lee, D.W. Cho, W. Hwang, T.B. Woodfield, K.S. Lim, J. Jang, Light - activated decellularized extracellular matrix - based bioinks for volumetric tissue analogs at the centimeter scale, *Advanced Functional Materials* 31(32) (2021) 2011252.
- [44] A. Bandyopadhyay, S.K. Chowdhury, S. Dey, J.C. Moses, B.B. Mandal, Silk: A promising biomaterial opening new vistas towards affordable healthcare solutions, *Journal of the Indian Institute of Science* 99(3) (2019) 445-487.
- [45] Y.P. Singh, A. Bandyopadhyay, B.B. Mandal, 3D bioprinting using cross-linker-free silk–gelatin bioink for cartilage tissue engineering, *ACS applied materials & interfaces* 11(37) (2019) 33684-33696.
- [46] L. Ma, Y. Wu, Y. Li, A. Aazmi, H. Zhou, B. Zhang, H. Yang, Current advances on 3D - bioprinted liver tissue models, *Advanced Healthcare Materials* 9(24) (2020) 2001517.
- [47] B.K. Bhunia, D.L. Kaplan, B.B. Mandal, Silk-based multilayered angle-ply annulus fibrosus construct to recapitulate form and function of the intervertebral disc, *Proceedings of the National Academy of Sciences* 115(3) (2018) 477-482.
- [48] B.K. Bhunia, S. Dey, A. Bandyopadhyay, B.B. Mandal, 3D printing of annulus fibrosus anatomical equivalents recapitulating angle-ply architecture for intervertebral disc replacement, *Applied Materials Today* 23 (2021) 101031.
- [49] S. Mehrotra, B.A.G. de Melo, M. Miscuglio, K. Kiaee, S.R. Shin, B.B. Mandal, Mimicking native heart tissue physiology and pathology in silk fibroin constructs through a perfusion - based dynamic mechanical stimulation microdevice, *Advanced Healthcare Materials* 11(6) (2022) 2101678.
- [50] A.P. Kourouklis, K.B. Kaylan, G.H. Underhill, Substrate stiffness and matrix composition coordinately control the differentiation of liver progenitor cells, *Biomaterials* 99 (2016) 82-94.

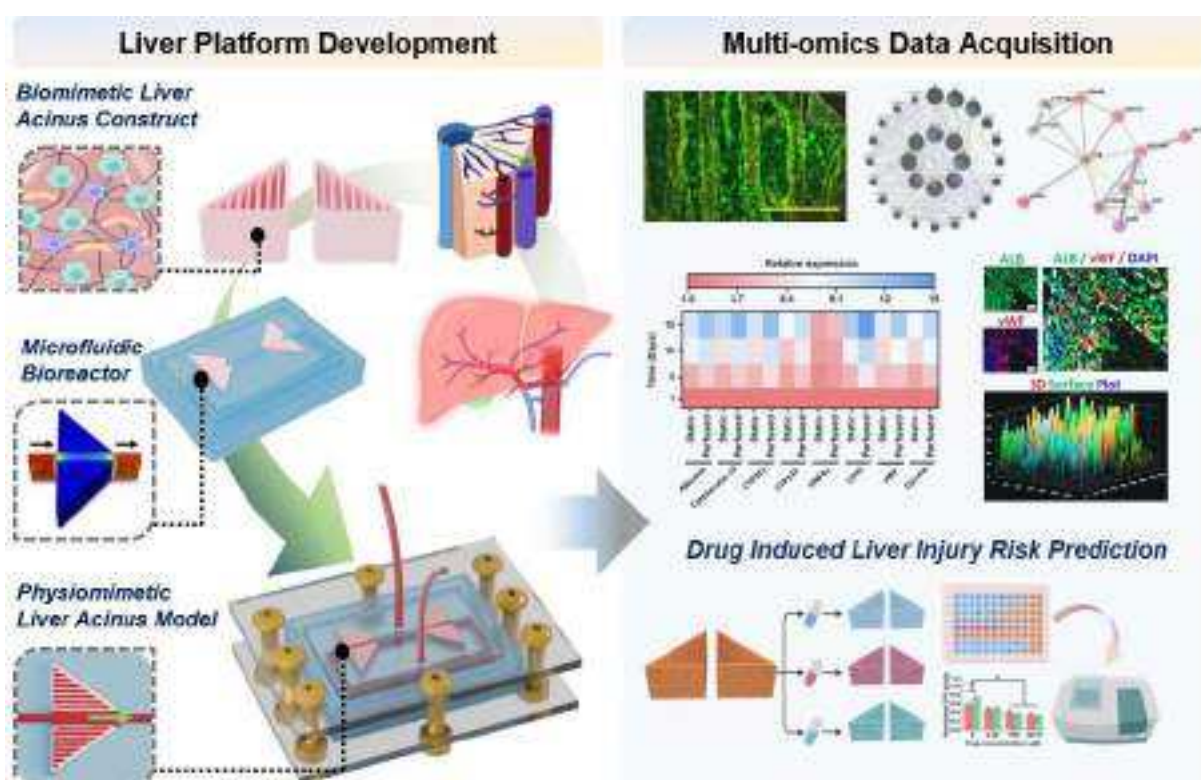
- [51] S.J. Blackford, T. Tracy, M.D. Norman, A.M. Syanda, M. Manolakakis, D. Lachowski, Z. Yan, Y. Guo, E. Garitta, F. Riccio, RGD density along with substrate stiffness regulate hPSC hepatocyte functionality through YAP signalling, *Biomaterials* 293 (2023) 121982.
- [52] T. Xia, R. Zhao, F. Feng, L. Yang, The effect of matrix stiffness on human hepatocyte migration and function—an in vitro research, *Polymers* 12(9) (2020) 1903.
- [53] V. Natarajan, E.J. Berglund, D.X. Chen, S. Kidambi, Substrate stiffness regulates primary hepatocyte functions, *RSC advances* 5(99) (2015) 80956-80966.
- [54] A. Karimi, A. Shojaei, An experimental study to measure the mechanical properties of the human liver, *Digestive Diseases* 36(2) (2018) 150-155.
- [55] M. Ruoff, S. Rebholz, M. Weimer, C. Grom-Baumgarten, K. Athanasopulu, R. Kemkemer, H. Käß, S. Ehnert, A.K. Nussler, Development of scaffolds with adjusted stiffness for mimicking disease-related alterations of liver rigidity, *Journal of functional biomaterials* 11(1) (2020) 17.
- [56] E. Moradi, S. Jalili-Firoozinezhad, M. Solati-Hashjin, Microfluidic organ-on-a-chip models of human liver tissue, *Acta biomaterialia* 116 (2020) 67-83.
- [57] P. Sphabmixay, M.S.B. Raredon, A.J. Wang, H. Lee, P.T. Hammond, N.X. Fang, L.G. Griffith, High resolution stereolithography fabrication of perfusable scaffolds to enable long-term meso-scale hepatic culture for disease modeling, *Biofabrication* 13(4) (2021) 045024.
- [58] N. Berndt, H.-G. Holzhütter, Dynamic metabolic zonation of the hepatic glucose metabolism is accomplished by sinusoidal plasma gradients of nutrients and hormones, *Frontiers in physiology* 9 (2018) 1786.
- [59] K.-J. Jang, M.A. Otieno, J. Ronxhi, H.-K. Lim, L. Ewart, K.R. Kodella, D.B. Petropolis, G. Kulkarni, J.E. Rubins, D. Conegliano, Reproducing human and cross-species drug toxicities using a Liver-Chip, *Science translational medicine* 11(517) (2019) eaax5516.
- [60] B.E. Uygun, A. Soto-Gutierrez, H. Yagi, M.-L. Izamis, M.A. Guzzardi, C. Shulman, J. Milwid, N. Kobayashi, A. Tilles, F. Berthiaume, Organ reengineering through development of a transplantable recellularized liver graft using decellularized liver matrix, *Nature medicine* 16(7) (2010) 814-820.
- [61] L. Ewart, A. Apostolou, S.A. Briggs, C.V. Carman, J.T. Chaff, A.R. Heng, S. Jadalannagari, J. Janardhanan, K.-J. Jang, S.R. Joshipura, Performance assessment and economic analysis of a human Liver-Chip for predictive toxicology, *Communications Medicine* 2(1) (2022) 154.
- [62] X. Ma, X. Qu, W. Zhu, Y.-S. Li, S. Yuan, H. Zhang, J. Liu, P. Wang, C.S.E. Lai, F. Zanella, Deterministically patterned biomimetic human iPSC-derived hepatic model via rapid 3D bioprinting, *Proceedings of the National Academy of Sciences* 113(8) (2016) 2206-2211.
- [63] F. Lakehal, D. Wendum, V. Barbu, L. Becquemont, R. Poupon, P. Balladur, L. Hannoun, F. Ballet, P.H. Beaune, C. Housset, Phase I and phase II drug - metabolizing enzymes are expressed and heterogeneously distributed in the biliary epithelium, *Hepatology* 30(6) (1999) 1498-1506.
- [64] A. Rubiano, A. Indapurkar, R. Yokosawa, A. Miedzik, B. Rosenzweig, A. Arefin, C.M. Moulin, K. Dame, N. Hartman, D.A. Volpe, Characterizing the reproducibility in using a liver microphysiological system for assaying drug toxicity, metabolism, and accumulation, *Clinical and translational science* 14(3) (2021) 1049-1061.
- [65] B. Delalat, C. Cozzi, S. Rasi Ghaemi, G. Polito, F.H. Kriel, T.D. Michl, F.J. Harding, C. Priest, G. Barillaro, N.H. Voelcker, Microengineered bioartificial liver chip for drug toxicity screening, *Advanced functional materials* 28(28) (2018) 1801825.

- [66] A. Chhabra, H.-H.G. Song, K.A. Grzelak, W.J. Polacheck, H.E. Fleming, C.S. Chen, S.N. Bhatia, A vascularized model of the human liver mimics regenerative responses, *Proceedings of the National Academy of Sciences* 119(28) (2022) e2115867119.
- [67] I. Manov, H. Motanis, I. Frumin, T.C. Iancu, Hepatotoxicity of anti-inflammatory and analgesic drugs: ultrastructural aspects, *Acta Pharmacologica Sinica* 27(3) (2006) 259-272.
- [68] H.J. Zimmerman, Effects of aspirin and acetaminophen on the liver, *Archives of Internal Medicine* 141(3) (1981) 333-342.
- [69] U.S. Food & Drug Administration: CFR-code of federal regulations title 21, 2017.
- [70] J. Laster, R. Satoskar, Aspirin-induced acute liver injury, *ACG case reports journal* 2(1) (2014) 48.
- [71] H. Eken, H. Ozturk, H. Ozturk, H. Buyukbayram, Dose-related effects of dexamethasone on liver damage due to bile duct ligation in rats, *World Journal of Gastroenterology: WJG* 12(33) (2006) 5379.
- [72] H. Oh, S. Namkoong, S. Lee, C. Kim, T. Billiar, J. Han, K. Ha, H. Chung, Y. Kwon, H. Lee, Dexamethasone protects primary cultured hepatocytes from death receptor-mediated apoptosis by upregulation of cFLIP, *Cell Death & Differentiation* 13(3) (2006) 512-523.
- [73] T. Kaden, K. Graf, K. Rennert, R. Li, A.S. Mosig, M. Raasch, Evaluation of drug-induced liver toxicity of trovafloxacin and levofloxacin in a human microphysiological liver model, *Scientific Reports* 13(1) (2023) 13338.
- [74] J. Vincent, R. Teng, D.K. Dalvie, H.L. Friedman, Pharmacokinetics and metabolism of single oral doses of trovafloxacin, *The American journal of surgery* 176(6) (1998) 8S-13S.
- [75] J. Kohloser, J. Mathai, J. Reichheld, B.F. Banner, H.L. Bonkovsky, Hepatotoxicity due to troglitazone: report of two cases and review of adverse events reported to the United States Food and Drug Administration, *The American journal of gastroenterology* 95(1) (2000) 272-276.
- [76] F.V. Schiødt, F.A. Rochling, D.L. Casey, W.M. Lee, Acetaminophen toxicity in an urban county hospital, *New England Journal of Medicine* 337(16) (1997) 1112-1118.
- [77] B. Mégarbane, N. Deye, F.J. Baud, Acetaminophen poisoning, *The New England Journal of Medicine* 359(18) (2008) 1962-3; author reply 1965.
- [78] P.B. Watkins, Insight into hepatotoxicity: the troglitazone experience, *LWW*, 2005, pp. 229-230.
- [79] J.E. Henney, Withdrawal of troglitazone and cisapride, *Jama* 283(17) (2000) 2228-2228.
- [80] U.S. Food & Drug Administration. FDA drug safety communication: prescription acetaminophen products to be limited to 325 mg per dosage unit; boxed warning will highlight potential for severe liver failure, (2011).
- [81] B.R. Ware, D.R. Berger, S.R. Khetani, Prediction of drug-induced liver injury in micropatterned co-cultures containing iPSC-derived human hepatocytes, *Toxicological sciences* 145(2) (2015) 252-262.
- [82] F. Li, L. Cao, S. Parikh, R. Zuo, Three-dimensional spheroids with primary human liver cells and differential roles of Kupffer cells in drug-induced liver injury, *Journal of pharmaceutical sciences* 109(6) (2020) 1912-1923.
- [83] M. Jang, P. Neuzil, T. Volk, A. Manz, A. Kleber, On-chip three-dimensional cell culture in phaseguides improves hepatocyte functions in vitro, *Biomicrofluidics* 9(3) (2015).

TABLE OF CONTENTS (ToC) GRAPHIC

Microfluidic Human Physiometric Liver Model as a Screening Platform Recapitulates Intrinsic and Idiosyncratic Drug Toxicity

*Souradeep Dey, Amritha Bhat, Janani G, Vartik Shandilya, Raghvendra Gupta, Biman B. Mandal**



In line with the evolution of in vitro liver models, a human physiometric liver acinus model (HPLAM) is bioengineered using transdisciplinary technologies for assessing diverse phenotypes of drug induced liver injury with more human specific sensitivity. The microfluidic bioreactor-based HPLAM acts as metabolic biofactories emulating in vivo like hepatic functionality and demonstrates dose- and time-dependent hepatotoxic response of human relevance.

Supporting Information

Figure S1: Characterization of the decellularized porcine liver tissue; Figure S2: Porosity, swelling behaviour, degradation behaviour and cumulative protein release of the 3D printed scaffolds; Figure S3: Dimensions of the 3D printed microfluidic device; Figure S4: Characterization of the differentiated human adipose derived mesenchymal stem cells (ADMSCs) towards hepatocyte-like cells (HLCs); Table S1: List of genes and the forward and reverse primer sequences used for gene expression analysis; Table S2: Description of the genes identified in the gene interaction network obtained using GeneMANIA database; Table S3: Description of the input and predicted functional partner proteins obtained from STRING database; Table S4: Protein-protein interaction network statistics and combined score annotation obtained using STRING database; Video S1: Procedure for the assembly of the human physiommimetic 3D printed in vitro liver acinus model.

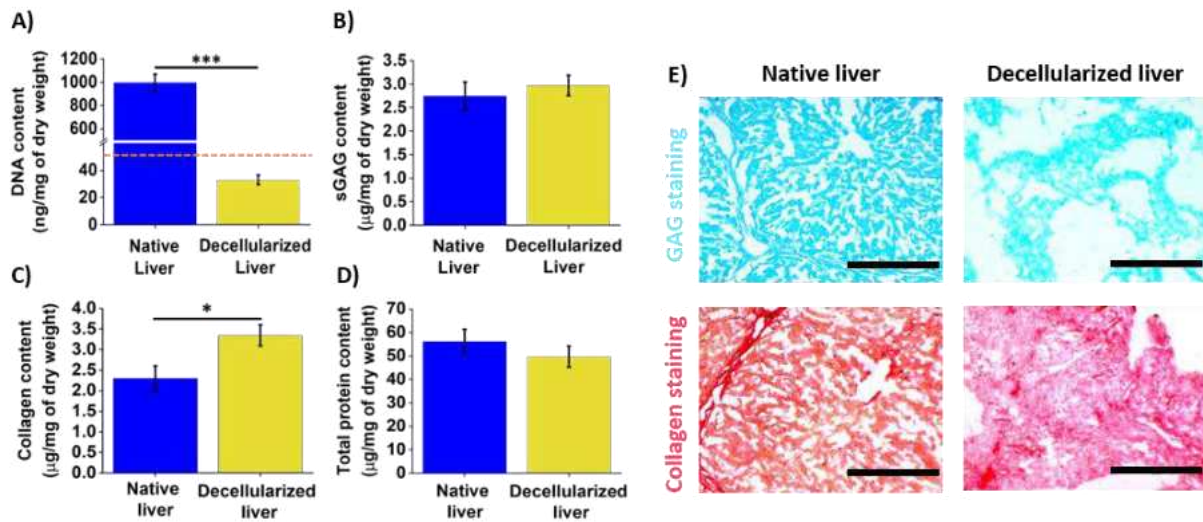


Figure S1: Characterization of decellularized porcine liver tissue. Biochemical estimation of A) DNA content, B) sGAG content, C) Collagen content and D) Total protein content in native and decellularized liver. E) Alcian blue staining for sGAG and picrosirius staining for collagen of native and decellularized liver tissue. Scale bar: 400 μm . Data are expressed as Mean \pm S.D ($n=3$); where * and *** signify the statistical difference between the groups at $p \leq 0.05$ and $p \leq 0.001$, respectively. The dotted line represents the allowed threshold limit of DNA content in decellularized ECM.

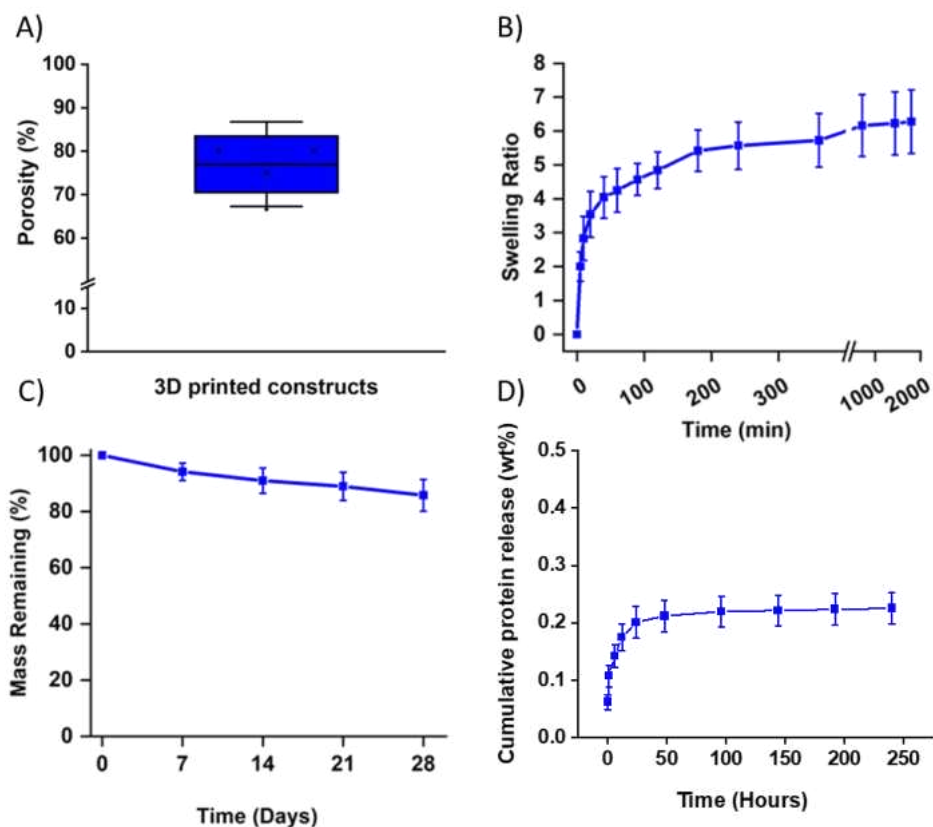


Figure S2: Physicochemical characterization of the 3D printed constructs. **A)** Porosity **B)** Swelling behaviour **C)** Degradation behaviour and **D)** Cumulative protein release (wt %) from the 3D printed scaffolds for over 10 days. Data are expressed as Mean \pm S.D. (n=5);

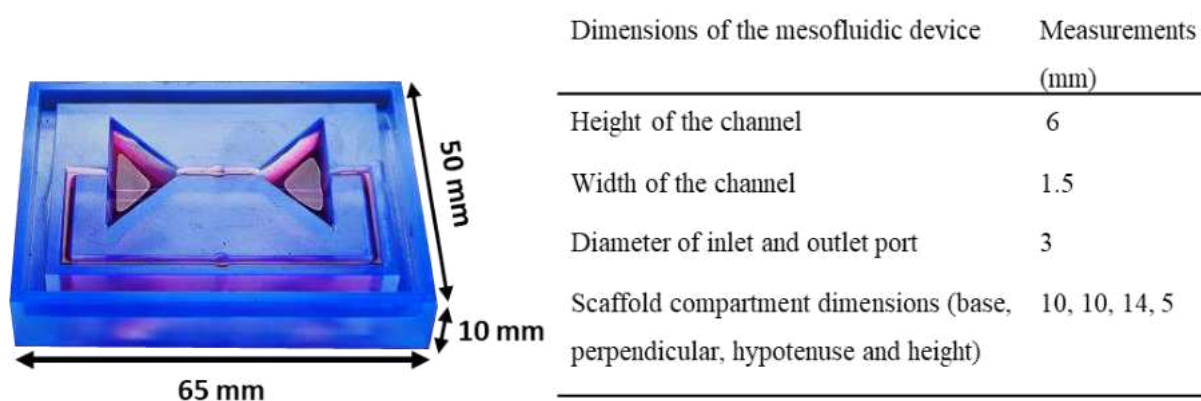


Figure S3: Dimensions of the 3D printed microfluidic device.

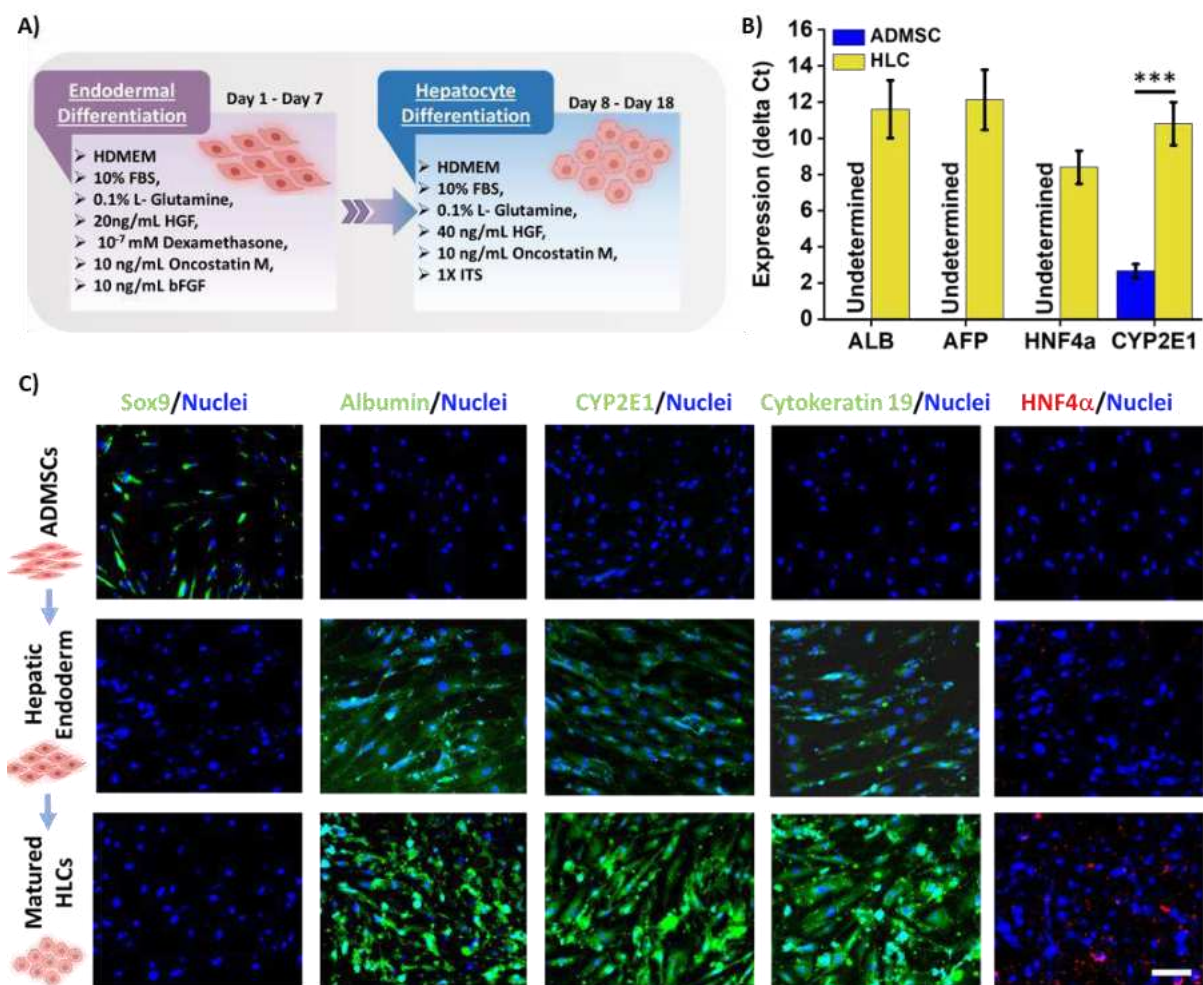


Figure S4: Characterization of differentiated human adipose derived mesenchymal stem cells (ADMSCs) towards hepatocyte-like cells (HLCs). **A)** Schematic illustration of the differentiation protocol of hADMSCs towards HLCs; **B)** Real time gene expression studies for ALB, CYP2E1, AFP and HNF4 α in hADMSCs and HLCs; **C)** Marker immunofluorescence images of hADMSCs, hepatic endoderm and mature HLCs for stem cell marker (SOX-9) and mature hepatocyte markers (Albumin, CYP2E1, Cytokeratin 18 and HNF4 α). Scale bar: 50 μ m. Data are expressed as Mean \pm S.D (n=3); where *** signify the statistical difference between the groups at $p \leq 0.001$, respectively.

Table S1: List of genes and the forward and reverse primer sequences used for gene expression analysis.

Sl. No.	Gene	Sequence	T _m (°C)	Accession Number
1	Human β -actin	F 5'-GGCATCCTCACCTGAAGTA-3' R 5'- GGGGTGTTGAAGGTCTCAAA-3'	60	NM_001101.5
2	Human SOX-9	F 5'-ACGGCTCCAGCAAGAACAAG-3' R 5'-TTGTGCAGATGCGGGTACTG-3'	60	NM_213843.1
3	Human ALB	F 5'-GTGCTAATTTCCCTCCGTTTGTC-3' R 5'- GCAACCTCACTCTTGTGTGC-3'	60	NM_000477.6
4	Human AFP	F 5'-AGCTTGGTGGTGGATGAAAC-3' R 5'-CCCTCTTCAGCAAAGCAGAC-3'	60	NM_001134.3
5	Human CYP2E1	F 5'-CGTGGAAATGGAGAAGGAAA-3' R 5'-GGTGATGAACCGCTGAATCT-3'	60	NM_000773.4
6	Human CYP1A2	F 5'-GCACTATCAGGACTTTGACA-3' R 5'-TTGGTCACAAGGTACATGAG-3'	60	NM_000761.4
7	Human HNF4 α	F 5'-CGAAGGTCAAGCTATGAGGACA-3' R 5'- ATCTGCGATGCTGGCAATCT-3'	60	NM_000457.6
8	Human CK-19	F 5'-AGCATGAAAGCTGCCTTGGA-3' R 5'-CCTGATTCTGCCGCTCACTATC-3'	60	NM_002276.5
9	Human CD31	F 5'-TCCGATGATAACCACTGCAA-3' R 5'-TGGTGGAGTCTGGAGAGGA-3'	60	XM_032908315.1
10	Human vWF	F 5'-TCTTCCAGGACTGCAACAAG-3' R 5'-TCCGAGATGTCCTCCACATA-3'	60	NM_000552.5
11	Human Desmin	F 5'-CATCGCGGCTAAGAACATTT-3' R 5'-GCCTCATCAGGGAATCGTTA-3'	60	NM_001382713.1

Table S2: Description of the genes identified in the gene interaction network obtained using GeneMANIA database.

Gene Name	Symbol	Score	Functions	Links (References)
Hepatocyte nuclear factor 4 alpha	HNF4A	0.60004	Carboxylic acid binding, cellular response to xenobiotic stimulus, monocarboxylic acid binding, organic acid binding, response to xenobiotic stimulus	http://www.ncbi.nlm.nih.gov/sites/entrez?db=gene&cmd=search&term=3172
Keratin 19	KRT19	0.592995	The protein encoded by this gene is a member of the keratin family. The keratins are intermediate filament proteins responsible for the structural integrity of epithelial cells and are subdivided into cytokeratins and hair keratins. The type I cytokeratins consist of acidic proteins which are arranged in pairs of heterotypic keratin chains. Unlike its related family members, this smallest known acidic cytokeratin is not paired with a basic cytokeratin in epithelial cells. It is specifically expressed in the periderm, the transiently superficial layer that envelopes the developing epidermis. The type I cytokeratins are clustered in a region of chromosome 17q12-q21.	http://www.ncbi.nlm.nih.gov/sites/entrez?db=gene&cmd=search&term=3880
Albumin	ALB	0.592882	Carboxylic acid binding, monocarboxylic acid binding, organic acid binding, vitamin binding	http://www.ncbi.nlm.nih.gov/sites/entrez?db=gene&cmd=search&term=213
Cytochrome P450 family 1 subfamily A member 2	CYP1A2	0.584359	Alcohol metabolic process, arachidonic acid metabolic process, carboxylic acid biosynthetic process, cellular hormone metabolic process, cellular response to xenobiotic stimulus, demethylation, diterpenoid metabolic process, drug catabolic process, drug metabolic process, fatty acid biosynthetic process, fatty acid derivative metabolic process, fatty acid metabolic process, hormone metabolic process, icosanoid metabolic process, isoprenoid metabolic process, long-chain fatty acid metabolic	http://www.ncbi.nlm.nih.gov/sites/entrez?db=gene&cmd=search&term=1544

			process, monocarboxylic acid biosynthetic process, monooxygenase activity, olefinic compound metabolic process, organic acid biosynthetic process, oxidoreductase activity, acting on CH or CH2 groups, oxidoreductase activity, acting on paired donors, with incorporation or reduction of molecular oxygen, primary alcohol metabolic process, response to drug, response to xenobiotic stimulus, retinoid metabolic process, steroid hydroxylase activity, steroid metabolic process, terpenoid metabolic process, tetrapyrrole binding, unsaturated fatty acid metabolic process	
Platelet and endothelial cell adhesion molecule 1	PECAM1	0.582561	Protein localization to cell-cell junction	http://www.ncbi.nlm.nih.gov/sites/entrez?db=gene&cmd=search&term=5175
Cytochrome P450 family 2 subfamily E member 1	CYP2E1	0.558468	Arachidonic acid metabolic process, arachidonic acid monooxygenase activity, carboxylic acid biosynthetic process, cellular response to xenobiotic stimulus, drug catabolic process, drug metabolic process, fatty acid biosynthetic process, fatty acid derivative metabolic process, fatty acid metabolic process, icosanoid metabolic process, isoprenoid metabolic process, long-chain fatty acid metabolic process, monocarboxylic acid biosynthetic process, monooxygenase activity, olefinic compound metabolic process, organic acid biosynthetic process, oxidoreductase activity, acting on paired donors, with incorporation or reduction of molecular oxygen, oxidoreductase activity, acting on paired donors, with incorporation or reduction of molecular oxygen, NAD(P)H as one donor, and incorporation of one atom of oxygen, response to drug, response to xenobiotic stimulus, terpenoid metabolic process, tetrapyrrole binding, unsaturated fatty acid metabolic process	http://www.ncbi.nlm.nih.gov/sites/entrez?db=gene&cmd=search&term=1571
Desmin	DES	0.536424	This gene encodes a muscle-specific class III intermediate filament. Homopolymers of this protein form a stable intracytoplasmic filamentous	http://www.ncbi.nlm.nih.gov/sites/entrez?db=

			network connecting myofibrils to each other and to the plasma membrane. Mutations in this gene are associated with desmin-related myopathy, a familial cardiac and skeletal myopathy (CSM), and with distal myopathies.	gene&cmd=search&term=1674
Von Willebrand factor	VWF	0.508497	This gene encodes a glycoprotein involved in hemostasis. The encoded preproprotein is proteolytically processed following assembly into large multimeric complexes. These complexes function in the adhesion of platelets to sites of vascular injury and the transport of various proteins in the blood. Mutations in this gene result in von Willebrand disease, an inherited bleeding disorder. An unprocessed pseudogene has been found on chromosome 22.	http://www.ncbi.nlm.nih.gov/sites/entrez?db=gene&cmd=search&term=7450
GC vitamin D binding protein	GC	0.018354	Fat-soluble vitamin metabolic process, steroid metabolic process, vitamin binding, vitamin metabolic process	http://www.ncbi.nlm.nih.gov/sites/entrez?db=gene&cmd=search&term=2638
Alpha fetoprotein	AFP	0.018289	Carboxylic acid binding, monocarboxylic acid binding, organic acid binding	http://www.ncbi.nlm.nih.gov/sites/entrez?db=gene&cmd=search&term=174
Afamin	AFM	0.018074	Carboxylic acid binding, monocarboxylic acid binding, organic acid binding, vitamin binding	http://www.ncbi.nlm.nih.gov/sites/entrez?db=gene&cmd=search&term=173
Chromosome 17 open reading frame 99	C17orf99	0.009515	Predicted to enable transmembrane signaling receptor activity. Predicted to be involved in cell surface receptor signaling pathway; mature B cell differentiation involved in immune response; and positive regulation of immunoglobulin production in mucosal tissue. Located in extracellular space. [provided by Alliance of Genome Resources,	http://www.ncbi.nlm.nih.gov/sites/entrez?db=gene&cmd=search&term=100141515

Mast cell immunoglobulin like receptor 1	MILR1	0.00661	Predicted to enable transmembrane signaling receptor activity. Predicted to be involved in several processes, including cell-cell adhesion via plasma-membrane adhesion molecules; mast cell degranulation; and negative regulation of mast cell activation. Predicted to be integral component of plasma membrane.	http://www.ncbi.nlm.nih.gov/sites/entrez?db=gene&cmd=search&term=284021
Extracellular matrix protein 1	ECM1	0.005284	This gene encodes a soluble protein that is involved in endochondral bone formation, angiogenesis, and tumor biology. It also interacts with a variety of extracellular and structural proteins, contributing to the maintenance of skin integrity and homeostasis. Mutations in this gene are associated with lipoid proteinosis disorder (also known as hyalinosis cutis et mucosae or Urbach-Wiethe disease) that is characterized by generalized thickening of skin, mucosae and certain viscera. Alternatively spliced transcript variants encoding distinct isoforms have been described for this gene.	http://www.ncbi.nlm.nih.gov/sites/entrez?db=gene&cmd=search&term=1893
Cytochrome P450 family 7 subfamily A member 1	CYP7A1	0.005217	Alcohol metabolic process, carboxylic acid biosynthetic process, monocarboxylic acid biosynthetic process, monooxygenase activity, organic acid biosynthetic process, oxidoreductase activity, acting on paired donors, with incorporation or reduction of molecular oxygen, oxidoreductase activity, acting on paired donors, with incorporation or reduction of molecular oxygen, NAD(P)H as one donor, and incorporation of one atom of oxygen, steroid hydroxylase activity, steroid metabolic process	http://www.ncbi.nlm.nih.gov/sites/entrez?db=gene&cmd=search&term=1581
Inter-alpha-trypsin inhibitor heavy chain 2	ITIH2	0.005097	The inter-alpha-trypsin inhibitors (ITI) are a family of structurally related plasma serine protease inhibitors involved in extracellular matrix stabilization and in prevention of tumor metastasis. The ITI family contains multiple proteins made up of a light chain (see MIM 176870) and a variable number of heavy chains.	http://www.ncbi.nlm.nih.gov/sites/entrez?db=gene&cmd=search&term=3698
Cytochrome P450 family 2	CYP2B6	0.005062	Arachidonic acid metabolic process, arachidonic acid monooxygenase activity, cellular response to xenobiotic stimulus, drug catabolic process, drug metabolic process, fatty acid derivative metabolic process, fatty acid	http://www.ncbi.nlm.nih.gov/sites/entrez?db=gene&cmd=search&term=1581

subfamily B member 6			metabolic process, icosanoid metabolic process, long-chain fatty acid metabolic process, monooxygenase activity, olefinic compound metabolic process, oxidoreductase activity, acting on paired donors, with incorporation or reduction of molecular oxygen, oxidoreductase activity, acting on paired donors, with incorporation or reduction of molecular oxygen, NAD(P)H as one donor, and incorporation of one atom of oxygen, response to drug, response to xenobiotic stimulus, steroid hydroxylase activity, tetrapyrrole binding, unsaturated fatty acid metabolic process	gene&cmd=search&term=1555
Cytochrome P450 family 2 subfamily D member 6	CYP2D6	0.004826	Alcohol metabolic process, carboxylic acid biosynthetic process, cellular hormone metabolic process, cellular response to xenobiotic stimulus, demethylation, diterpenoid metabolic process, drug catabolic process, drug metabolic process, fatty acid biosynthetic process, fatty acid derivative metabolic process, fatty acid metabolic process, hormone metabolic process, icosanoid metabolic process, isoprenoid metabolic process, long-chain fatty acid metabolic process, monocarboxylic acid biosynthetic process, monooxygenase activity, olefinic compound metabolic process, organic acid biosynthetic process, oxidoreductase activity, acting on paired donors, with incorporation or reduction of molecular oxygen, oxidoreductase activity, acting on paired donors, with incorporation or reduction of molecular oxygen, NAD(P)H as one donor, and incorporation of one atom of oxygen, primary alcohol metabolic process, response to drug, response to xenobiotic stimulus, retinoid metabolic process, steroid metabolic process, terpenoid metabolic process, tetrapyrrole binding, unsaturated fatty acid metabolic process	http://www.ncbi.nlm.nih.gov/sites/entrez?db=gene&cmd=search&term=107987478
Inter-alpha-trypsin inhibitor heavy chain 1	ITIH1	0.004779	This gene encodes a member of the inter-alpha-trypsin inhibitor family of proteins. Alternative splicing results in multiple transcript variants, at least one of which encodes a preproprotein that is proteolytically processed to generate the heavy chain of the inter-alpha-trypsin inhibitor complex, which is secreted by hepatocytes into the blood. The heavy chain also	http://www.ncbi.nlm.nih.gov/sites/entrez?db=gene&cmd=search&term=3697

			interacts with hyaluronan, and this interaction may play a role in ovulation and fertilization, and has been implicated in multiple inflammatory diseases. This gene is present in a gene cluster on chromosome 3.	
Cytochrome P450 family 1 subfamily A member 1	CYP1A1	0.004661	Alcohol metabolic process, arachidonic acid metabolic process, carboxylic acid biosynthetic process, cellular hormone metabolic process, diterpenoid metabolic process, fat-soluble vitamin metabolic process, fatty acid biosynthetic process, fatty acid derivative metabolic process, fatty acid metabolic process, hormone metabolic process, icosanoid metabolic process, isoprenoid metabolic process, long-chain fatty acid metabolic process, monocarboxylic acid biosynthetic process, monooxygenase activity, olefinic compound metabolic process, organic acid biosynthetic process, oxidoreductase activity, acting on paired donors, with incorporation or reduction of molecular oxygen, primary alcohol metabolic process, retinoid metabolic process, steroid hydroxylase activity, steroid metabolic process, terpenoid metabolic process, unsaturated fatty acid metabolic process, vitamin metabolic process	http://www.ncbi.nlm.nih.gov/sites/entrez?db=gene&cmd=search&term=1543
Cytochrome P450 family 26 subfamily A member 1	CYP26A1	0.004467	Carboxylic acid binding, cellular hormone metabolic process, cellular response to xenobiotic stimulus, diterpenoid metabolic process, fat-soluble vitamin metabolic process, hormone metabolic process, isoprenoid metabolic process, monocarboxylic acid binding, monooxygenase activity, organic acid binding, oxidoreductase activity, acting on paired donors, with incorporation or reduction of molecular oxygen, response to xenobiotic stimulus, retinoid metabolic process, steroid metabolic process, terpenoid metabolic process, tetrapyrrole binding, vitamin metabolic process	http://www.ncbi.nlm.nih.gov/sites/entrez?db=gene&cmd=search&term=1592
Cytochrome P450 family 4	CYP4A11	0.004443	Arachidonic acid metabolic process, arachidonic acid monooxygenase activity, carboxylic acid biosynthetic process, fatty acid derivative metabolic process, fatty acid metabolic process, icosanoid metabolic	http://www.ncbi.nlm.nih.gov/sites/entrez?db=gene&cmd=search&term=1543

subfamily A member 11			process, long-chain fatty acid metabolic process, monooxygenase activity, olefinic compound metabolic process, organic acid biosynthetic process, oxidoreductase activity, acting on paired donors, with incorporation or reduction of molecular oxygen, oxidoreductase activity, acting on paired donors, with incorporation or reduction of molecular oxygen, NAD(P)H as one donor, and incorporation of one atom of oxygen, unsaturated fatty acid metabolic process	gene&cmd=search&term=1579
Cadherin 5	CDH5	0.00437	Protein localization to cell-cell junction	http://www.ncbi.nlm.nih.gov/sites/entrez?db=gene&cmd=search&term=1003
Cytochrome P450 family 2 subfamily C member 19	CYP2C19	0.004294	Arachidonic acid metabolic process, arachidonic acid monooxygenase activity, cellular response to xenobiotic stimulus, drug catabolic process, drug metabolic process, fatty acid derivative metabolic process, fatty acid metabolic process, icosanoid metabolic process, isoprenoid metabolic process, long-chain fatty acid metabolic process, monooxygenase activity, olefinic compound metabolic process, oxidoreductase activity, acting on paired donors, with incorporation or reduction of molecular oxygen, response to drug, response to xenobiotic stimulus, terpenoid metabolic process, tetrapyrrole binding, unsaturated fatty acid metabolic process	http://www.ncbi.nlm.nih.gov/sites/entrez?db=gene&cmd=search&term=1557
Inter-alpha-trypsin inhibitor heavy chain 3	ITIH3	0.004234	This gene encodes the heavy chain subunit of the pre-alpha-trypsin inhibitor complex. This complex may stabilize the extracellular matrix through its ability to bind hyaluronic acid. Polymorphisms of this gene may be associated with increased risk for schizophrenia and major depressive disorder. This gene is present in an inter-alpha-trypsin inhibitor family gene cluster on chromosome 3.	http://www.ncbi.nlm.nih.gov/sites/entrez?db=gene&cmd=search&term=3699
Cytochrome P450 family 3	CYP3A4	0.004146	Alcohol metabolic process, carboxylic acid biosynthetic process, cellular hormone metabolic process, cellular response to xenobiotic stimulus, demethylation, diterpenoid metabolic process, drug catabolic process,	http://www.ncbi.nlm.nih.gov/sites/entrez?db=gene&cmd=search&term=1579

subfamily A member 4			drug metabolic process, fat-soluble vitamin metabolic process, fatty acid biosynthetic process, fatty acid metabolic process, hormone metabolic process, isoprenoid metabolic process, long-chain fatty acid metabolic process, monocarboxylic acid biosynthetic process, monooxygenase activity, organic acid biosynthetic process, oxidoreductase activity, acting on CH or CH2 groups, oxidoreductase activity, acting on paired donors, with incorporation or reduction of molecular oxygen, primary alcohol metabolic process, response to drug, response to xenobiotic stimulus, retinoid metabolic process, steroid hydroxylase activity, steroid metabolic process, terpenoid metabolic process, vitamin metabolic process	gene&cmd=search&term=1576
Cytochrome P450 family 2 subfamily C member 9	CYP2C9	0.003987	Arachidonic acid metabolic process, arachidonic acid monooxygenase activity, carboxylic acid biosynthetic process, cellular hormone metabolic process, cellular response to xenobiotic stimulus, demethylation, drug catabolic process, drug metabolic process, fatty acid biosynthetic process, fatty acid derivative metabolic process, fatty acid metabolic process, hormone metabolic process, icosanoid metabolic process, isoprenoid metabolic process, long-chain fatty acid metabolic process, monocarboxylic acid biosynthetic process, monooxygenase activity, olefinic compound metabolic process, organic acid biosynthetic process, oxidoreductase activity, acting on CH or CH2 groups, oxidoreductase activity, acting on paired donors, with incorporation or reduction of molecular oxygen, response to drug, response to xenobiotic stimulus, steroid metabolic process, terpenoid metabolic process, tetrapyrrole binding, unsaturated fatty acid metabolic process	http://www.ncbi.nlm.nih.gov/sites/entrez?db=gene&cmd=search&term=1559
Cytochrome P450 family 2 subfamily C member 18	CYP2C18	0.003973	Arachidonic acid metabolic process, arachidonic acid monooxygenase activity, cellular hormone metabolic process, cellular response to xenobiotic stimulus, diterpenoid metabolic process, drug catabolic process, drug metabolic process, fatty acid derivative metabolic process, fatty acid metabolic process, hormone metabolic process, icosanoid	http://www.ncbi.nlm.nih.gov/sites/entrez?db=gene&cmd=search&term=1562

			metabolic process, isoprenoid metabolic process, long-chain fatty acid metabolic process, monooxygenase activity, olefinic compound metabolic process, oxidoreductase activity, acting on paired donors, with incorporation or reduction of molecular oxygen, response to drug, response to xenobiotic stimulus, retinoid metabolic process, terpenoid metabolic process, tetrapyrrole binding, unsaturated fatty acid metabolic process	
--	--	--	--	--

Table S3: Description of the input and predicted functional partner proteins obtained from STRING database.

Protein	Protein Description	Functions
AHSG	Alpha-2-HS-glycoprotein chain A	Promotes endocytosis, possesses opsonic properties and influences the mineral phase of bone. Shows affinity for calcium and barium ions; Belongs to the fetuin family.
ALB	Serum albumin	Serum albumin, the main protein of plasma, has a good binding capacity for water, Ca(2+), Na(+), K(+), fatty acids, hormones, bilirubin and drugs (Probable). Its main function is the regulation of the colloidal osmotic pressure of blood (Probable). Major zinc transporter in plasma, typically binds about 80% of all plasma zinc. Major calcium and magnesium transporter in plasma, binds approximately 45% of circulating calcium and magnesium in plasma.
CYP1A2	Cytochrome P450 1A2	A cytochrome P450 monooxygenase involved in the metabolism of various endogenous substrates, including fatty acids, steroid hormones and vitamins. Mechanistically, uses molecular oxygen inserting one oxygen atom into a substrate, and reducing the second into a water molecule, with two electrons provided by NADPH via cytochrome P450 reductase (NADPH--hemoprotein reductase). Catalyzes the hydroxylation of carbon-hydrogen bonds. Exhibits high catalytic activity for the formation of hydroxysteroids from estrone (E1) and 17beta- estradiol (E2), namely 2-hydroxy E1.

CYP2E1	Cytochrome P450 2E1	A cytochrome P450 monooxygenase involved in the metabolism of fatty acids. Mechanistically, uses molecular oxygen inserting one oxygen atom into a substrate, and reducing the second into a water molecule, with two electrons provided by NADPH via cytochrome P450 reductase (NADPH--hemoprotein reductase). Catalyzes the hydroxylation of carbon-hydrogen bonds. Hydroxylates fatty acids specifically at the omega-1 position displaying the highest catalytic activity for saturated fatty acids. May be involved in the oxidative metabolism of xenobiotics (Probable).
DES	Desmin	Muscle-specific type III intermediate filament essential for proper muscular structure and function. Plays a crucial role in maintaining the structure of sarcomeres, inter-connecting the Z-disks and forming the myofibrils, linking them not only to the sarcolemmal cytoskeleton, but also to the nucleus and mitochondria, thus providing strength for the muscle fiber during activity. In adult striated muscle they form a fibrous network connecting myofibrils to each other and to the plasma membrane from the periphery of the Z- line structures.
HNF4A	Hepatocyte nuclear factor 4-alpha	Transcriptional regulator which controls the expression of hepatic genes during the transition of endodermal cells to hepatic progenitor cells, facilitating the recruitment of RNA pol II to the promoters of target genes. Activates the transcription of CYP2C38 (By similarity). Represses the CLOCK- ARNTL/BMAL1 transcriptional activity and is essential for circadian rhythm maintenance and period regulation in the liver and colon cells.
ITGA2B	Integrin alpha-IIb light chain	Integrin alpha-IIb/beta-3 is a receptor for fibronectin, fibrinogen, plasminogen, prothrombin, thrombospondin and vitronectin. It recognizes the sequence R-G-D in a wide array of ligands. It recognizes the sequence H-H-L-G-G-G-A-K-Q-A-G-D-V in fibrinogen gamma chain. Following activation integrin alpha-IIb/beta-3 brings about platelet/platelet interaction through binding of soluble fibrinogen. This step leads to rapid platelet aggregation which physically plugs ruptured endothelial cell surface.
KDR	Vascular endothelial growth factor receptor 2	Tyrosine-protein kinase that acts as a cell-surface receptor for VEGFA, VEGFC and VEGFD. Plays an essential role in the regulation of angiogenesis, vascular development, vascular permeability, and embryonic hematopoiesis. Promotes proliferation, survival, migration and differentiation of endothelial cells. Promotes reorganization of the actin cytoskeleton. Isoforms lacking a transmembrane domain, such as isoform 2 and isoform 3, may function as decoy receptors for VEGFA, VEGFC and/or VEGFD.

KRT19	Keratin, type I cytoskeletal 19	Involved in the organization of myofibers. Together with KRT8, helps to link the contractile apparatus to dystrophin at the costameres of striated muscle; Belongs to the intermediate filament family.
LEF1	Lymphoid enhancer-binding factor 1	Participates in the Wnt signaling pathway. Activates transcription of target genes in the presence of CTNNB1 and EP300. May play a role in hair cell differentiation and follicle morphogenesis. TLE1, TLE2, TLE3 and TLE4 repress transactivation mediated by LEF1 and CTNNB1. Regulates T-cell receptor alpha enhancer function. Binds DNA in a sequence-specific manner. PIAG antagonizes both Wnt-dependent and Wnt-independent activation by LEF1 (By similarity).
PECAM1	Platelet endothelial cell adhesion molecule	Cell adhesion molecule which is required for leukocyte transendothelial migration (TEM) under most inflammatory conditions. Tyr-690 plays a critical role in TEM and is required for efficient trafficking of PECAM1 to and from the lateral border recycling compartment (LBRC) and is also essential for the LBRC membrane to be targeted around migrating leukocytes. Trans-homophilic interaction may play a role in endothelial cell-cell adhesion via cell junctions.
SELP	P-selectin	Ca(2+)-dependent receptor for myeloid cells that binds to carbohydrates on neutrophils and monocytes. Mediates the interaction of activated endothelial cells or platelets with leukocytes. The ligand recognized is sialyl-Lewis X. Mediates rapid rolling of leukocyte rolling over vascular surfaces during the initial steps in inflammation through interaction with SELPLG; Belongs to the selectin/LECAM family.
VWF	Von Willebrand antigen 2	Important in the maintenance of hemostasis, it promotes adhesion of platelets to the sites of vascular injury by forming a molecular bridge between sub-endothelial collagen matrix and platelet- surface receptor complex GPIb-IX-V. Also acts as a chaperone for coagulation factor VIII, delivering it to the site of injury, stabilizing its heterodimeric structure and protecting it from premature clearance from plasma.

Table S4: Protein-protein interaction network statistics and combined score annotation obtained using STRING database

<p>Number of nodes: 13 Number of edges: 28 Average node degree: 4.31 Avg. local clustering coefficient: 0.841 Expected number of edges: 12</p>
--

PPI enrichment p-value: 5.66e-05

Protein 1	Protein 2	Combined score
AHSG	ALB	0.999
ALB	VWF	0.871
ALB	ITGA2B	0.701
ALB	SELP	0.72
ALB	KDR	0.618
ALB	AHSG	0.999
ALB	DES	0.473
ALB	CYP1A2	0.622
ALB	CYP2E1	0.637
ALB	HNF4A	0.673
ALB	KRT19	0.687
ALB	PECAM1	0.781
CYP1A2	ALB	0.622
CYP1A2	HNF4A	0.667
CYP1A2	CYP2E1	0.982
CYP2E1	ALB	0.637
CYP2E1	HNF4A	0.476
CYP2E1	CYP1A2	0.982
DES	ALB	0.473
DES	PECAM1	0.403
HNF4A	LEF1	0.999
HNF4A	ALB	0.673
HNF4A	CYP2E1	0.476
HNF4A	KRT19	0.609
HNF4A	CYP1A2	0.667
ITGA2B	VWF	0.999
ITGA2B	KDR	0.53

ITGA2B	ALB	0.701
ITGA2B	PECAM1	0.882
ITGA2B	SELP	0.965
KDR	VWF	0.848
KDR	ITGA2B	0.53
KDR	SELP	0.453
KDR	ALB	0.618
KDR	PECAM1	0.999
KRT19	ALB	0.687
KRT19	HNF4A	0.609
KRT19	PECAM1	0.781
LEF1	HNF4A	0.999
PECAM1	VWF	0.918
PECAM1	ITGA2B	0.882
PECAM1	SELP	0.908
PECAM1	KDR	0.999
PECAM1	ALB	0.781
PECAM1	KRT19	0.781
PECAM1	DES	0.403
SELP	VWF	0.999
SELP	ITGA2B	0.965
SELP	KDR	0.453
SELP	ALB	0.72
SELP	PECAM1	0.908
VWF	KDR	0.848
VWF	ALB	0.871
VWF	PECAM1	0.918
VWF	SELP	0.999
VWF	ITGA2B	0.999

I (***Souradeep Dey***) certify that the aforementioned research article is an authentic record of the results obtained from the research work carried out by me under the supervision of Prof. Biman B. Mandal (thesis supervisor) in the Centre for Nanotechnology, Indian Institute of Technology Guwahati, India.

A handwritten signature in blue ink, reading "Souradeep Dey". The signature is written in a cursive style with a long horizontal stroke at the end.

(Souradeep Dey)